A Study of the XUV Flux Emission from Laser-Plasmas Using a Multilayer Monochromator

A thesis submitted for the degree of

Master of Science

by

M J Collins B Sc

School of Physical Sciences
Dublin City University
February 1994

Research supervised by

J T Costello Ph D and J P Mosnier Ph D

Declaration

This thesis is based on the work of the author

Dedication

I dedicate this work to Miriam and Luke

“ the extreme ultraviolet has changed from a little-known region to a well-recognised and important part of the spectrum ”

Professor Lyman, 1928

“Do I believe in God? I am plagued by doubts What if everything is an illusion and nothing exists? In that case, I definitely overpaid for my carpet If only God would give some clear sign! Like making a large deposit in my name at a Swiss Bank ”

Woody Allen, 1972

Contents

Chapter 1 Introduction

Chapter 2 **Experimental Systems**

Chapter 3 **Characterisation of Nd:YAG Plasmas**

Chapter 4 **Atomic-Number Dependence**

Chapter 5 **Double-Pulse Experiment**

Appendices:

Acknowledgements

I wish to express my sincerest thanks to my supervisors, Dr John Costello and Dr Jean-Paul Mosnier, for their guidance, support, attention to detail and enthuasism throughout the course of this work They were always available for discussion, at any level, for any reason, during my time here and for this reason, I will remain grateful

To the other members of the laser-plasma group, Prof Eugene Kennedy, Matthew Shaw, Laurence Kiernan, Hassan Sayyad and Ulrich Koeble, I offer many thanks for the laughs, helpful chats and good times shared In particular, I am indebted to Matty for his help with the software interfacing in the early days of this work

I wish to offer many thanks to Desmond Lavelle and Cian Merne for their skilful and efficient engineering of parts used in the XUV flux measurement system, especially Des for the table-tennis games on Thursdays, "your a bit of a Fine Gaeler"

I would like to take this opportunity to thank other people in the physics department who have made contributions to this work To the technical staff, in particular, Albert Devine for the photographs contained here and John Lynch for assistance with the vacuum system, I extend my thanks for any help offered I would also like to thank Tony Caffola for use of his multilayers program Thanks must also go to Barchewitz and co-workers at the Université Pierre et Marie Curie in Paris for the multilayer mirrors and reflectivity measurements It was very much appreciated

To my family and the Magee family, thanks for always being there for me

I would like to acknowledge the financial support of Eolas and the Clare County Council during the course of this work

Finally, to friends old and new, who in their own inimitable way have contributed in one form or another to this thesis, I offer my best wishes

Abstract

When the output of a high-power laser is focussed onto the surface of a solid target, a localised and short-lived plasma is formed which is characterised by high electron densities and temperatures As a result, such plasmas radiate predominantly in the extreme UV and x-ray spectral regions Results from a study on the dependence of extreme ultraviolet (XUV) emission from plasmas created with a conventional Nd YAG laser (500 mJ, 10 ns) on target elements from carbon through lead are presented A complete description of the XUV flux measurement system is given For a number of elements, spectral measurements in the energy region of interest were recorded using a 2 2 m grazing incidence multichannel photoelectric spectrometer These spectra are used to generate a complementary atomic-number dependence which is compared with that yielded from the flux measurement system

The XUV emission spectra from plasmas of cobalt through zinc are measured The corresponding predominant ion stages and electron temperatures are inferred from these spectra Emission spectra were previously recorded on a 2 m photographic grazing incidence spectrograph As a result of this study, new lines from the $3s^23p^n$ -> $3s^23p^{n-1}4s$ transitions arrays, for n = 1, 3 and 4, have been classified

Finally, following recent reports on sub-nanosecond double-pulsed laser-produced plasmas yielding enhanced x-ray emission, we have performed a corresponding study with our table-top laser source Results from measurements of the XUV dependence on time-delay, energy ratio and overlap between the laser pulses are reported We have observed up to a 40% increase in the XUV flux, under certain conditions, over single pulse produced plasmas of the same total laser pulse energy

Chapter 1

Introduction

In this chapter, the basic physics of plasmas is introduced and a number of different plasma-production techniques briefly outlined The generation and evolution of a laser-produced plasma is discussed and associated plasma models are mentioned Some important applications of laser-plasma light sources are underlined and the relative merits of different XUV sources compared An introduction to the work undertaken in this thesis draws the chapter to a conclusion Formulae are given in the international system (S I) of units unless otherwise stated

1.1 Overview

This section briefly reviews the general physics of plasmas The features of a selected number of methods for plasma production are highlighted, with the focus on laser-produced plasmas The UV-wavelength subdivisions are defined and associated nomenclature is given

1.1.1 General Plasma Properties

A significant confirmation of Einstein's theory of the interaction of radiation with matter was the advent of the laser [1] In turn, the interaction of laser radiation with matter has heralded a whole new field of basic and applied physics research At high laser irradiances, all materials are vapourised and ionised, forming what is known as a plasma The term "plasma" was first used to describe the collective behaviour of charged particles by Tonk & Langmuir [2] in their study of oscillations in electric discharges The plasma state, often referred to as the "fourth state of matter[1]", is believed to account for about 99 9% of apparent matter in the universe whether stellar or interstellar material

For a collection of charged particles to be defined as a plasma, certain criteria must be satisfied [4]

1) The presence of collective effects constitutes a primary plasma condition A quantative measure of this criterion is the Debye length, λ_D , the distance over which the electric field of an individual charge extends before it is effectively shielded by oppositely charged particles in its environ It may be defined as

$$\lambda_D = (\varepsilon_0 k_B T_e/n_e e^2)^{1/2} \approx 7(T_e(\mathrm{eV})/n_e(\mathrm{cm}^{-3}))^{1/2} \ \ (\mathrm{cm}) \qquad (1)$$

---

[1] First coined by W Cookes [3] The plasma state follows in the series of solid, liquid and gaseous states of matter

where n_e is the number of electrons per unit volume of charge e, k_B is the Boltzmann constant, T_e is the absolute electron temperature (Note 1 eV = 11,600 K) Beyond λ_D, collective effects dominate Thus the first criterion may be stated as

$$\lambda_D << L \qquad (2)$$

where L is the linear extent of the plasma

2) The assumption of a large number of particles in the neighbourhood of a particular charged particle to provide the decrease in the field for the deduction of the Debye length is a further criterion To ensure applicability of this criterion, the number of particles, N_D, within a Debye sphere of radius λ_D, must be greater than 1, i e ,

$$N_D = (4\pi n_e \lambda_D^3)/3 = 1380\ T_e(eV)^{3/2}/n_e(cm^{-3})^{1/2} >> 1 \qquad (3)$$

3) Quasi-neutrality is another important condition which may be defined by

$$n_i \approx n_e \qquad (4)$$

where n_i is the plasma ion density That is to say, the system retains overall space charge neutrality

4) A characteristic parameter of a plasma is the fundamental frequency, ω_{pe}, at which the electrons oscillate Generally called the plasma frequency, it may be defined as

$$\omega_{pe} = (e^2 n_e/\varepsilon_0 m_e)^{1/2} = 5\ 65\times10^4\, n_e(cm^{-3})^{1/2} \qquad (5)$$

where m_e is the electronic mass and ε_0 is the permittivity of free space Collisions between ions and electrons will tend to dampen these collective oscillations Thus, in order for oscillations to be only slightly damped, the collisional frequency, ω_c, must be so small that

$$\omega_{pe} >> \omega_c \qquad (6)$$

1.1.2 Methods of Plasma Production

Plasmas may be produced by many different techniques Some common plasma production methods are now briefly mentioned [5]

a) *Low-pressure cold-cathode discharge tubes* can be used to initiate and maintain a low-pressure steady-state (or pulsed) arc discharge by application of a voltage across the anode-cathode The plasma produced between the electrodes has a low density (~10^{10} cm^{-3}) and low temperature (typically 500 K) Cold-cathode discharge plasmas found their main use at the early stages of plasma studies and in atomic spectroscopy

b) *Plasma guns* are capable of producing a plasma in one location (the "gun barrel") and injecting it into a region where an experiment is occurring, for example, an experimental test chamber These sources supply 2 – 10 μs bursts of typically 10^{17} plasma particles with an average ion energy of 1 keV They find application in experiments where it is desired to investigate the plasma decay following the injection into a region of containment There are many forms of plasma guns but the most popular are the "occluded gas source" [6] and the "Marshall Gun" [7]

c) *Thermionic Arc Discharge Tubes* are an improvement on the cold-cathode discharge tubes for laboratory studies Arc discharge tubes use a thermionic oxide coated cathode as an electron source Plasma densities of 10^9 – 10^{13} cm^{-3} (variable over this range) are typical This source finds application in the study of plasma waves and oscillations [8]

d) *RF-produced plasmas* use alternating electric fields to induce and maintain gas breakdown (by accelerating electrons to energies greater than the gas ionisation potential) Plasma densities of approximately 10^{10} cm^{-3} are typical Substantially higher energies (~20 keV) are obtainable by modifying the set-up to be performed in a magnetic field These are called cyclotron resonance plasmas when the exciting RF-field has the same frequency as the cyclotron frequency of electrons

e) *Laser-produced plasmas (LPP)*

The study of laser-produced plasmas is one of the fastest growing fields of present day physics and has generated many innovative applications, e g , in materials science and clinical procedures but arguably the most important is the search for the safe production of clean nuclear fusion energy with low-cost inexhaustible fuel

When a high peak-power laser pulse is focused to a power density in excess of 10^8 W cm^{-2} onto the surface of a solid target (usually in *vacuo*), a short-lived ($t \approx 10^{-13} - 10^{-6}$ s), high-temperature ($T_e \approx 10^6 - 10^8$ K), dense ($n_e \approx 10^{19} - 10^{24}$ cm^{-3}) plasma is produced In one of the first experiments, W I Linlor [9] irradiated a metal target under vacuum and demonstrated that the irradiated region formed a small, dense plasma and that 1 keV metal ions were emitted from this region Since many of the LPP parameters (such as electron temperature and peak/dominant ion stage) are, to a certain degree, controllable, the study of LPP's has greatly enhanced our understanding of hot, ionised matter This is directly important in many areas of research such as astrophysics (e g determining the relative abundance of elements in galaxies) and laser physics (e g using laser-produced plasmas as gain media in x-ray/XUV laser systems)

The LPP emits an intense burst of radiation (which exists for about the same duration as the driving laser pulse) spanning a broad spectral region (x-ray to visible) but emitting predominantly in the vacuum ultraviolet (VUV) spectral region (2 – 2000

Å) Spectra generally exhibit line emission (due to bound-bound transitions within the atoms and ions) and continuum emission due to Bremsstrahlung (free-free transitions) and/or recombination (free-bound transitions) processes, the relative contribution of which depends, to a considerable extent, on the atomic-number of the target material

1.1.3 Wavelength Regimes and Nomenclature

The various names given to the wavelength regions of the electromagnetic (EM) spectrum below 2000 Å are based on the nature of the optical instruments used there Because of the opacity of air between 2000 and 2 Å and consequently the need to use evacuated spectrographs, this regime has been named the vacuum ultraviolet [10] The VUV can be further subdivided into the soft x-ray (SXR) and extreme ultraviolet (EUV) regions Since the EUV region includes the SXR region it was proposed by Tousey [11] that it be contracted to XUV Figure 1 1 defines these various somewhat-overlapping short wavelength regions

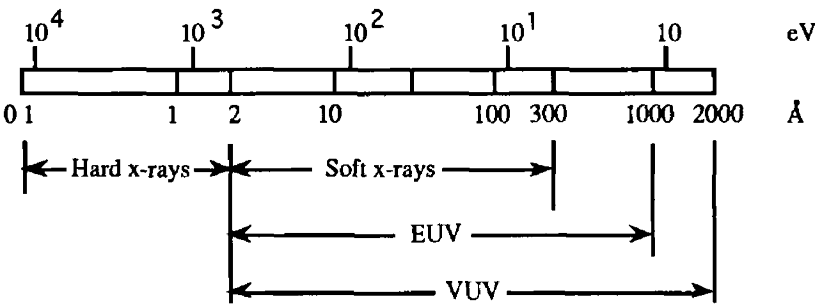

Figure 1 1 Definition of wavelength regions and nomenclature used below 2000 Å [12]

One can easily transform from wavelength, λ, to energy, E, and vice versa using the simple relation

$$\lambda(\text{Å}) \approx 12{,}398\ 5/E(\text{eV}) \tag{7}$$

1.2 Evolution of a Laser-Produced Plasma

The evolution of a laser-plasma can be divided into two distinct stages initiation and growth Each stage is briefly described in the following sections

1.2.1 Initiation

The primary stage of laser-plasma production differs depending on whether the target material is a metal or an insulator due to the difference in the bandgap for each Since only metal targets have been examined by the author, the present discussion will omit the case of insulators

When the electric field of a focussed laser pulse impinges on a metal surface, the EM radiation penetrates to a depth of a fraction of the laser wavelength (known as the skin depth) The skin depth, ∂, is related to the metal conductivity by the well-known equation (in m k s units)

$$\partial = (\pi f \mu_0 \sigma)^{-1/2} \qquad (8)$$

where μ_0 is the permeability of free space, f is the frequency of the laser radiation and σ is the conductivity in mhos m^{-1} [13] For a non-magnetic metal such as aluminium with $\sigma = 3\ 65 \times 10^7$ mhos m^{-1}, irradiated with Nd YAG laser light of frequency $2\ 82 \times 10^{14}$ Hz, the depth of penetration of the laser radiation is $\partial \approx 5$ nm The laser irradiance ϕ (in W cm^{-2}) is related to the r m s electric field strength, E_{rms}, by the expression [14]

$$E_{rms} = 19\ 4\phi^{1/2} \quad (\mathrm{V\ cm^{-1}}) \qquad (9)$$

so that for $\phi = 10^{12}$ W cm^{-2}, $E_{rms} \approx 2 \times 10^7$ V cm^{-1}, this value being 0 4% of the Coulomb field of a hydrogen nucleus at the first Bohr radius (5×10^9 V cm^{-1}) As a result of this strong interaction with electrons in the conduction band, heating, evapouration and ionisation occur extremely rapidly The net effect of this strong coupling is to generate a thin plasma layer close to the metal surface This priming plasma is generated in the first few cycles of the driving laser pulse

1.2.2 Growth of Plasma

Incoming radiation is absorbed in the priming plasma mainly by inverse Bremsstrahlung (IB) The Johnston-Dawson [15] absorption coefficient for this process is given by

$$K(\omega) = 5\ 64\times10^{-11}\ Zn_e^2 \ln\Lambda\, \omega^2 T_e^{3/2} \times 1/[1 - (\omega_p^2/\omega^2)]^{1/2} \qquad (10)$$

where the familiar symbols have their usual meaning, Z is the atomic number of the target material and ω is the frequency of the laser radiation The quantity $\Lambda = \upsilon_T/\omega_{pe}r_m$, where υ_T is the thermal velocity of the electrons and r_m is the minimum impact parameter, arises from the fact that IB is essentially a process which takes place during electron-ion collisions $Ln\Lambda$ is usually between 5 and 10 for laser-produced plasmas [16] At the early stages of absorption we find that

$$\omega >> \omega_p \qquad (11)$$

and so the rate of absorption is mainly dependent on n_e^2 (and ω^2 and Z) As the energy absorbed increases, so too does the the temperature of the electrons T_e (and ions T_i) This, in turn, produces further ionisation which consequently increases the electron density n_e Hence, the absorption rate and, along with it, the ionisation rate escalate so that n_e increases still further until it eventually reaches a critical density n_{ec}

at some distance away from the surface of the metal The critical density of a laser-plasma may be determined using the equation

$$n_{ec} = m_e \varepsilon_0 \omega^2 / e^2 \approx 10^{21} / \lambda(\mu m)^2 \quad (cm^{-3}) \qquad (12)$$

where $\omega = 2\pi f$ is the angular frequency of the laser light. For a plasma created by an Nd YAG laser (λ = 1 064 μm), the EM radiation will propagate into the plasma until a critical density of ~9 4 × 10^{20} cm^{-3} is reached Across this critical density surface (where $n_e = n_{ec}$) one finds

$$\omega = \omega_p \text{ and } K(\omega) \rightarrow \infty \qquad (13)$$

and the layer becomes opaque to incident EM radiation which is therefore reflected outwards again For plasma layers immediately in front of the critical density layer

$$\omega < \omega_p \qquad (14)$$

and, according to equation (10), these layers become highly absorbing Therefore, most of the incoming radiation will now be deposited in the region in front of the critical density surface

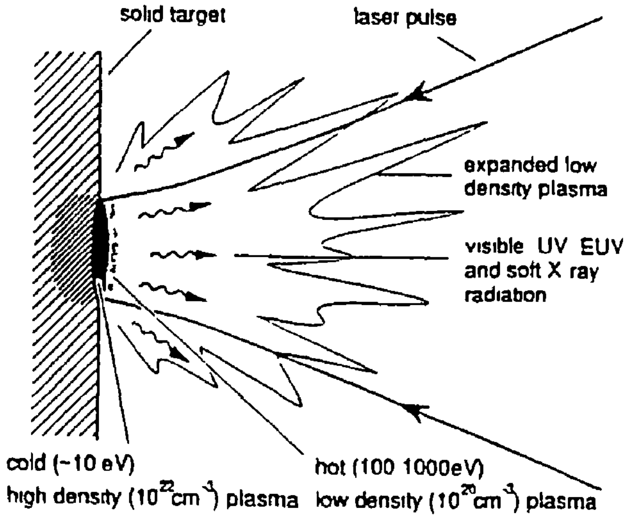

Figure 1 2 Representation of laser-plasma generation showing the solid target irradiated with high power laser light to produce a high density hot core and an expanding lower density plasma plume [17]

Although laser radiation no longer reaches the metal surface, plasma growth still continues due to heating of the ‘coronal’ region ($n_e < n_{ec}$) via IB Conduction of some of this heat to the metal is achieved through collisions of particles in the hot core ($n_e > n_{ec}$) with particles in the corona [18], thus producing yet further ionisation The plasma is driven mostly outwards from the solid target causing the electron density to decrease and laser radiation can again penetrate through the plasma to the metal surface This 'self-regulating' process continues smoothly throughout the duration of the laser pulse

1.3 Plasma Models

The simplest model for a plasma is that of a classical blackbody radiator, a material that absorbs radiation perfectly at all wavelengths This will be the first plasma model discussed in this section

For an ideal plasma in complete thermodynamic equilibrium, particle velocities and populations obey Maxwell's and Boltzmann's distribution laws respectively The Saha distribution equation allows a quantitive description of relative abundances of ionic species while Planck's radiation law describes the intensity distribution of radiation from a plasma as a function of frequency However, many plasmas (such as laser-produced plasmas) are non-ideal and therefore require approximate equilibrium models to be developed in order to obtain a knowledge of the rates of all the atomic processes (e g collisional and radiative excitation, deexcitation, ionisation and recombination) Three non-ideal plasma models shall be considered briefly

1.3.1 Blackbody Radiator

One may compare the spectral emission from an optically thick plasma using an idealised heated solid called a blackbody radiator The fundamental emission spectrum is a continous one In the context of a plasma, line emissions are reabsorbed by the dense ionised matter An expression for the total XUV power density from a blackbody radiator can be obtained [19]

$$I = \sigma T^4 = 1\ 03 \times 10^5\ T_e(\mathrm{eV})^4 \quad (\mathrm{W\ cm^{-2}}) \qquad (15)$$

where σ is the Stefan-Boltzmann constant (= 5 67 × 10^{-8} W m^{-2} K^{-4})

The equation which describes a blackbody's spectrum was derived by Planck, that is

$$I(\lambda) = (2\pi hc^2/\lambda^5) \times [\exp(hc/\lambda k_B T)] \qquad (16)$$

where $I(\lambda)$ is called the spectral radiance at wavelength λ and h is Planck's constant, such that $I(\lambda)d\lambda$ is defined as the rate at which energy is radiated per unit area of surface for wavelengths lying in the interval λ to $\lambda + d\lambda$ Integrating this quantity over all wavelengths gives the spectral intensity of the blackbody emission at a particular temperature This is plotted in figure 1 3 as a function of temperature of the blackbody Using Wien's law, it is possible to assess the position, λ_p, of the peak of the spectral intensity by

$$\lambda_p(\text{Å}) = 2500\ T(\mathrm{eV})^{-1} \qquad (17)$$

This is also plotted in figure 1 3 as a function of temperature of the the blackbody

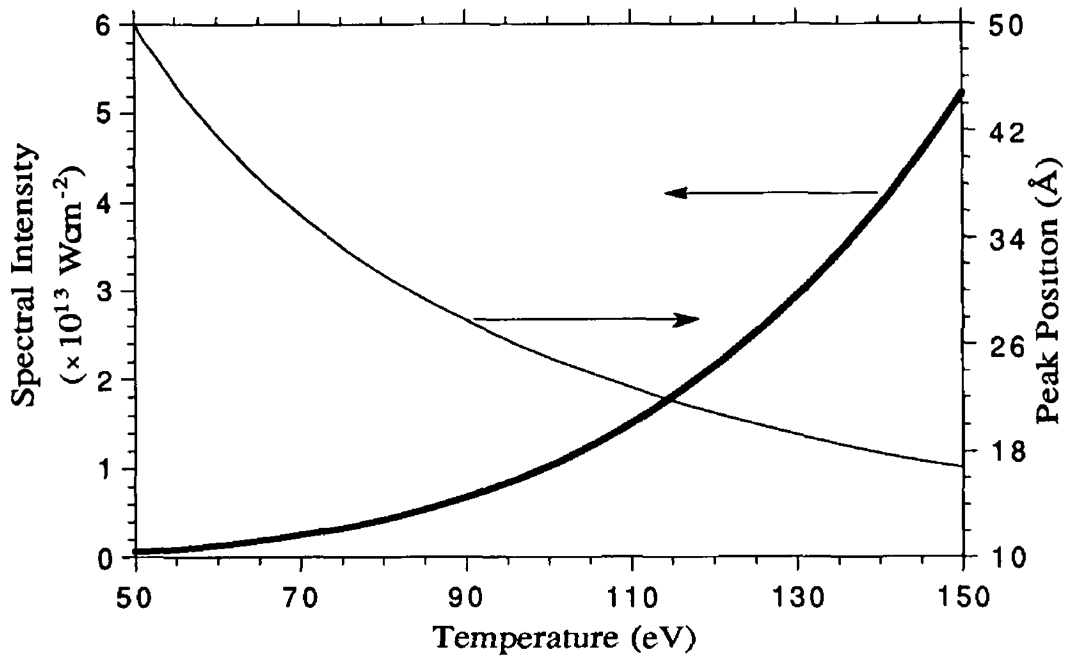

Figure 1 3 Dependence of XUV spectral intensity and average wavelength, λp, of the maximum intensity on the temperature of a blackbody radiator

The peak positions predicted by the blackbody model provides an estimate of the expected peak position for Bremsstrahlung and recombination emission from a plasma

Therefore, the blackbody radiator serves as a useful model for characterising the emission from an optically thick plasma In practice, of course, the emission from laser-plasmas will differ from blackbody spectra because plasmas are not completely optically thick, and they do show line radiation

1.3.2 Local Thermodynamic Equilibrium (LTE)

At high plasma densities ($n_e > 10^{22}$ cm^{-3}), collisional processes dominate over radiative processes in determining excited state populations The LTE model assumes that collisional events (in particular, those involving electrons) determine the behaviour of the system Electron-atom and electron-ion collision processes are extremely rapid and dominate (vis-à-vis radiative processes) the plasma rate equations In such circumstances each process is accompanied by its inverse and these pairs of processes occur at equal rates by the principle of detailed balance The laws which hold for thermodynamic equilibrium are assumed to be valid for LTE except, however, the radiation law which is not obeyed since radiative effects play an insignificant part in determining the equilibrium For the LTE model to hold, a necessary criterion [19] is (in c g s units)

$$n_e \geq 1.4 \times 10^{14} T_e(eV)^{1/2} \chi(p, q)^3 \quad (cm^{-3}) \qquad (18)$$

where $\chi(p, q)$ is the excitation potential (in eV) of the atomic transition from level p to level q The LTE model can be applied to Nd YAG-produced plasmas at very low degrees of ionisation ($z < 9$) [20]

1.3.3 Coronal Equilibrium (CE)

In low density plasmas ($n_e < 10^{19}$ cm^{-3}), as found in the solar corona, a second limiting type of equilibrium may be attained where a balance exists between excitation and ionisation by electron collisions and de-excitation and recombination by radiative processes In such plasmas, an excited atom will generally have time to radiate a photon before it undergoes a collisional transition Assuming the plasma is optically thin (that is, radiation escapes without interacting with the plasma), the inverse process of excitation by absorption of a photon is unlikely to occur Almost all atoms and ions are in their ground states, therefore it is assumed that collisional excitation from the ground state balances radiative decay A sufficient criterion [19] for applicability of the coronal model is

$$n_e < 5.6\times10^{8}(z+1)^{6} T_e^{1/2} \exp(1.162\times10^{3}(z+1)^{2}/T_e) \quad (cm^{-3}) \qquad (19)$$

where z is the ionic charge (the number of electrons removed from the atom) The coronal model can be applied to Nd YAG-produced plasmas for ions with charge states above $z = 29$ [20]

1.3.4 Collisional-Radiative (C-R) Equilibrium

In the intermediate density range neither the LTE or coronal model is valid To this end, the collisional-radiative model of Bates *et al* [21] was developed by modification of the coronal model to account for collisional de-excitation and three-body recombination According to the theory of the C-R model, excitation is considered to be dominated by collisional processes while de-excitation occurs primarily through radiative processes

An extension of this model applied to laser-produced plasmas was developed by Colombant and Tonon [20] who derive useful formulae to calculate (i) the relative ion population densities, (ii) the electron temperature as a function of laser flux and, (iii) the dominant ionisation stage as a function of electron temperature'

The steady state relative ion population density, n_z, may be calculated from

$$n_{z+1}/n_z = S(z, T_e) \,/\, [\alpha_r(z+1, T_e) + n_e \alpha_{3b}(z+1, T_e)] \qquad (20)$$

where S(z, Te) is the collisional ionisation coefficient, $\alpha_r(z, T_e)$ is the radiative-recombination coefficient, and $\alpha_{3b}(z, T_e)$ the three-body recombination coefficient. From this expression, the ratio

$$n_z / \sum_{k=1}^{z} n_k$$

may be computed and its evolution as a function of T_e determined

The electron temperature may also be estimated as a function of incident laser energy density and the atomic-number of the target element using

$$T_e(\mathrm{eV}) \approx 5\ 2\times10^{-6} Z^{1/5}[\lambda^2\phi\,(\mathrm{W\ cm^{-2}})]^{3/5} \qquad (21)$$

where λ is the wavelength of the laser radiation in microns

For LPP's with $T_e \geq 30$ eV, the dominant charge state may be calculated as a function of the electron temperature by the following relation

$$z \approx 2/3\ [ZT_e(\mathrm{eV})]^{1/3} \qquad (22)$$

It should be noted that this expression is better verified for heavy elements than lighter ones for which the formula is only approximate [20] This model is particularly appropriate in the power density range of $10^{11} - 10^{13}$ W cm^{-2} and for medium to high atomic-number elements

1.4 Applications of LPP Light Sources

In recent years, laser-produced plasmas have enjoyed an increased level of research activity in the arena of applications These applications take advantage of the LPP's unique emission characteristics in the XUV such as the pulse-duration (typically comparable to that of the laser pulse width), the well-defined small physical dimensions, the choice of discrete or continuous nature of emission, the single-shot brightness and the shot-to-shot reproducibility A selection of important applications will now be discussed

1.4.1 High-Resolution Lithography

Minimum dimensions for standard UV-photolithography (typically microns) are diffraction limited and therefore, to obtain even higher densities of electronic components on a single chip requires the use of shorter wavelength sources (x-rays to XUV) for the mask exposure X-ray lithography offers the possibility of replication of submicron-scale features without the diffraction and multiple reflection effects associated with UV radiation or the scattering effects associated with electron beam exposures Electron-impact and synchrotron sources were once the only serious contenders for x-ray lithography, but feasibility studies (e g Nagel *et al* [22] and Gohil *et al* [23]) have demonstrated that LPP light sources can produce lithographs with superior uniformity over the entire chip area with no obvious quality differences (e g wall and surface uniformity) compared to those obtained with synchrotron sources Gohil *et al* [23] proposed that the soft x-ray output from a laser-plasma light-source (LPLS) may be increased by (i) increasing the laser repetition rate, (ii) using focussing with soft x-ray reflective optics (e.g. multilayers in the Schwarzchild configuration [24]), (iii) increasing the energy per pulse and/or (iv) reducing the quantity of "blow-off" products from the target which may travel to the experiment. Gohil argues that if these features are improved, the LPP lithographic light source will be at least as intense and of significantly better intensity uniformity per steradian than that obtainable using synchrotron radiation.

Recently, features as small as 0.1 µm have been recorded with high contrast using a Mo/Si multilayer-coated Schwarzchild objective and 14 nm radiation from a LPP source [25]. Also, at the Rutherford Appleton Laboratory, a 100 Hz KrF laser-plasma x-ray source was developed and tested in replication of sub-0.5 µm structures. Using proximity x-ray lithography images in 1.2 mm thick photoresist they have accurately reproduced features as small as 0.3 µm [26]. It should be noted that a laser-plasma x-ray lithography system based on an Nd glass laser system is nowadays commercially available [27].

1.4.2 High-Resolution Microscopy

A pulsed soft x-ray source (in the 10 – 100 Å region) for use in contact microscopy would provide high resolution, high contrast images with minimal radiation damage to the biological specimen involved compared to conventional microscopes. The presence of numerous absorption edges in the constituent N, C and O atoms at soft x-ray wavelengths provide high contrast imaging of edges and an opportunity to highlight some features while suppressing others [28].

Work on soft x-ray contact microscopy with a laser-generated carbon plasma source has been reported as early as 1985 by Rosser *et al* [29]. In this process, a sample in contact with an XUV-sensitive resist is exposed to 40 Å radiation from an LPP source. The sample, when removed, is developed and a relief pattern (corresponding to the sample x-ray opacity) is formed in which features as small as 20 nm are clearly discernible. To date, the highest resolution obtained in contact x-ray microscopy is 10 nm achieved by Feder *et al* [30].

Much of current effort is directed at developing scanning soft x-ray microscopes which expose the specimen to the minimum dose of damaging radiation and the information is immediately available on a computer. At present, there exists three scanning soft x-ray microscopes operating in the so called "water-window" (23 – 44 Å), all of which use synchrotron radiation and high-resolution Fresnel zone-plates as focussing optics [31]. Recently, Trail and Byer [32] have constructed a table-top soft x-ray microscope, with 0.5 µm resolution, that utilises a LPP source and normal-incidence multilayer-coated mirrors in the Schwarzchild configuration as focussing optics. Most recently, Daido *et al* [33] demonstrated a coherent monochromatic laser-plasma point x-ray source in the water-window operating at a repetition rate of up to 100 Hz for use in transmission scanning soft x-ray microscopy.

1.4.3 EXAFS Spectroscopy

Extended-x-ray-absorption-fine-structure (EXAFS) spectroscopy is a powerful analytical tool, providing information on identities and spatial arrangements of atoms in any solid, liquid or gas In this technique, the x-ray absorption coefficient of a material is measured as a function of energy from the K-edge or the L-edge of a specified element in the material to as far as 1 keV above the particular edge Absorption by an atom results in photoelectrons being ejected which may then scatter from nearby atoms Photoelectrons which have been backscattered from atoms in the immediate vicinity of the absorbing atom give rise to a periodic "wiggle" structure in the x-ray absorption spectrum Analysis of the wiggle structure above the absorption edge of the element in question can provide information relating to the spatial arrangement of atoms in the space surrounding the absorbing atom

In the past, chemical research with the EXAFS technique was limited due to lack of availability of intense x-ray sources Synchrotron radiation sources remedied this to some extent, but certain types of EXAFS experiments such as those designed to analyse highly transient structures (e g excited electronic states within molecules) require a complete EXAFS spectrum in a single, intense burst of x-rays synchronised with excitation of the sample Feasibility studies by Mallozzi *et al* [34] and Eason *et al* [35] have shown that laser-plasmas are almost ideal sources for fast kinetic studies of this type

1.4.4 XUV/VUV Spectroscopic Light Source

To be useful as a laboratory spectroscopic light source, it is desirable that the LPP source have a high intensity, good shot-to-shot reproducibility and emit a line-free continuum over a broad spectral range High atomic-number rare-earth elements, which radiate from ionised systems with partially-filled shells (Carroll, Kennedy and O'Sullivan [36,37]) are excellent candidates because any line emission from these materials is quite likely to be extremely dense and easily confused with continuum radiation Work by these authors has shown that with appropriate target selection, the LPP can provide clean, essentially line-free continua suitable for absorption spectroscopy from 40 – 2000 Å

Much work has been conducted on LPPs as backlighting sources, particularly in time-resolved or time-synchronised photoabsorption spectroscopy (this initially being exploited by Carroll and Kennedy [38] in their study of Li^+ in the XUV) The experimental arrangement of such studies generally consists of two laser-plasmas generated independently by separate lasers which have been time-delayed with respect to each other (ps –> ms) Continuum radiation from the backlighting plasma passes through the absorbing plasma column, thereby giving valuable information on the atomic structure of constituents within the absorbing plasma The technique, often referred to as the dual-laser plasma (DLP) method, is ideally suited to the study of ionic and refractory atom absorption (for which vapours cannot readily be formed [39]) A review of XUV absorption spectroscopy with laser-produced plasmas is given by Costello *et al* [40]

Line emissions from laser-plasmas are also effectively utilised for studying atomic and ionic structure and for diagnostics of LPPs Identification and classification of spectral lines emitted from highly ionised atoms develops an understanding of the energy level structure of such species which exist in astrophysical plasmas In one of the first experiments, Fawcett *et al* [41] classified spectral lines in Fe XV, Fe XVI, Ni XVII, Ni XVIII (where the Roman numeral represents the spectrum number or ionisation stage, e g $C^{3+} \equiv$ C IV) Since then, many thousands of reports on laser-plasma emission spectra have been published and the area continues to be an active one (see reviews by Fawcett [42], Martinson [43] and O'Sullivan [44])

Numerous methods exist for diagnosing electron densities and temperatures in LPPs One possible method of determining the electron density is to measure the Stark broadening of spectral lines (due to perturbations of the radiating particles arising from the microscopic electric fields of surrounding ions and electrons) The electron temperature may be determined spectroscopically from the ratio of the line intensities to the underlying Bremsstrahlung continuum [45] or by determining the intensity ratio of two spectral lines which have the same lower transition level [46] A review of laser plasma diagnostic techniques is treated by DeMichelis and Mattioli [47]

1.4.5 XUV/X-ray Lasers

The development of sophisticated modelling and multi-terawatt laser systems has allowed the theoretical and practical problems of demonstrating XUV/X-ray laser action in laser-plasmas to be overcome, generating a sudden upsurge of progress in this exciting new field Many physical processes within the LPP medium have been considered which can preferentially pump the population of an upper-bound energy level within an ion and give rise to a population inversion [48] These include (i) recombination of free electrons through three-body, radiative and dielectronic recombination, (ii) collisional excitation of both valence and inner-shell electrons through collisions with electrons and (iii) photoexcitation of bound electrons through resonant photoabsorption

Experiments involve the use of line foci to create elongated cylindrical plasmas of small diameters from fibres, exploding thin foils and solid single or double slab targets XUV multilayer mirrors are often employed to provide a double pass (half cavity operation) of the lasing radiation through the gain medium for enhanced gain efficiency [49]

Recombination lasers use free electrons, generated in the laser-heating phase, which combine with closed-shell ions to reestablish equilibrium Recombination is preferentially into bound levels close to the continuum limit and subsequent collisional and radiative cascading populates the lower-bound levels and ground state Population inversion due to non-thermal distributions of population densities among excited states can thus be achieved if the plasma cooling rate is fast enough Hydrogen- and lithium-like recombination lasers are based on this scheme One of the first observations of population inversion in an expanding plasma was due to Irons and Peacock [50] with the hydrogen-like C^{5+} 182 Å line Subsequent studies of this recombination line were reported by many authors including Suckewer *et al* [51] who successfully attained XUV laser action in a recombining magnetically-confined plasma column with an enhancement of $\sim$100 of stimulated emission over spontaneous emission Recombination into lithium-like ions has been studied for over a decade by groups such as Jaegle *et al* [52] with emphasis on the Al^{10+} ion lasing at 105 7 Å

Collisional-excitation lasers are generally based on electron impact collisions between free electrons and ground state bound electrons in a suitable plasma ion As a result, excitation to a higher bound level will create a population inversion with respect to a lower bound level Neon- and nickel-like collisional lasers are based on this scheme Zherkin *et al* [53] first described a scheme for obtaining a population inversion in neon-like ions Subsequently, Matthews *et al* [54] conducted the first successful experiment on a neon-like Se^{24+} ion laser at 206 3 and 209 6 Å High gain at short wavelengths has been produced in neon-like ions ranging from Ti^{12+} to Ag^{37+} at wavelengths from 326 to 80 Å, and in nickel-like ions from Sm^{24+} to Au^{51+} at wavelengths from 73 to 35 6 Å [55] For example, recent work at the Central Laser Facility (CLF) of the SERC Rutherford-Appleton Laboratory has focussed on the neon-like Ge XXIII laser line at 236 Å where amplification saturation and near-diffraction limit operation has been reported by Carillon *et al* [56] using a double plasma configuration with an XUV multilayer mirror to double-pass the double plasma

Resonantly photopumped laser schemes [57] are analogous to optical flash-pumped visible and IR-lasers except pumping is by soft x-rays, i e , radiation from one LPP is used to resonantly pump another Besides the overlap of transmission and absorption transition energies, strong transitions must be chosen for both the pump and the lasant ions As of yet, direct evidence of gain using this method has not been verified in the XUV Most of the work has concentrated on accurate measurements of population inversions [58], amplification of spontaneous emission (ASE) gains and potential lines for pump-matching [57]

1.4.6 XUV/X-ray Radiography

As laser fusion target performance changes towards ablatively-driven, low-temperature and high density fuel conditions, soft x-ray backlighting from LPPs has become an important method to determine the dynamics of a laser-driven implosion [59] The bright emission lines from laser-plasmas map historically the implosion in one or more regions of the microballoon target In these experiments, multiple lasers drive the implosion and a separate time-synchronised beam generates the backlighting radiation from a different target The soft x-ray burst can be delayed from typically 200 - 600 ps in order to capture different moments in the implosion [60]

Benattar and Godart [61] successfully used the soft x-ray emission from a time-synchronised laser-generated copper plasma to probe the density profile of another laser-plasma in its over-dense region ($n_e > n_{ec}$) using an x-ray refraction method

1.4.7 Reflectometry

Multilayer optics are now accepted as essential components in the development of novel soft x-ray instrumentation Evaluation of multilayer properties such as spectral reflectance is crucial if reliable implementation of these developments is to be achieved To this end, Trail *et al* [62] carried out initial tests to evaluate multilayer reflectances using a grazing incidence monochromator Nakayama *et al* [63] designed and constructed a soft x-ray reflectometer which utilises an Nd YAG- or XeCl-driven samarium plasma, a constant deviation monochromator and a reflectometer Comparison of its performance with results obtained from a synchrotron source verified its usefulness for reflectance measurements Recently, Azuma *et al* [64] proposed a new experimental arrangement that is capable of measuring the spectral reflectance of multilayer coatings in the soft x-ray region using a single laser-plasma pulse

1.5 Comparison with other XUV Light Sources

VUV and SXR radiation is available from laboratory sources such as laser-produced plasmas and B-R-V[2] vacuum sparks as well as large facility-based sources such as synchrotrons In choosing the best light source for a particular application, an experimenter is confronted with a myriad of advantages and disadvantages associated with each source The relative merits of each of the above mentioned sources are intercompared in table I 1 Although the single pulse power of the LPP exceeds that of the synchrotron by at least 4 orders of magnitude, the average power is lower by typically 3 orders of magnitude However, as excimer and solid state lasers move towards the 10^3 pulses s^{-1} regime at > 100 mJ pulse^{-1}, the average power gap will be narrowed

---

[2] Ballofet-Romand-Vodar [65]

Table I 1 Comparison of XUV light sources [40]

Source Property	LPP	Synchrotron	B-R-V
Peak Spectral Irradiance/Pulse (photons cm ^{2} mr ^{2} Å^{1})	~10^{10}	10^{5} - 10^{7}	~10^{7}
Average Spectral Irradiance (photons cm^{2} mr ^{2} Å^{-1} s ^{1})	~10^{12}@ 100 Hz	~10^{14}	~10^{8} @ 10 Hz
Polarisation	none	linear in orbit plane	none
Repetition Rate (Hz)	1 - 10^{2}	10^{7} - 10^{9}	10
Directionality	emits in 2π sr	emits in narrow cone tangential to electron orbit	emits in 2π sr
Reproducibility	< 5 %	< 1 %	20 - 40 %
Pulse Duration (ns)	< 20	~0 1	40 - 90

A radiometric comparison of a LPP and B-R-V source is dealt with by Kuhne [66], while Kuhne and Wende [67] review radiometric source and detector standards in the VUV and soft x-ray region Spectral irradiance power measurements of soft x-ray sources, including LPPs, using the electron storage ring BESSY as a standard radiometric source is detailed by Fisher *et al* [68]

1.6 Motivation for Present Work

High power and compact lasers have stimulated the growth of laboratory plasma light sources over the past decade Much work has been done [22,69] to successfully develop table-top (repetitively-) pulsed sources for operation in the XUV spectral region In discussing the characterisation of laser-plasmas for use as light sources, many fundamental questions arise that demand detailed consideration, e g ,

(i) How does the XUV flux emitted from a laser-plasma depend on the atomic-number of the target material?

(ii) How does the energy, wavelength, pulse duration and focussing conditions of the laser radiation affect the XUV flux output?

(iii) What is the SXR/XUV pulse duration (in emission) from an LPP?

(iv) How does the ambient environment conditions (i e vacuum, gas, and so on) influence the plasma XUV flux emission?

(v) What is the effect of different target geometries on the generation of XUV radiation?

(vi) How may the XUV flux output from an LPLS be enhanced?

Many of these key questions have been considered in detail by various authors For instance, the target atomic-number, laser irradiation and pulse duration dependence of laser-plasma emissions in the x-ray spectral region have been investigated by McMordie and Simmons [70] for 26 elements $(6 \leq A \leq 92)$ in the spectral region above 800 eV using a 50 ns CO_2 laser system, by Bleach and Nagel [71] on 17 elements $(6 \leq A \leq 68)$ between 0 8 – 5 keV using a 20 ns Ruby laser, by Gilbert *et al* [72] on 36 elements $(4 \leq A \leq 92)$ between 0 7 – 20 keV using an 8 ns Nd glass laser and by Gupta *et al* [73] on 7 elements $(6 \leq A \leq 73)$ above 0 9 keV using a 5 ns Nd glass laser However, relatively little work has been reported on the atomic-number dependence in the important XUV region [74, 75] The work of this author focusses on the LPP atomic-number dependence of 27 elements $(6 \leq A \leq 82)$ in the XUV energy region using a 10 ns Nd YAG laser system

The focussed power density attainable with the Nd YAG laser system in our laboratory is $\sim 5 \times 10^{11}$ W cm^{-2} (section 2 1 1) A power density of this order would create an average electron temperature of 90 – 130 eV Rather than study the atomic-number dependence over a broad spectral range as with previous works, it was decided that a narrow energy region would be selected To achieve this, an XUV multilayer mirror [76] was employed Multilayers reflect radiation in a manner analogous to Bragg crystals At a fixed angle to the incoming radiation, the multilayer behaves as a bandpass filter, reflecting radiation in a narrow band centred on the angle-dependent peak wavelength given by the modified Bragg equation (Appendix A) It is important for many applications involving laser-plasmas, such as high-resolution lithography and microscopy, to understand the atomic-number dependence of the emitted XUV flux and the characteristic nature of this radiation To this end, we have carried out a systematic study of this dependence in a narrow radiation band (~6 eV full width) centred at 125 4 eV in the XUV using a NiCr/C multilayer mirror (section 2 1 2), corresponding to the approximate spectral peak intensity of the Nd YAG-generated plasmas Results are presented in chapter 4

A knowledge of the radiative nature of the XUV emission from these plasmas is the key to understanding their atomic-number dependence Therefore, in order to facilitate interpretation, emission spectra of a selected number of target metals used in the atomic-number dependence study were recorded in the energy region of the multilayer bandpass using a 2 2 m MacPherson spectrometer equipped with an EUV optical multichannel analyzer (OMA) [77] These high-resolution spectra allowed characterisation of the XUV flux emissions in terms of transition arrays between electron configurations of 5 – 15 times ionised species In order to simulate the atomic-number dependence plot generated with the multilayer system, the instrument bandwidth of the multilayer system was used to modify the spectra recorded with the OMA to produce a complementary atomic-number dependence plot Both plots are compared in chapter 4

Emission spectra from plasmas of cobalt through zinc were previously recorded by Costello and Mosnier [78] with a 2 m photographic spectrometer These spectra have since been analysed by the author, as an introduction to this work, to gain an understanding of the typical dominant ion stages and electron temperatures of plasmas generated by the Nd YAG laser system in our laboratory In the process, previously unobserved lines have been recorded and measured for the $3p^n$ ->$3p^{(n-1)}4s$ (n = 1, 3, 4) transition arrays, and subsequently classified using *ab initio* Hartree-Fock calculations Results are presented in chapter 3

A most important factor for use of LPPs as efficient light sources is the soft x-ray conversion efficiency (defined as the ratio of the measured XUV fluence to the main laser energy per unit solid angle, expressed in % sr^{-1}) Studies have been undertaken to examine the effect of introducing a weak prepulse beam before the main pulse to create a pre-plasma which is subsequently heated after some time interval by the main laser pulse Kodama *et al* [79], using this technique, observed a factor of 2 – 3 times enhancement in the conversion efficiency using a 0 53 µm picosecond laser Tom *et al* [80] used an ultrashort (femtosecond) prepulse to create a pre-plasma which was subsequently irradiated by a time-delayed second pulse and noticed that a higher conversion efficiency was recorded compared to that achieved with a single pulse

A corresponding study has been undertaken in this work using a conventional nanosecond table-top laser source, the impetus being to generate more XUV photons from an LPP by using a prepulse and time-delayed main pulse than could be obtained using a single laser beam of the same total energy In chapter 5, measurements of the XUV flux dependence on time, space and the prepulse to main pulse energy ratio are presented

Concluding Remarks

This chapter has served to introduce the field of laser-plasma physics in a broad and general manner The basic physics of plasmas was introduced and a qualitative description of the formation and growth of a laser-plasma briefly outlined As in most fields of physics, technological applications stand as testimony to the degree of development and usefulness of research The range of applications which employ LPPs is far from fully exploited, as this area is still a relatively young one However, some of the important uses of the present for LPPs were outlined A discussion of the motivation and philosophy behind this research program brought the chapter to a conclusion

Chapter 2

Experimental Systems

This chapter describes the experimental arrangements used in the course of the work described in this thesis Particular detail is given to the important components of the system used to investigate the atomic-number and double-pulse pumping dependence on the EUV flux emitted from laser-produced plasmas This is followed by a calculation of the energy bandpass of the LSM system The software developed to control system hardware and handle data acquisition is discussed The salient features of the 2 m photographic and 2 2 m MacPherson spectrometers are outlined A comparison of the multilayer and 2 2 m systems draws the chapter to a conclusion

2.1 The Extreme UV Flux Measurement System

The generation and observation of XUV radiation from laser-produced plasmas requires (i) the use of a high power laser focussed onto a suitable target surface to create a hot plasma, (ii) a controllable environment, and (iii) appropriate detection The system shown in figure 2 1 was designed and assembled by the author to carry out a systematic study of the atomic-number dependence of laser-plasma XUV flux emission and also to investigate the effects of double laser pulse plasma generation on the XUV flux emission

In order to capture an XUV waveform on the oscilloscope, the sequence of events which took place are diagramaticlly illustrated in figure 2 2 A rising edge trigger pulse with a < 1 ns rise time and duration of 100 μs was sent from the PC/AT to the external flashlamp trigger circuit in the Nd YAG control console After 1 92 μs, the flashlamp synchronisation (sync) output circuit sent a rising edge trigger pulse of 120 μs duration to the Pockels cell trigger circuit Subsequently, after a 172 μs delay , a sync pulse is sent from the Pockels cell Q-switch sync circuit to the Pockels cell and the oscilloscope (to ensure that the device is in sampling mode when the XUV emission occurs), and 380 ns later the optical pulse is emitted from the laser Plasmas generated by the Nd YAG laser (in *vacuo*) emitted over a broad spectral range A narrow band of this radiation was selected by the collimating apertures and a multilayer mirror which operated at an angle of incidence of 45°, and reflected towards the detector unit which comprised a composite thin-film filter, a scintillator, an interference filter and a photosensitive gain device

Alignment of the laser-produced plasmas along the optical axis of the system was accomplished using two HeNe laser beams A HeNe laser beam was propagated through a series of collimating apertures to the multilayer mirror The position of the multilayer mirror was adjusted to an angle of incidence of 45° which redirected the

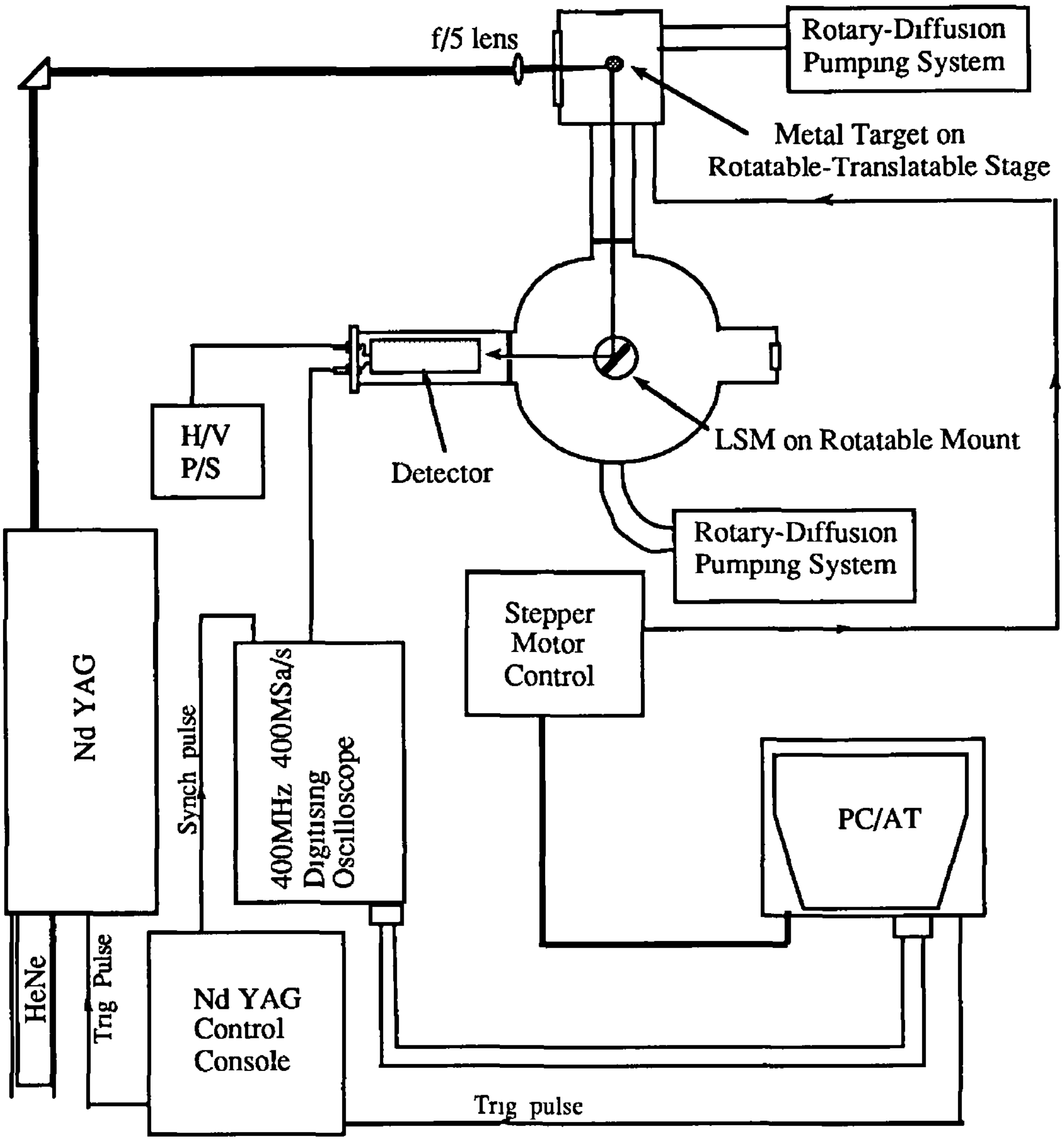

Figure 2 1 The extreme UV flux measurement system used to study the laser-produrced plasmas

beam through another series of apertures to fall centrally on the detector face This HeNe laser beam formed the optical axis of the system The HeNe alignment beam of the Nd YAG laser was then adjusted vertically to intersect the optical axis The intended target surface is then located at this point of intersection using an X-Y micrometer stage The target was scanned across the axis to ascertain the optimum position for the generation and detection of the XUV radiation

Appendix B contains photographs of the individual components of the system shown in figure 2 1, that is, the target mount, the multilayer mount, and the assembled XUV detector and its carriage A photograph of the completely assembled system is also included

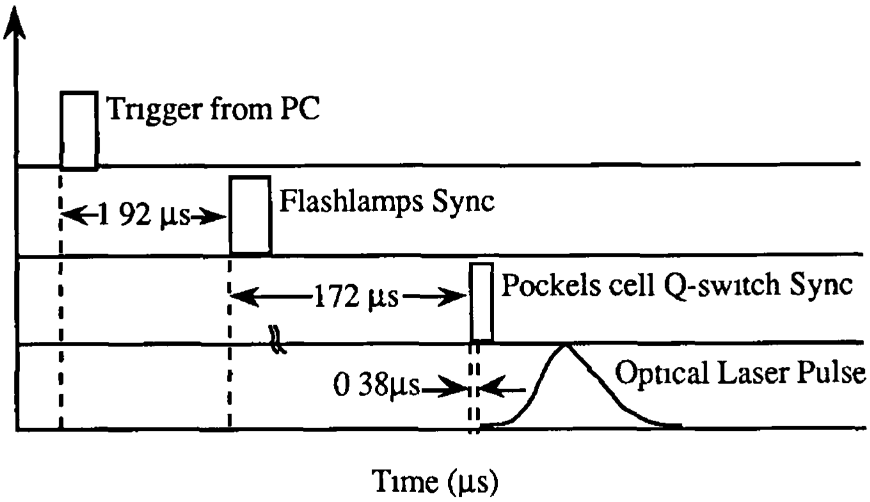

Figure 2.2 Timing diagram for sequence of events in firing the Nd:YAG laser

2.1.1 The Nd:YAG Laser

The laser used throughout this work was a Spectron Laser Systems Q-switched Nd:YAG SL800 laser featuring a two stage oscillator/amplifier system, as shown in figure 2.3. The basic principles of an Nd:YAG laser are briefly discussed in Appendix C. This laser delivered a single optical pulse at 1064 nm (the fundamental frequency), with a FWHM of 10 ns and carrying around 500 mJ of energy. The energy in the laser pulse was measured using a calibrated Radiant Dyes Chemie energy monitor with a sensitivity of 160 mV per Joule of laser energy.

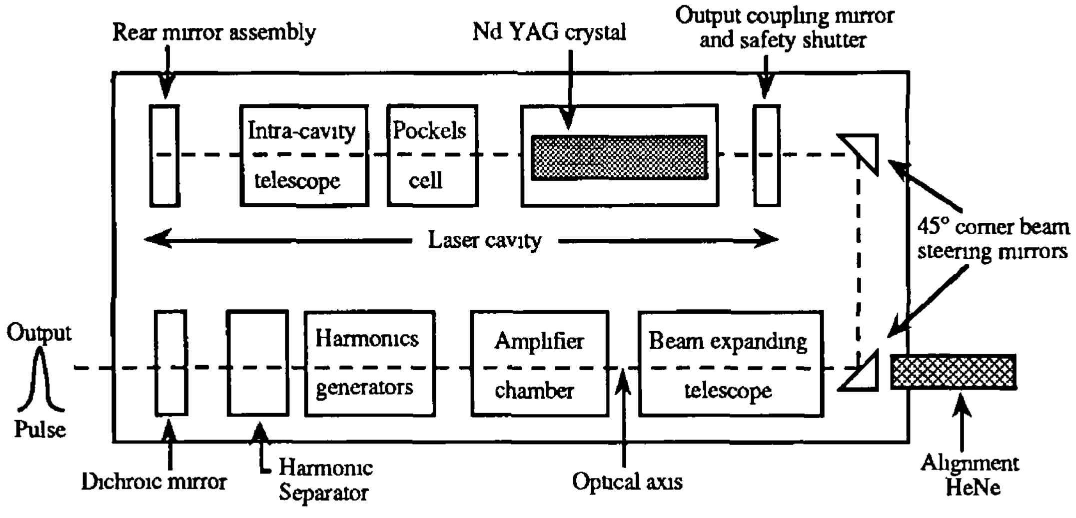

Figure 2.3 Schematic diagram of the Nd:YAG laser head

The laser beam was focussed through a glass window onto the target surface via an f/5, 100 mm focal length plano-convex lens mounted on an X-Y stage outside the vacuum chamber. Focussing was checked by viewing the target surface through a telescope (focussed at infinity) and the lens. The position of the lens was then adjusted until the image of the target was clearly discernable The focussed area size of the beam is ultimately diffraction limited (i e , linear dimensions of the image are of the same order as the laser wavelength) but lens aberrations and the mode structure of the beam increase the spot size to 5 – 100 times the diffraction limit Assuming the laser beam to be a TEM_{00} mode and Gaussian in profile, the radius of the focussed laser spot can be estimated using the following approximate relation

$$\omega \approx \lambda f/\pi\omega_L \tag{23}$$

where ω is the focussed spot radius (1/e of peak axial value), f is the focal length of the lens and ω_L is radius of the laser beam at the input to the lens ω_L may be calculated using

$$\omega(x) \approx x\lambda/\pi\omega_0 \tag{24}$$

where $\omega(x)$ is the beam radius after propagating some distance x and ω_0 is the intracavity beam radius Also, ω_0 may also be approximated by

$$\omega_0 \approx \lambda/\pi\theta \tag{25}$$

where θ is the divergence of the Gaussian laser beam For the Nd YAG laser beam used here, λ = 1064 nm and $\theta \approx 2$ mrad so that ω_0 = 0 16 mm The lens is positioned at a distance of x = 2 5 m from the laser aperture so that $\omega(x = 2\ 5\ \text{m}) = \omega_L \approx 5$ mm Expression (23) now gives the focussed spot diameter, 2ω, equal to ~15 μm The actual diameter of the hole drilled in a zirconium target by the focussed laser beam was measured to be approximately 100 μm in diameter, around 7 times the diffraction limit, which would be expected considering that the Nd YAG laser beam is multimode and that the lens is not aberration-free Therefore, the illuminated target surface area is approximately $\pi(5 \times 10^{-5})^2 \approx 10^{-8}$ m^2

The energy possessed by a 1 064 μm photon is 1 87 × 10^{-19} J For a laser pulse delivering 500 mJ in 10 ns, the power is 50 MW If the area of the focussed beam is 10^{-8} m^2, then the corresponding laser energy density is about 5×10^{15} W m^{-2} (or 5×10^{11} W cm^{-2}) – corresponding to ~10^{34} photons m^{-2} s^{-1} irradiating the target

2.1.2 Layered Synthetic Microstructure (LSM)

Metallic thin-film layers in which the refractive index, n, varies periodically with depth reflect EM radiation at particular wavelengths [81] Reflectivity at the transition between two layers is sizeable only in the case of sufficient discontinuity between the optical densities of the materials At short wavelengths (< 2000 Å) this originates from differences in the absorption coefficient of each layer A layered synthetic microstructure or multilayer, in its simplest form, is made up of two materials, a low atomic-number/low refractive index material (A) and a high atomic-number/high refractive index material (B), arranged alternatively in layers of thickness d_A and d_B respectively, on a smooth substrate The periodicity of this structure is $d = d_A + d_B$ Figure 2 4 schematically illustrates the structure of an LSM The first attempt to produce a stack of very thin metallic layers was made by Deubner [82] Subsequently, Dumond and Youtz [83] successfully manufactured the first multilayer to reflect soft x-rays More recently, Barbee [84] succeeded in producing LSM dispersion elements for use in soft x-ray applications

If the structure consists of L pairs of layers bound by two semi-infinite media, the vacuum and substrate, then the total number of media involved is 2L + 2 As the number of bilayers in a multilayer is increased, the reflectivity increases up to some maximum value which will not increase upon addition of extra layers [85] Reflection from this stacked structure is analogous to Bragg reflection of radiation by crystallographic planes, described by the Bragg equation $m\lambda = 2d\sin\theta_m$, where d is the interplanar spacing and θ_m is the Bragg angle of incidence of the mth-order radiation The Bragg equation must be modified to correct for refraction and absorption effects if it is to give the correct angular position, θ_m^p, and value of the Bragg maximum of diffraction of reflected soft x-rays from multilayers In an absorption-free multilayer, the Bragg equation corrected for refraction [86] may be written as

$$m\lambda = 2d \sin\theta_m^p \, [1 + (\delta_0^2 - 2\delta_0)/\sin^2\theta_m^p]^{1/2} \qquad (26)$$

where δ_0 is the average scattering decrement of the multilayer

Selection of $d_A = d_B$ suppresses even-order (m = 2, 4, 6,) reflections and thus eliminates the need for additional filtering [85] A theoretical analysis of LSMs is given in Appendix A, while a comprehensive review of multilayer optics is given by A G Michette in his monograph entitled “Optical Systems for Soft x-rays” [85]

The multilayer used in this experimental arrangement had 25 bilayers and used a nickel (80%) – chromium (20%) alloy as the high refractive index material and carbon as the low refractive index material, with $d_A = d_B = 37\ 35$ Å The substrate was a semiconductor grade, high resistivity silicon (111) wafer Figure 2 5 shows the theoretically predicted and measured reflectivities as a function of incident photon energy for such a multilayer configuration subtended at an angle of incidence of 45° to the incoming radiation The theoretical data was calculated using a code written by Cafolla [87] The actual reflectivity of the LSM was measured by S Bac and collaborators at the Université Pierre et Marie Curie in Paris using SuperACO synchrotron radiation monochromatised with a plane grating The energy position of the measured peak reflectivity occurs at 125 4 eV with a FWHM of 6 eV The peak reflectivity is 8 5%, that is, ~63% of the theoretically predicted value Such discrepancies are commonly observed when comparing theoretical and measured reflectivities A number of reasons can be invoked to explain this, such as, interface

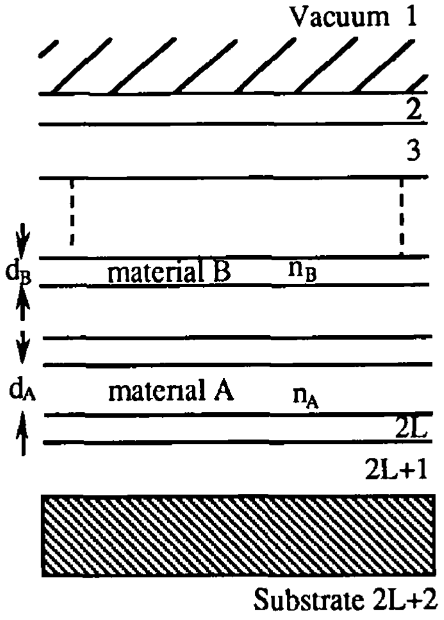

Figure 2 4 Schematic representation of a multilayer thin-film Subscript 'A' represents the low refractive index layer and subscript B represents the high refractive index layer

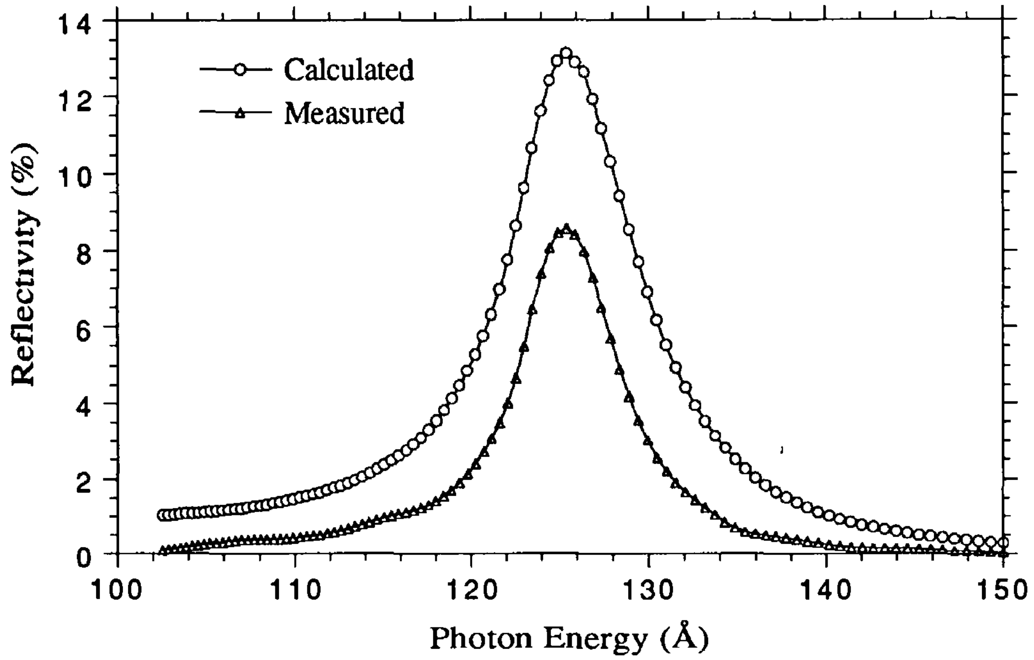

Figure 2 5 Measured and calculated reflectivities as a function of incident photon energy for a NiCr/C multilayer with L= 25 bilayers, periodicity d = 74 7 Å, and positioned at an angle of 45° to incident radiation

roughness, random errors in the thickness of layers, interdiffusion between layers resulting in index gradients and so forth [85]

The NiCr/C multilayer has a wavelength-dependent efficiency associated with it, i.e., the multilayer does not reflect all energies with the same efficiency. This dependence has been developed in Appendix A and the results plotted here in figure 2.6. For unpolarised radiation incident at an angle of 45°, or Brewster's angle, the electric field component of the radiation which is parallel to the multilayer interface (π-polarised) is absorbed, leaving only the perpendicular or σ-component. At angles other than the 45° position, the contribution from π-polarised radiation increases the overall integrated energy reflected.

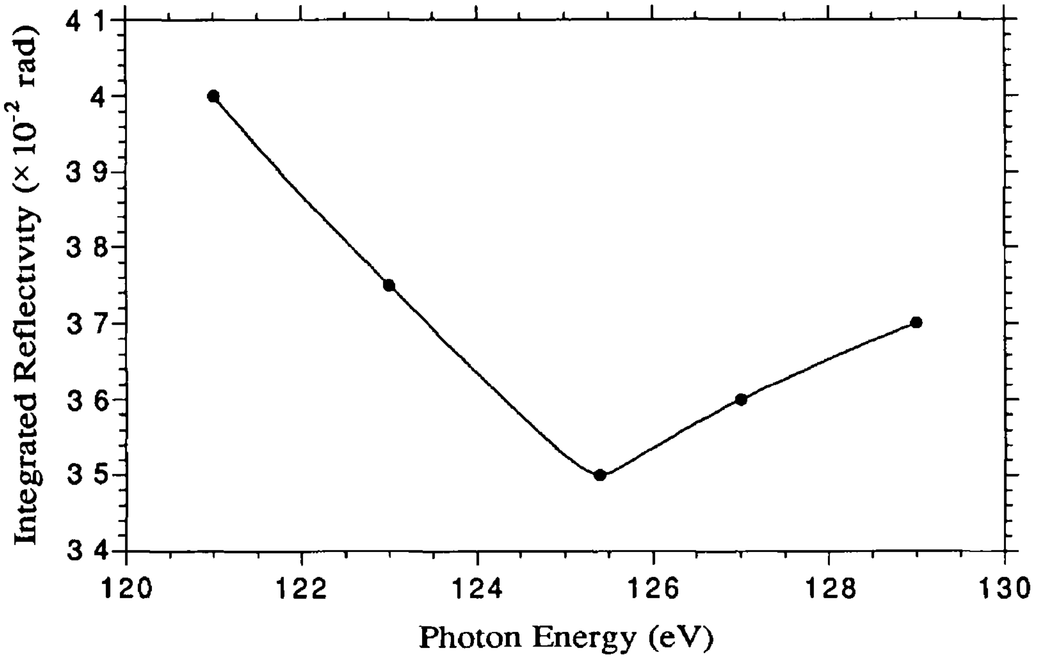

Figure 2.6 The efficiency curve of the NiCr/C multilayer as a function of energy

2.1.3 The XUV Detector

The detection system used to measure the XUV emission from the laser-plasmas was based on a thin-film C/Ag composite – interference filter for XUV filtering and scattered laser light rejection and a scintillator/photomultiplier as the detector as shown in figure 2.7. The multilayer also behaved as a narrowband filter. The emitted radiation from the LPP was firstly attenuated by the multilayer as characterised in section 2.1.2. Subsequently, the reflected radiation was further filtered and attenuated by the thin-film composite filter. The XUV radiation was then down-converted to visible light by the scintillator. At this point, the fluorescence was further filtered by the interference filter which selected a narrow band of the fluorescence light to be passed onto the photomultiplier. The detector was mounted on

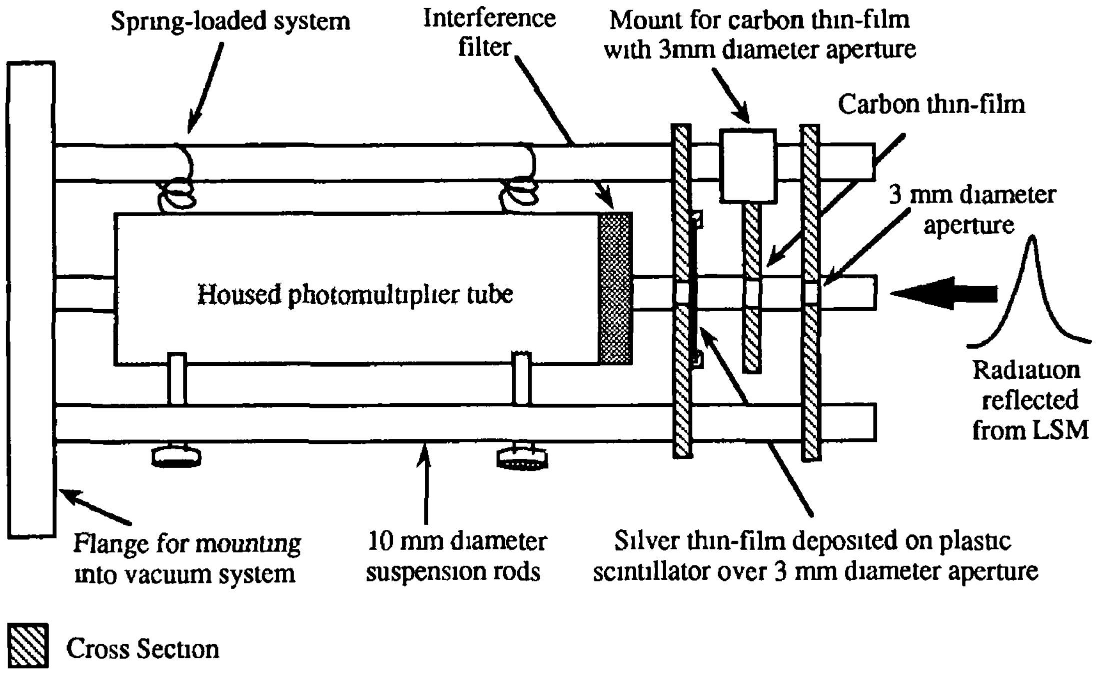

Figure 2 7 The XUV detector and its carriage

a three rail spring-loaded system which was inserted into one of the arms of the multilayer vacuum chamber (see figure 2 1)

2 1 3.1 Composite Filter

Any radiation transmitted that is not within the bandpass of the multilayer was unwanted background radiation (laser and VUV to visible radiation from the plasma) and therefore had to be eliminated from the detected pulse To this end, optical filtering was achieved using a carbon/silver thin-film composite The characteristic transmission curve of a carbon thin-film shows a window in the XUV above 50 Å, where its absorption coefficient ranges from < 1 μm^{-1}, up to ~8 μm^{-1} at 150 Å as shown by figure 2 8 From this point onwards, the coefficient increases to 190 μm^{-1} at 800 Å but begins to transmit well again as the wavelength approaches the ultraviolet (figure 2 9) and visible spectral regions This clearly presents a problem with background radiation in the detected XUV pulse However, combining carbon with a filter that has a similar transmission window in the XUV and complementary transmission characteristics elsewhere would resolve this dilemma Silver is an excellent choice for this purpose as it transmits soft x-rays from 32 to 100 Å where the absorption coefficient is < 10 μm^{1} (figure 2 10), blocks visible light in sub-micron thicknesses, and attenuates strongly in the 120 – 3100 Å region as shown in figure 2 11

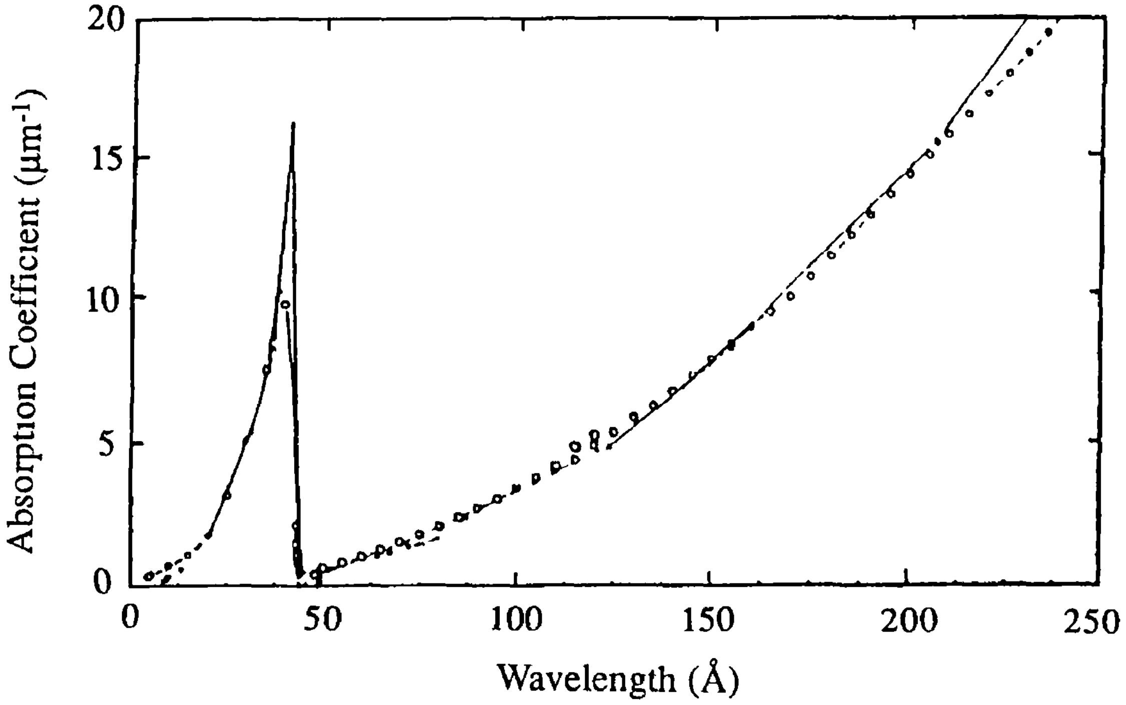

Figure 2 8 Linear absorption coefficient of carbon out to a wavelength of 250 Å [88]

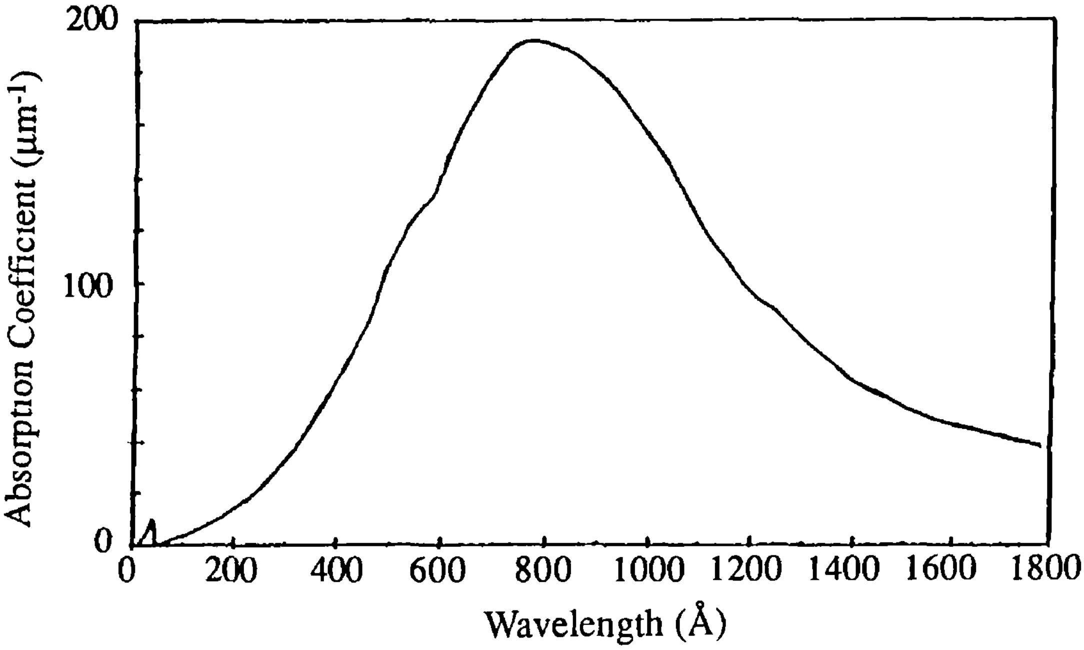

Figure 2 9 The linear absorption coefficient for carbon up to 1800 Å [88]

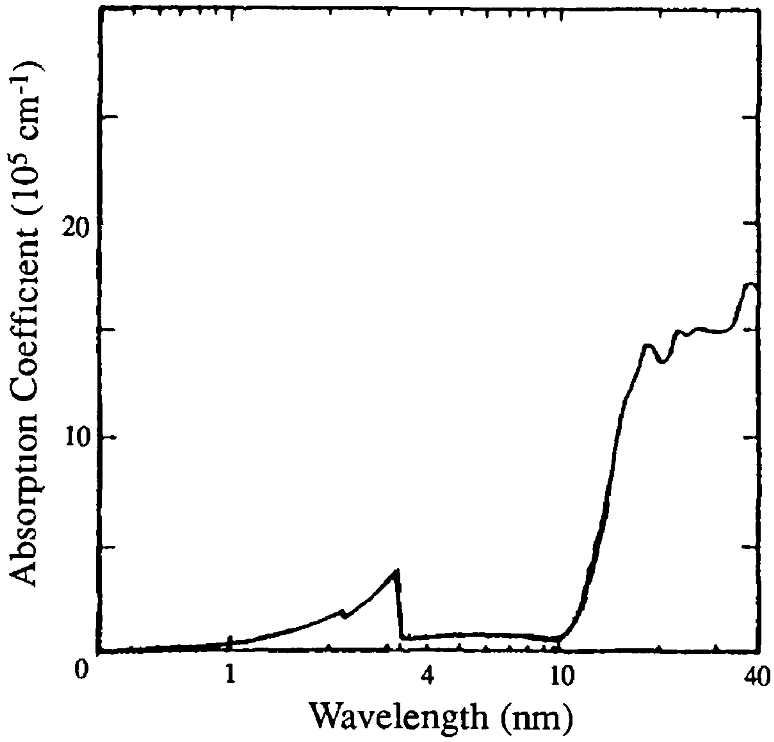

Figure 2 10 The linear absorption coefficient of silver between 4 and 400 Å spectral region [89]

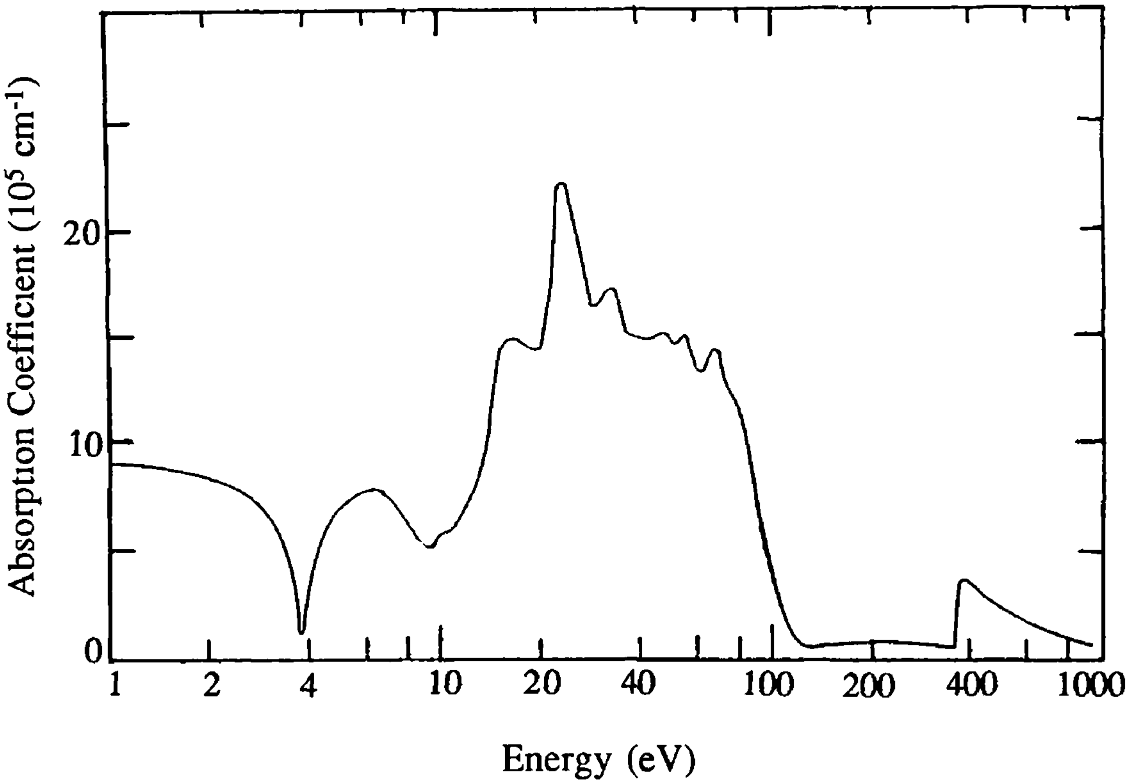

Figure 2 11 The absorption coefficient of silver [90]

A film of silver 0 1 ± 0 01 μm in thickness was prepared on a plastic scintillator's smooth substrate by vacuum deposition and the thickness measured using an ellipsometric thickness monitor

The transmittance (T), a dimensionless ratio of transmitted power (I) to incident power (I_0), of a filter at a particular wavelength may be predicted using the simple relation

$$T = I/I_0 = \exp(-\mu x) \qquad (27)$$

where μ is the absorption coefficient of the material at the chosen wavelength and x is the thickness of the filter The overall transmittance of a composite filter can be computed as the product of the predicted transmittance of the films at each wavelength Using absorption coefficient data extracted from figures 2 8 and 2 10, the transmittance as a function of photon energy of each filter and the composite was calculated using expression (27) The resulting transmittance curves are shown in figure 2 12 The thickness of the carbon filter used in this experiment was 0 44 μm

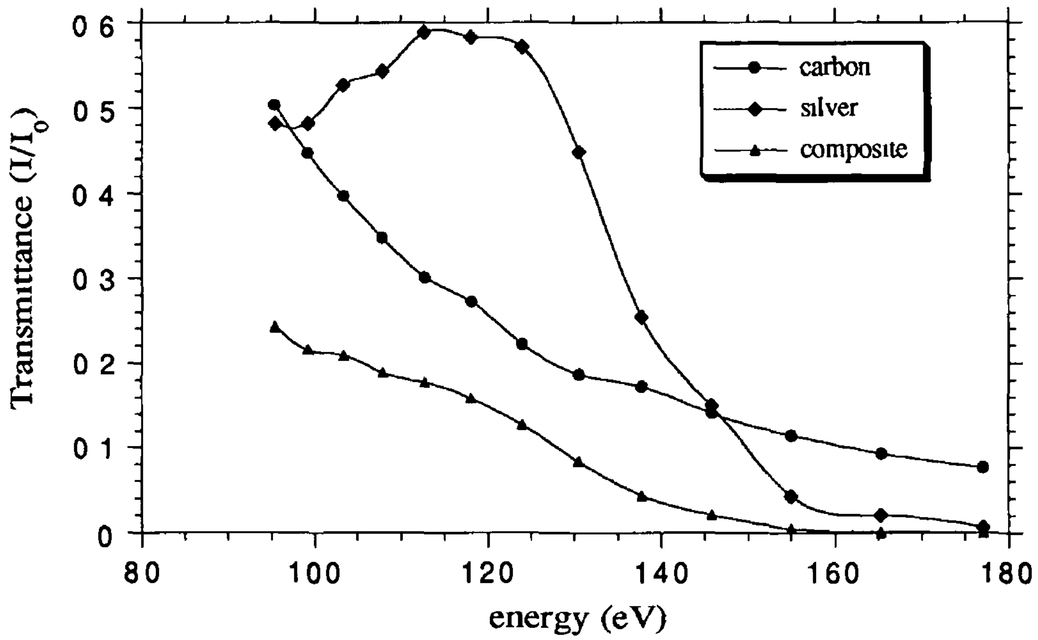

Figure 2 12 The transmission of carbon, silver and composite filters in the 105 – 145 eV region

2.1.3.2 Scintillator

A scintillator is a material that can convert XUV photons to visible light by absorption of the soft x-ray radiation and reemission through fluorescence The scintillating material used in these experiments was plastic NE102A (a polymerised form of organic-based scintillators) which has a peak fluorescence wavelength at 4200 Å (figure 2 14) and a fluorescent decay time of 2 2 ns [12] The spectral profile of the fluorescence output from the scintillator is independent of incident wavelength, so that subsequent narrowband filtering of this fluorescent emission by an interference filter does not affect the relative intensities of the detected XUV emissions (see figure 2 14)

Compared with other scintillators, NE102A has a slightly better conversion efficiency than the organic-based tetraphenylbutadiene (TPB) and a lower efficiency but faster decay time than sodium salycilate (7 – 12 ns) [12] NE102A requires no special preparation and is commercially available in thin sheets down to 5 μm thick NE102A has an extremely smooth surface which makes it is possible to deposit thin-films on its substrate When metallic thin-films are evaporated onto scintillators, their effective transmittances are increased since they reflect the fluorescence radiation which would otherwise escape detection A scintillator thickness of 500 μm was used throughout this work, which was sufficiently thin to ignore fluorescence reabsorption effects yet thick enough to deposit silver upon and to handle and mount with ease

2.1.3.3 Interference Filter

The interference filter (I/F) used in this detector was a visible narrowband (or bandpass) Ealing Electro-Optics filter that passes radiation at a peak wavelength of 4466 Å (figure 2 13) and a peak transmission 62% with a FWHM of 393 Å

The I/F transmitted only a narrow portion of the fluorescent emission of the NE102A which then propagated to the photomultiplier tube for detection

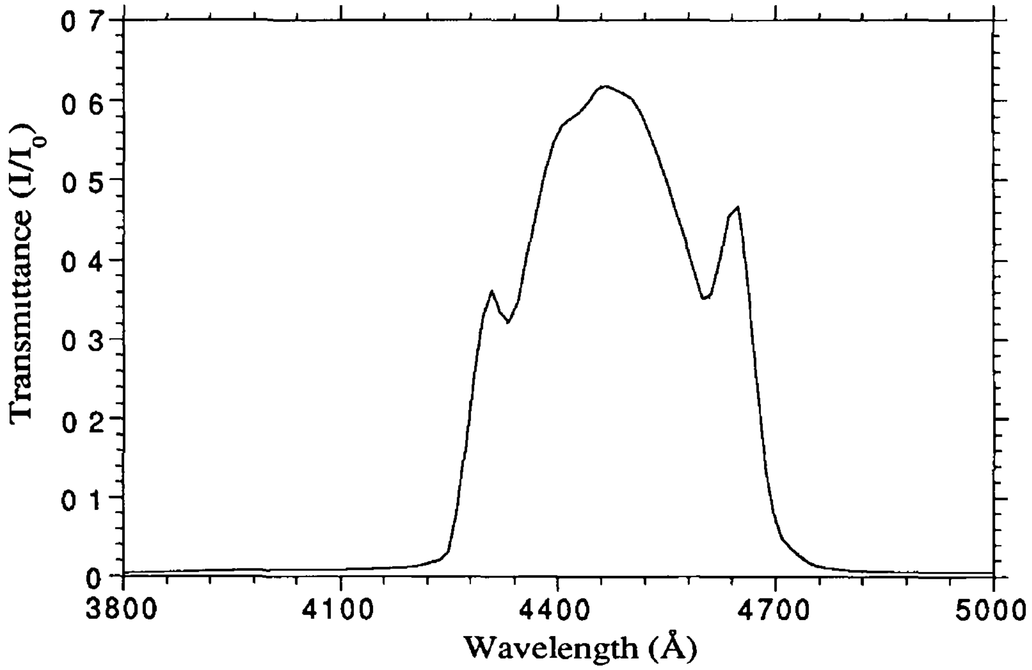

Figure 2 13 The transmission profile of the Ealing Electro-Optics interference filter

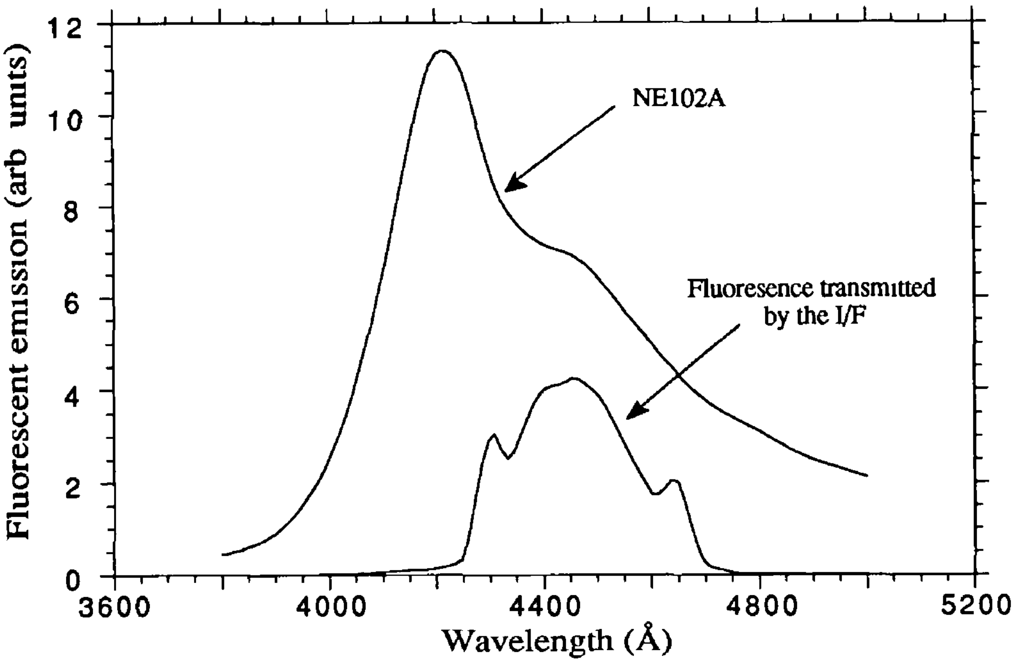

Figure 2 14 The fluorescent emission of NE102A plastic scintillator and the portion of this emission transmitted by the interference filter

2.1.3.4 Photomultiplier Tube

The photomultiplier tube (PMT) used here was a Hamamatsu R1450 head-on photomultiplier with a peak transmission at 4200 Å and a spectral range of 3000 to 6500 Å The PMT was operated at a voltage of 1 5 kV throughout all experiments, unless otherwise stated, providing a current gain of about 2×10^6 The rise time of the device is 1 8 ns

2.1.4 Temporal Response

All XUV pulses measured on the scope were dispersed or broadened in time by the response time of the system components To estimate the actual pulse duration it was therefore necessary to calculate the overall system response time Thus, the mechanisms responsible for the pulse broadening must be recognised, these are the scintillator decay time T_S, the photomultiplier rise time T_{PMT}, the RC time constant of the electrical cable connecting the detector and scope, and finally the rise time of the Hewlett-Packard scope T_{HP} The rise (or fall) time here is taken as being the 10 - 90% (or vice versa) temporal response The system rise time τ_{SYST} may be calculated from the rise times of the individual components using the expression [91]

$$\tau_{SYST} = 1\ 1(T_S{}^2 + T_{PMT}{}^2 + T_{50\Omega}{}^2 + T_{HP}{}^2)^{1/2} \qquad (28)$$

where $T_{50\Omega}$ is the rise time of the 50 Ω coaxial cable The cable may be represented by an RC filter as shown in figure 2 15 The RC fall time may be calculated using

$$T_{50\Omega} = 2\ 2RC \tag{29}$$

where the coaxial cable resistance $R = 50\ \Omega$ and C is the capacitance which was measured by a capacitance metre to be 150 pF for a cable length of 1 5 m Using

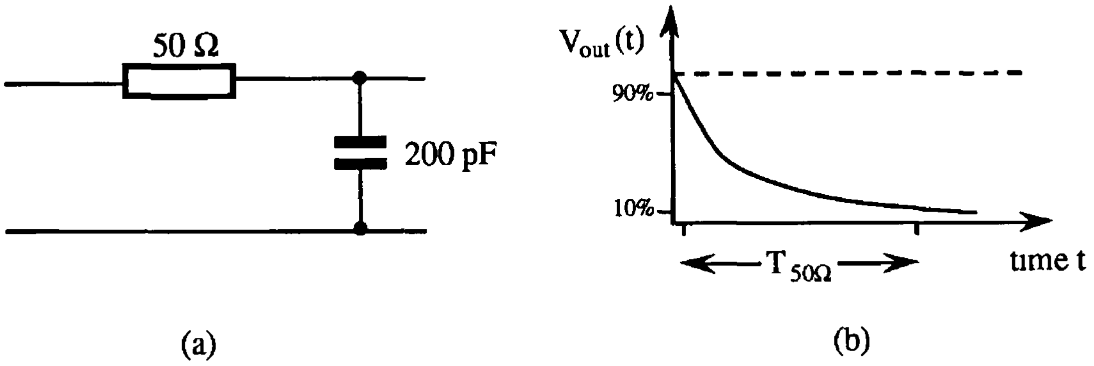

Figure 2 15 (a) A low pass RC filter circuit equivalent to the resistance and capacitance of the coaxial cable and (b) the circuit discharge response as described by the equation $V_{out} = V_{in}\ (1 - \exp(-t/RC))$

these values , one finds $T_{50\Omega} = 16$ ns From the specifications of the scope, one finds that $T_{HP} \approx 3\ 5$ ns Now inputting each of the component rise and fall times into equation (28) gives $\tau_{SYST} \approx 17$ ns

It is clear that measurement of the pulse duration is bandwidth-limited, since the XUV pulse length is as long as the system response time The rise time of the pulses is relatively fast (< 8 ns) but these are RC-limited on the fall time Thus, little information can be gained from measurement of the pulse duration other than to say that the XUV emission occurs in a FWHM time window of 17 ns or less

2.1.5 Target Chambers and Vacuum System

Due to the wavelength range of the radiation being examined, it was necessary that all measurements be carried out under high-vacuum conditions (sub–10^{-4} mbar) to avoid absorption of the XUV radiation by air molecules The target chambers already existed from previous projects The multilayer chamber was designed by J Costello at DCU and built at the UCD engineering workshop The sample chamber was designed by J P Mosnier at DCU and built at the UCC engineering workshop

All hardware was machined of stainless steel, a metal with very low outgassing properties A multilayer mount was designed by the author which allowed rotational and orientational adjustments to the multilayer mirror, and is shown in figure 2 16 The multilayer was fixed with a film of vacuum grease to the front block The dimensions of the window in the front block were 13 × 8 mm Four M3 allen screws in a spring-loaded design allowed a wide degree of movement for mirror alignment The cylindrical piece at the top of the mount was locked into the receiver which allowed the multilayer mount to be rotated via an external, degree-calibrated dial The multilayer could be locked into position when the 45° incidence angle was located

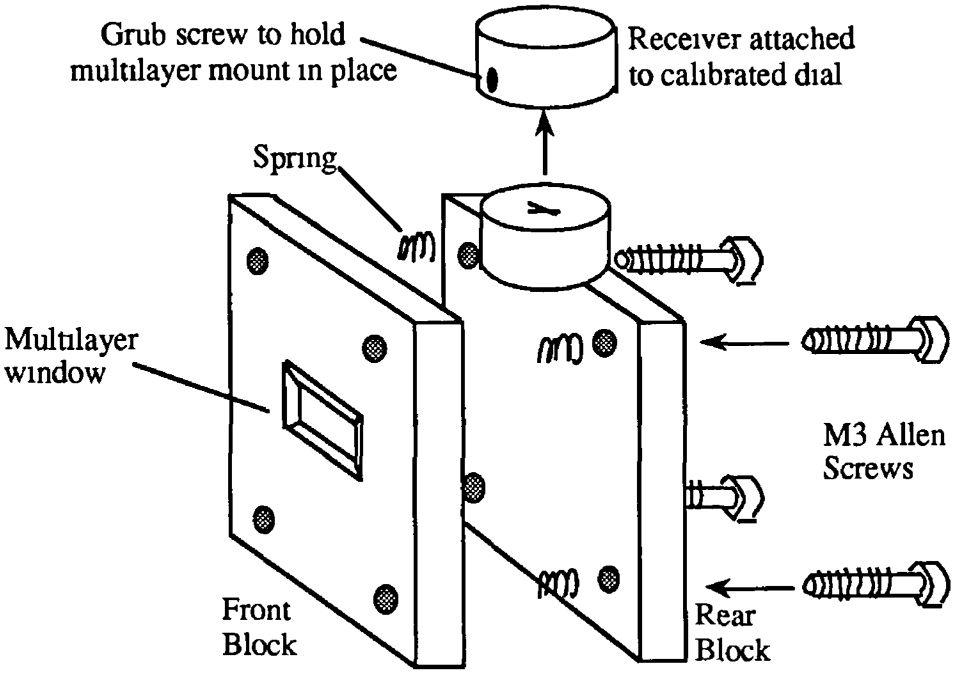

Figure 2 16 The multilayer mount

Four planar targets were mounted at once using the design shown in figure 2 17 Cylindrical targets could only be mounted one at a time which required a break of vacuum for each cylindrical target change

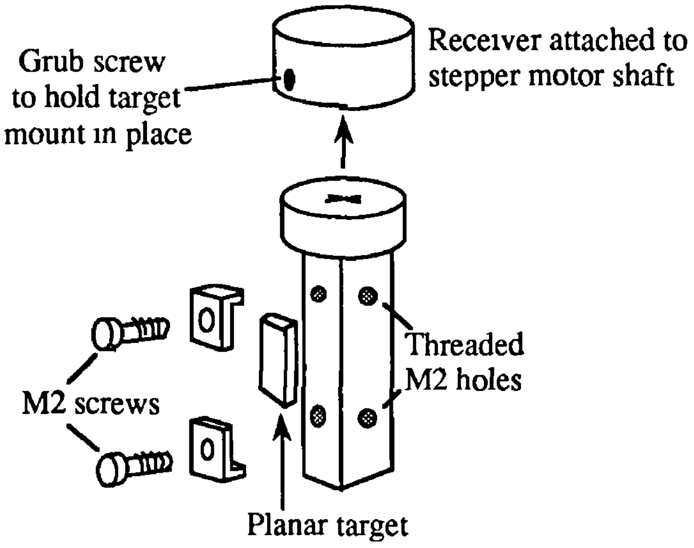

Figure 2 17 The target mount

Irradiation of targets with a focussed high-power laser beam leads to the formation of microcraters Therefore, it is desirable to move the target periodically after a number of laser shots, which will depend on the properties of the target element A software-controlled stepper motor was employed to rotate targets to refresh the surface and thus avoid burial of the laser-plasma in the metal

Evacuation of the system required two rotary-diffusion pump rigs (the volume of vacuum space being too large for efficient pumping with a single rig) The Edwards two-stage rotary pumps reduced the internal pressure to $\sim 10^{-1}$ mbar, at which stage the diffusion pumps could operate (figure 2 18) The ultimate pressure obtainable with this system was 1×10^{-5} mbar (which took about 15 minutes providing the system was being regularly used) The rotary and Diffstak™ diffusion pump were connected to the target chamber by corrugated stainless steel pipes to allow flexibility and to decouple the system from added vibrations The multilayer chamber was evacuated by a Leybold-Heraeus diffusion pump The two chambers were connected by a 79 mm internal diameter pipe into which the collimating apertures were mounted The detector's output signal and ground lines were taken out from vacuum to the scope via a Caburn-MDC electrical feedthrough and terminated with a 50 Ω impedence

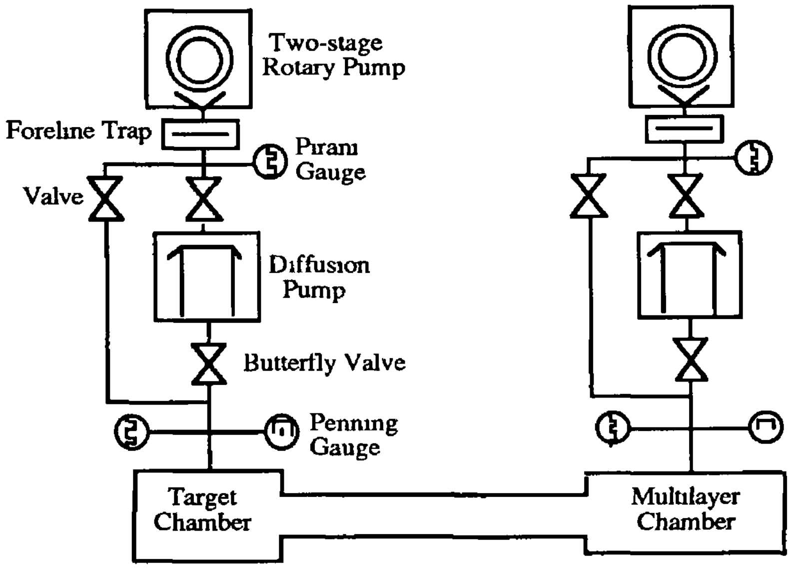

Figure 2 18 Schematic of vacuum system[1]

2.1.6 Performance Tests

A typical output pulse from the XUV flux measurement system is displayed in figure 2 19 It was important to routinely check the filtering performance of the system A simple test was employed to ensure that only the desired XUV radiation was being detected This involved the positioning of a glass microslide in the optical

---

[1] ISO Standard Graphic Symbols [92] are used

path between the plasma source and multilayer No window materials transmit radiation below 1024 Å [12], therefore, only lower energy radiation reaches the filtering system If the XUV filter is operating properly, then none of this radiation should appear at the input to the photomultiplier tube The results of this test offered information on the condition of the thin-films, e g, whether a filter had a pinhole in it or not, and whether scattered laser radiation was present When a pinhole was present, the output pulse had a strong, prompt and sharp peak corresponding to scattered laser radiation superimposed on the broad pulse (lasting 100's of nanoseconds) originating from XUV to visible radiation emitted from the plasma

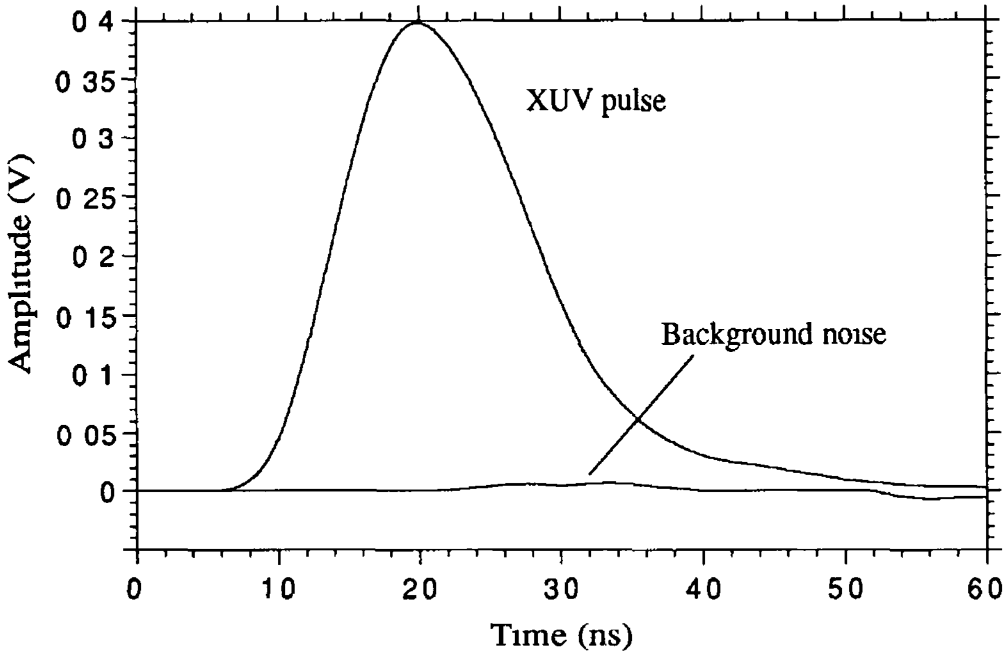

Figure 2 19 Typical output pulse and background signal from the XUV flux measurement system The measured FWHM of the XUV pulse is around 17 ns

The nanosecond time-scale on the x-axis of figure 2 19 is not an absolute scale, i e , the XUV pulse is not detected 10 ns after the laser pulse is emitted The time-scale is a result of the triggering set-up within the oscilloscope Results presented in chapter 4 are shown with the same time scale The only time information to be gleaned from these spectra is the temporal pulse width as discussed in section 2 1 4

The target surface was refreshed after every five shots by rotating the cylindrical targets through ~10° For planar targets the stepper motor shaft was rotated through 320° which returned the target face to its original direction but the surface was refreshed because of the screw action within the stepper motor shaft which altered the target position vertically with respect to the laser beam In this situation, a constant direction of rotation was necessary each time for the planar target to ensure the orientation of the target face to the optical axis remained unchanged This was necessary because of a small degree of "play" in the rotation of the stepper motor shaft

2.2 Bandpass of the XUV Flux Measurement System

Two effects are determining the energy bandpass of the LSM system These are (i) the resolving power of the multilayer and (ii) the collimating apertures or slits These slits have a certain width which corresponds to a wavelength spread $\Delta\lambda$ This effect would be present even if the effect (i) was not present The instrumental line profile is therefore a convolution of these two effects, i e

$$P(\lambda) = P_1(\lambda) \otimes P_2(\lambda) \qquad (30)$$

where $P_1(\lambda)$ represents the influence of the slits and $P_2(\lambda)$ represents the influence of the limiting resolution of the instrument The corresponding broadenings are $d\lambda_s$ (slit image width) and $d\lambda_r$ (instrumental width) respectively In an ordinary spectrometer or monochromator (i e , grating or crystal), $d\lambda_r$ is extremely small, so that they operate way above their resolution limit In such instruments, the slits widths are the dominating factor In the present case, it is likely that both quantities will be comparable Assuming Gaussian profiles, the bandpass is given by the square root of the addition of the squares of the quantities, or

$$BP = [(d\lambda_s)^2 + (d\lambda_r)^2]^{1/2} \qquad (31)$$

The effects of diffraction, aberrations, and so forth, are being neglected here It is also being assumed that the linewidth of the grating used to measure $d\lambda_r$ at SuperACO is negligible

2.2.1 Geometry of the Instrument

Figure 2 20 shows the geometry of the measurement system For a narrow slit at a fixed angle with respect to the multilayer, one has a situation equivalent to a monochromator mode However, in this case, the apertures are wide compared to the angular resolution of the multilayer so that the system is really a mixture of an imaging and a monochromator system The dimension of the plasma source is about 100 μm This is extremely small compared with the geometrical dimensions of the apertures Thus one can say that pinhole effects will be negligible It is nevertheless important to take into account the influence of these apertures as the entrance "arm" of the instrument is very long This implies that the f/value at the entrance will also be very long, thus making the angular acceptance of the instrument very limited In the approximation of a point source, the energy bandpass of the instrument is limited, i e

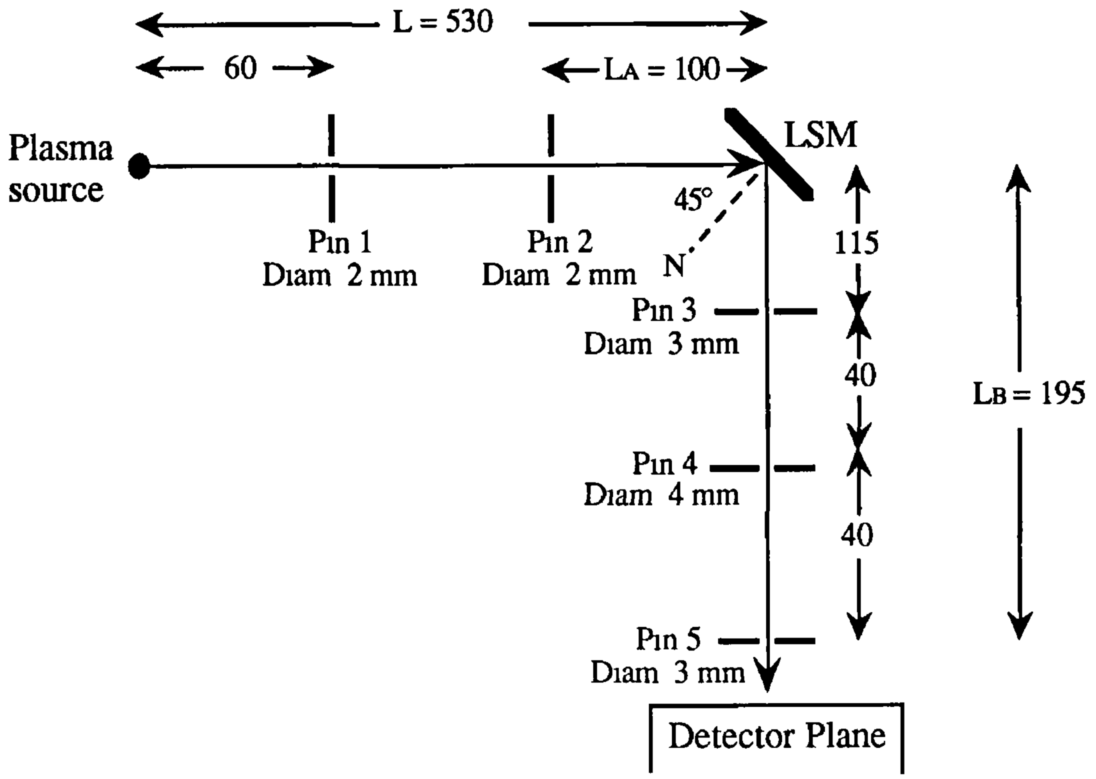

Figure 2 20 Geometric arrangement in LSM system Measurements are in millimetres Diam is the diameter of the aperture

the narrower the range of angles allowed, the narrower the spectral energy band reflected This stems from Bragg's Law which dictates that for one direction (θ), only one energy (λ) is reflected

One may define light gathering power of the system by its numerical aperture (NA) and f/value The maximum range of possible angles incident at the LSM is determined by Pin 2 From figure 2 20, the NA is then (since angles are small)

$$NA \approx (1/430) \approx 2\ 32 \text{ mrad}$$

The F number is equal to

$$1/(2NA) = f/(2 \times 2\ 32 \times 10^{-3}) = f/215$$

The corresponding solid angle is given by

$$\pi(1 \times 10^{-3})^2 / (430 \times 10^{-3})^2 = \pi/430 = 7\ 31 \times 10^{-3} \text{ sr}$$

2.2.2 Linear Dispersion

The wavelength spread at the position of the multilayer (i e 530 mm from the laser-plasma) about the mean ray at 45° (which corresponds to an energy of 125 4 eV) must be calculated In order to do this, one has to differentiate the corrected Bragg Law to calculate $d\lambda/dx$ Also $\Delta\lambda/\Delta x$ is obtained from $\Delta\lambda/\Delta\varphi$, where $\Delta\varphi = \Delta x/L$ as shown in figure 2 21

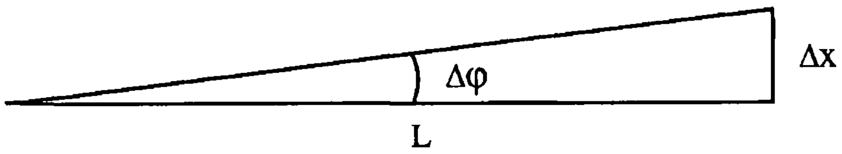

Figure 2 21 The half angle energy spread at the LSM

In order to simplify differentiating the corrected Bragg's Law, one may write

$$m\lambda = 2d\sin\varphi_i\,[1 + (\delta_0^2 - 2\delta_0)/\sin^2\varphi_i]^{1/2}$$
$$\cong 2d\sin\varphi_i\,[1 + (\delta_0^2 - 2\delta_0)/2\sin^2\varphi_i] \qquad (32)$$

Upon differentiating

$$d\lambda/d\varphi_i = d/d\varphi_i\{2d\sin\varphi_i[1 + (\delta_0^2 - 2\delta_0)/2\sin^2\varphi_i]\}$$
$$= 2d\{\cos\varphi_i\,[1 + (\delta_0^2 - 2\delta_0)/2\sin^2\varphi_i] + [-\cos\varphi_i(\delta_0^2 - 2\delta_0)/\sin^2\varphi_i]\}d\varphi_i$$
$$= 2d\{\cos\varphi_i\,[1 + (\delta_0^2 - 2\delta_0)/2\sin^2\varphi_i - (\delta_0^2 - 2\delta_0)/\sin^2\varphi_i]\}d\varphi_i$$
$$= 2d\cos\varphi_i\,[1 - (\delta_0^2 - 2\delta_0)/2\sin^2\varphi_i]d\varphi_i \qquad (32)$$

The linear dispersion is then

$$\Delta\lambda/\Delta x = (2d/L)\cos\varphi_i\,[1 - (\delta_0^2 - 2\delta_0)/2\sin^2\varphi_i] \qquad (33)$$

From Appendix A, it may be shown that the average scattering decrement, δ_0, for the NiCr/C multilayer is given by

$$\delta_0 = \delta_{NiCr} + \delta_C \qquad (34)$$

where δ_{NiCr} = 0 044 and δ_C = 0 0184 Therefore, one finds that δ_0 = 0 0314 at an energy of 125 4 eV Using d = 74 7 Å, the linear dispersion is

$$\Delta\lambda/\Delta x = 0\ 173\ \text{Å mm}^{-1}$$

In energy, this becomes 0 22 eV mm^{1}

2.2.3 Calculation of the Bandpass

The total energy spread at the multilayer is given by multiplying ΔE/Δx by 2Δx as determined in section 2 2 1, that is, the diameter of the cone of radiation at the multilayer position Therefore, the bandpass due to Pin 2 is 0 54 eV which is small compared with the resolution of the multilayer From equation (31) the total bandwidth of the instrument is then

$$BP = [(6)^2 + (0\ 54)^2]^{1/2} \approx 6\ 03\ \text{eV}$$

with $d\lambda_r = 6$ eV taken from figure 2 5

From figure 2 20, the equivalent projected width of Pin 2 at the position of the detector can be calculated as 2 × (L + LB) × 2 32 mrad ≈ 3 4 mm The width of Pin 5 is 3 mm which implies a loss of bandpass The two aperutres at Pin 2 and Pin 5 are not matched and, ultimately, this must be taken into account when calculating the final throughput of the instrument One has to introduce a transmission factor, F, which takes into account this geometric loss

2.3 Software Interfacing

It was necessary to write a software package to control the firing of the Nd YAG laser, to rotate the stepper motor, and to retrieve and process data from the oscilloscope The interface used to achieve this is dealt with in two parts the IEEE-488 GPIB-PC interface and the applications program developed in Turbo C to control the system hardware and data acquisition

2.3.1 IEEE-488 Interface

A General Purpose Interface Bus (GPIB) was the link used to allow communication between interconnected electronic devices (computer, oscilloscope and plotter) GPIB implements the IEEE-488-1978 international standard for information transfer between computers and electronic devices The IEEE-488 interface card used in this work was a PC-labcard PCL-848A/B This card has a dip switch setting that allows the card to emulate a National Instruments PCII interface card, thereby allowing the use of NI-488 software for instrument control

A Talker sends messages to one or more Listeners The Controller manages the flow of information on the GPIB by sending commands to all devices Devices can be talkers, listeners and/or controllers In this experimental arrangement, the GPIB interface and associated software acted as the Controller, handling the transfer of messages between the computer and the scope and plotter, which both acted as Talkers and/or Listeners

The GPIB-PC software package has a number of control files and utility programs that are necessary for successful implementation GPIB COM is a device file handler (loadable device driver) for the GPIB that is loaded at system start-up by the DOS operating system It contains symbolic names, primary and secondary addresses as well as all other characteristics of the devices and boards in the system IBCONF EXE is a utility configuration program that allows one to edit the software parameters and other data used by the file handler Whenever a change to GPIB COM has been made using IBCONF EXE, the computer must be rebooted in order to activate the change(s) Both the GPIB COM and IBCONF EXE files must be installed in the root directory of the boot drive

Once the card is installed in the computer, a batch file called IBSTART EXE is run to test the hardware installation before the GPIB software is configured and installed If successful, the file creates a directory called GPIB-PC and to it copies the GPIB software Next, it modifies the DOS system configuration file CONFIG SYS to contain the line

DEVICE=GPIB COM

During boot-up, DOS reads this file and installs new device drivers and handlers

Communication, without the need for an applications program, between the PC and a connected device is possible using IBIC EXE, an interactive control program that allows execution of the handler functions from the keyboard This is an extremely useful tool that helps the user to test the board/instrument functions, to program the instrument and develop an applications program

Communication between interconnected devices is achieved by passing messages through the interface system The GPIB carries two types of messages device-dependent messages and interface messages Device-dependent messages contain device specific information such as programming instructions, measurement results, data files and machine status Interface messages manage the bus itself They perform such functions as initialising the bus, addressing and unaddressing devices, and setting device modes for remote and local programming

2.3.2 Turbo C Applications program

GPIB-PC functions are high-level and low-level functions that communicate with and control devices on the GPIB High level functions automatically execute sequences of commands that handle bus management operations such as reading from and writing to devices and polling them for status These functions do not require the user to understand the GPIB protocol and bus management details All devices are addressed before the message is sent and unaddressed afterwards On the other hand, low-level functions perform primitive operations that require the user to understand GPIB protocol The program written by the author uses only high-level functions calls

At the beginning of the Turbo C program, a declaration file DECL H must be included This globally defined file declares all GPIB commands and constants that are used throughout the applications program Upon sending a GPIB function call to a board or device in the appropriate language syntax, an input/output (I/O) error check must be done to ensure that the function call was successfully executed The GPIB status, error and count bytes, declared in DECL H, return information corresponding to the error condition, if any, that is discovered A function is included at the end of the program to interpret the error messages

The file TCIBS OBJ is a memory model (in this case, a small size model was satisfactory) which contains the C language interface to the NI-488 MS-DOS handler When TCIBS OBJ is link compiled with the source code MC1000 C, an executable file, MC1000 EXE, is produced permitting access to the handler MC1000 EXE is the applications program which controls the system hardware and handles data acquisition

The device connected to the GPIB card was a Hewlett-Packard 54502A 400MHz programmable digitising oscilloscope (compatible with IEEE-488 Standard) MC1000 EXE communicates with the scope by passing messages over the remote interface using the I/O statements embedded in the instruction set of the computers interface language, i e Turbo C The scope divides a waveform into two separate files a waveform data file and a preamble file The waveform file contains 2000 raw data values that must be converted to voltage and time values by the preamble data (option (g) below) Each file must be read across the GPIB individually to the PC Four waveform memories are available to the scope in which waveforms may be stored for further processing

The menu of options available in the executable program MC1000 is shown in figure 2 22 Each option will now be briefly discussed

Program Options

(a) Set up stepper motor
(b) Set up oscilloscope
(c) Alignment/Waveform memory clear
(d) Run experiment
(e) Hardcopy to HP plotter
(f) File averaging
(g) File conversion
(q) Exit

Figure 2 22 Menu of options available with MC1000

The flow chart of figure 2 23 describes the format in each of the options listed in figure 2 22 Upon entering an option, the user is offered the choice of reading information relating to that option (omitted from the flow chart) Once each option has been executed, the user is returned to the program menu

Option (a): This option allows the user to set the stepper motor parameters to be used in an experiment The angular increment for the stepper motor can be from 0° to 360° in intervals of 1 8° Rotation may be clockwise or anticlockwise The 4-phase unipolar stepper motor drive board (stepper motor controller) was interfaced to the Tandon 286 PC/AT using an add-on PCL-720 Digital I/O card which was programmed in this option

Option (b)· The digitising oscilloscope can be operated in local or remote mode This function localises the scope (which is already in remote mode), allowing the user to adjust the operational settings When the user is satisfied with the settings, the scope is returned to remote programming mode The scope settings may be stored at a specified file address in the PC memory

Option (c): Firstly, for ease of alignment, an optional routine was written which allows the user to fire the laser at will or for a specific number of shots while the target position is optimised On escaping this routine, the program then allows the user to fire the laser and store a recorded signal at an already specified waveform memory The built-in averaging function m the scope requires that the waveform memory (1, 2, 3 or 4) is cleared before the averaging routine begins This may be achieved by disconnecting the PMT signal line from the scope and storing the ground line signal at the intended memory (more on this in option (d))

Option (d): This is the main option from which an experiment is run The user is given an opportunity to set (or reset) the stepper motor parameters Next, the option is given to conduct a single shot routine or an averaging routine In the single shot option, the laser is fired and the XUV flux displayed on the scope When a desired waveform appears, the user may save the signal at an inputted address in the PC The user may exit when satisfied On choosing the averaging option, the user must input the number of laser shots to be fired and the number of shots between each rotation of the stepper motor (if selected) The program then allows the option of automatically or manually executing the firing sequence The scope must be set up in a specific fashion (outlined in the option details) to ensure the procedure runs smoothly The previously cleared memory (see option (d)) must be selected and the signal appearing on the scope stored at that memory using the waveform addition function in the scope Each subsequent waveform appearing on the scope is added to this memory This is done automatically by MC1000 Upon completion of the firing sequence, the accumulated waveform data may be read across to the PC and stored at a specified address

Option (e): Any waveform (whether stored in scope memory or on-screen) may be plotted on the attached Hewlett-Packard 7475A graphics plotter This may be done in remote or local programming mode The plotter was connected to the scope via a GPIB cable

Option (f): Each waveform must be averaged in this routine The program asks the user for the waveform file to be averaged and the number of waveforms added in the file

Option (g): The 2000 raw data points in the waveform file, read across the GPIB, must be scaled for useful interpretation The values used to interpret the data are the X and Y references, origins and increments These values are read from the waveform preamble The formula to convert a data value to a voltage value is

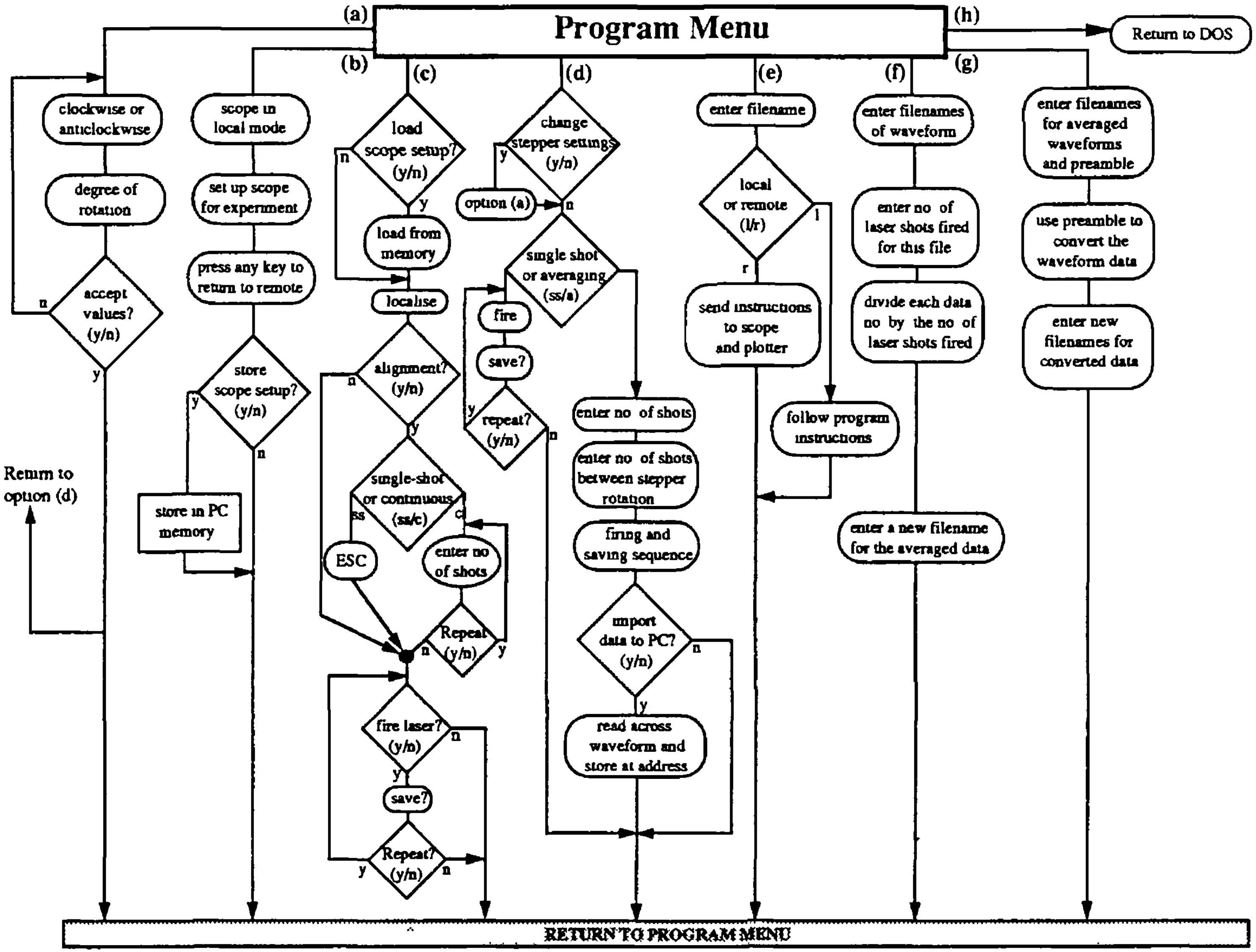

Figure 2.23 Flow chart of MC1000

$$\text{voltage} = [(\text{data value} - \text{yreference}) * \text{yincrement}] + \text{yorigin}$$

The time value of a data point can be determined by the formula

$$\text{time} = [(\text{data value} - \text{xreference}) * \text{xincrement}] + \text{xorigin}$$

Any waveform that is to be converted in this option must first have been file averaged using option (f) to change the format of the data array to one that this option recognises

Option (q): Selecting this option quits MC1000 and returns the user to the DOS operating system

Spectral data files were transferred from the Tandon 286 PC to the Apple Macintosh IIci microcomputer via a TOPS® network Converted data files were processed by Kaleidagraph™, version 2 1, a Macintosh graphics package

2.4 The 2m Photographic Spectrograph

XUV emission spectra from highly ionised first transition metal series from cobalt through zinc were photographically recorded in 1989 by Costello and Mosnier [78] on a 2 m grazing incidence vacuum spectrograph, model E580, supplied by Hilger and Watts and schematically illustrated in figure 2 24

Plasmas were produced using the Q-switched Nd YAG laser (600 mJ, 10 ns) The target metals used to generate plasmas were cobalt through to zinc which were in both rod and planar form Targets were mounted in holders on the end of a drive shaft in the sample chamber which allowed target rotation in order to provide a fresh surface for repeated plasma production The spectrograph consisted of three main parts, all of which are in a plane perpendicular to the Rowland circle plane (i) an adjustable entrance slit forming a narrow aperture which acted as a line-shape source for the grating, (ii) a 1200 grooves mm^{-1} (1°47’ blaze angle) concave diffraction grating with a radius of curvature of 2 m, which disperses the XUV radiation, and (iii) an XUV sensitive Kodak™ SWR (short wave radiation) glass photographic plate, mounted in a plate-holder, onto which the focussed image of each spectrum was recorded Images produced by this spectrograph are astigamtic (that is, a point in the object plane of the source will be imaged as a line in the image plane of the spectrometer), a property inherent in the concave grating but one which can be compensated for by auxiliary optical elements (such as a toroidal mirror)

The LPP was positioned 6 cm from the slit The slit width was set to 15 µm Emission spectra were averaged over 100 laser shots to produce well blackened images on the plates. Also recorded on each plate was a known reference spectrum of aluminium. Upon substitution of the metal being studied for the reference metal, the only physical change incurred to the system conditions was the repositioning of the baffle with respect to the photographic plate so that the reference spectrum could be imaged adjacent to the spectrum under study. These photographed spectra showed varying dispersion rates across the length of the plates, ranging from 0.11 Å mm^{-1} at the low wavelength end to 0.148 Å mm^{-1} at the high wavelength side. This wavelength-dependent dispersion must be taken into account when measuring the wavelength of the emission lines.

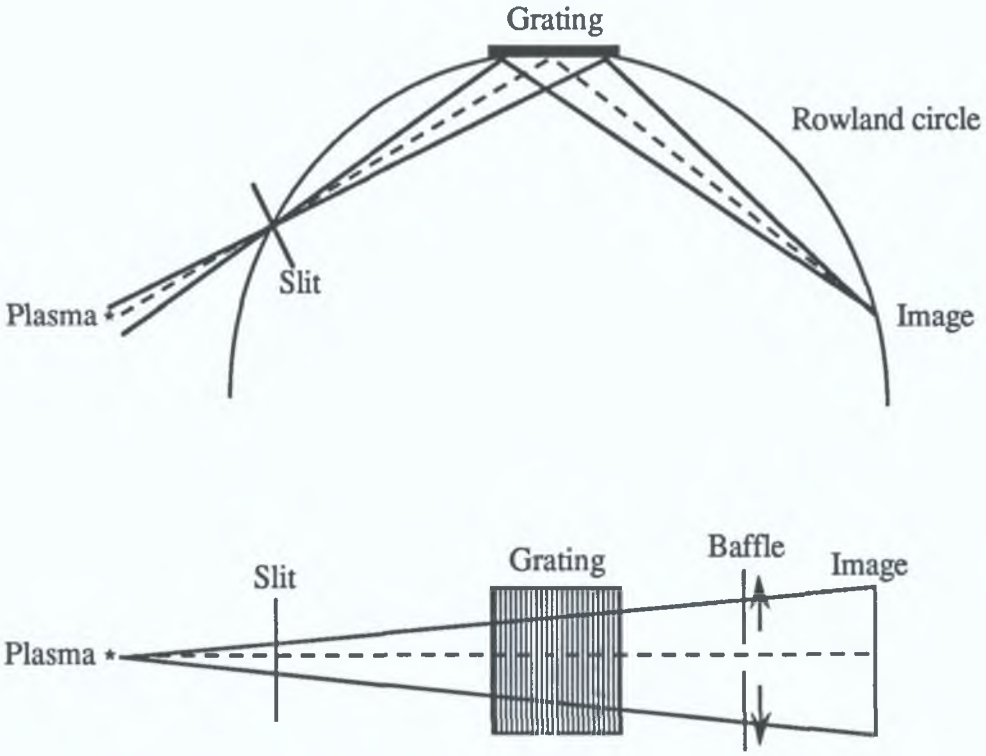

Figure 2.24 Schematic representation of an astigmatic 2m grazing incidence vacuum spectrograph demonstrating the focussing properties of the Rowland circle.

2.5 The 2.2m MacPherson Spectrometer

The XUV pulses recorded on the system described in section 2.1 provide no information on the nature of the radiation (i.e., line and/or continuum and their atomic origins) emitted from the plasma. To better understand the target atomic-number dependence of laser-plasmas, it is necessary to have a knowledge of the radiative characteristics of the plasmas. To this end, emission spectra of these metal plasmas were recorded on a 2.2 m MacPherson grazing incidence spectrometer. The slit, grating and detector all lie on the arc of the grating's 2 2 m circle of curvature The detector is translatable along the Rowland circle while the entrance slit position remains fixed A slit width of 20 μm was used to ensure sufficient XUV radiation from the plasma reached the detector and because resolution was not an important criterion The Rowland circle setting for the detector was 16" (measured from the center of the grating) which, for this system, corresponds to a centre wavelength of 135 eV with an energy window of width 40 eV The concave grating was ruled with 1200 grooves mm^{-1} To correct for astigmatism of the spectral image and to improve the efficiency (or speed) of the grazing incidence spectrometer, this system incorporates a toroidal mirror which produces a stigmatic[2] image on the Rowland circle The toroidal mirror improves the speed by efficiently coupling light into the spectrometer by focussing it onto the entrance slit The parameters of the toroidal mirror are also chosen to fill the optimum width of the grating and therefore optimise the spectral resolution of the instrument

The photoelectric detector, illustrated in figure 2 25 comprises a photocathode (which converts the XUV photons to photoelectrons) coated onto a microchannel plate (MCP) intensifier[3] which amplifies and transmits the electrons through the MCP while maintaining the structure of the image impinging on the detector These newly generated electrons are further accelerated across a 400 μm micron-wide gap onto a phosphor which converts the electron flux to visible photons, which subsequently irradiate a photodiode array (PDA) The PDA consists of a linear array of 1024 silicon p-n junction photodiodes with 25 μm-wide centres

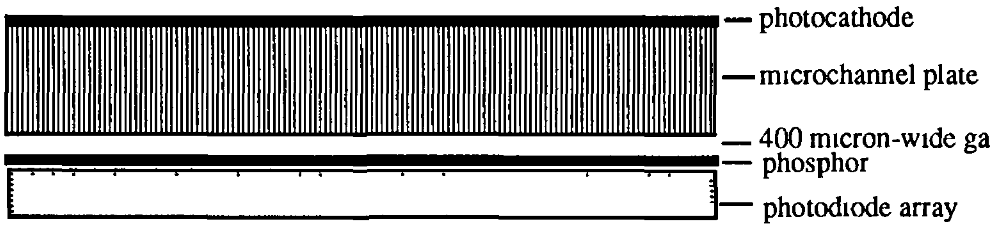

Figure 2 25 Schematic diagram of the 2 2 m photoelectric detector

The 2 2 m system shown in figure 2 26 is controlled by a software package [94] operated from a Tandon 286 which is interfaced via a GPIB to an EG&G Princeton Applied Research Optical Multichannel Analyser (OMA), model 1461 This device, programmed from the keyboard, acts as the interface between the PC and all

---

[2] A point in the object plane (of the source) will be imaged as a point in the image plane (on the detector)

[3] An MCP is an array of 10^4 – 10^7 miniature electron multipliers oriented parallel to each other, with each channel consisting of a hollow glass fibre which is internally coated in such a way as to render it semiconducting An electron which enters a channel is accelerated by a voltage through the fibre producing many more electrons through collisions with the semiconductive layer [93]

other connected devices

The MCP was operated at a working voltage of 835 V and the accelerating gap operated at a voltage of 4.5 kV The grating and detector chambers were maintained at a pressure of 2×10^{-7} mbar and the toroidal mirror chamber at a working pressure of

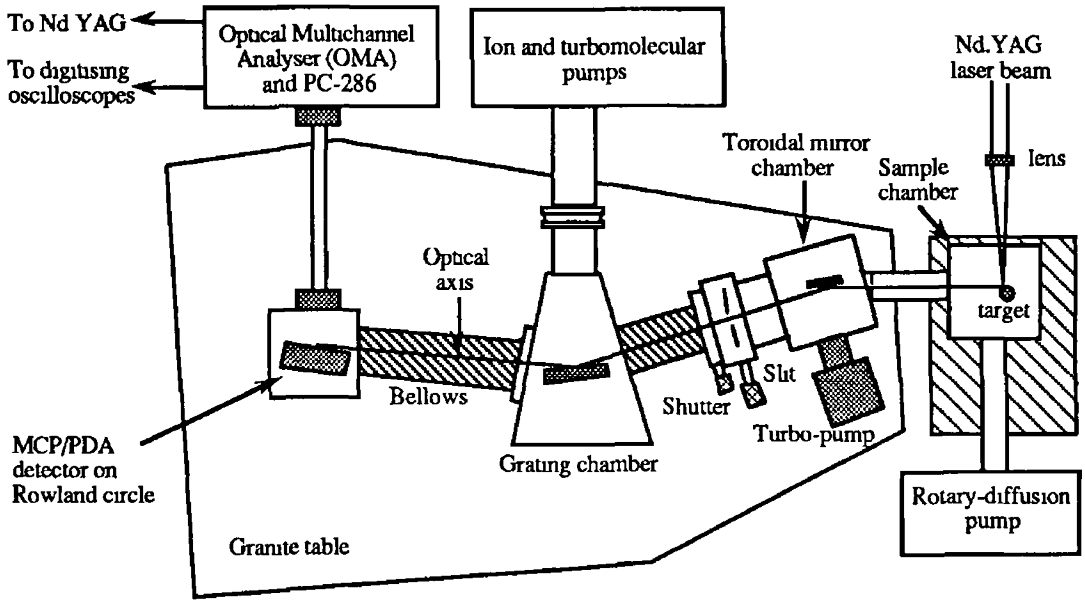

Figure 2.26 Schematic of 2.2m MacPherson spectrometer with controlling hardware

1.5×10^{-5} mbar The sample chamber (operating at a pressure of 1×10^{-5} mbar) can be returned to atmospheric pressure without affecting the rest of the system by inclusion of a GCA differential pressure barrier (an MCP with no semiconducting material on the inner walls of its channels) between the sample and toroidal mirror chambers Plasmas are positionally optimised using a rotatable-translatable shaft to which the samples are fixed Spectra were averaged over 20 shots to improve the signal-to-noise ratio Again, a reference spectrum of aluminium was recorded to calibrate the pixel axis in terms of energy (eV) Strong emission lines of alumimium are plotted as a function of pixel number and the data fitted to a 2nd order polynomial or alternatively to the grating's dispersion relation The 1024 data points in each spectrum were applied to this curve fit to convert pixel numbers into energy values

2.6 Comparison of LSM and OMA Systems

Let B_λ be the radiance or intensity per unit surface area of the plasma source at a particular wavelength λ in units in terms of flux cm^{-2} sr^{-1} or W cm^{-2} sr^{-1} in the direction of a detector The geometric etendue, G, characterises the ability of an optical system to accept light It is a function of the area of the emitting source S and the solid angle Ω into which it propagates This may be written as

$$d^2G = dSd\Omega \text{ or } G = \iint dSd\Omega$$

For a spectrometer G depends on the geometric characteristics of the system such as the slit widths and heights, dimensions of aperture and field stops, grating size, magnification and so forth, and is thus a constant of the instrument.

For the LSM system used here, the usable photon flux at the instrument exit, or throughput, for a particular wavelength is given by

$$\Phi_\lambda^{LSM} = B_\lambda \times G^{LSM} \times E_\lambda^{LSM} \times F_\lambda^{LSM} \times T_\lambda \qquad (35)$$

where E_λ^{LSM} is the efficiency of the LSM, F_λ^{LSM} is the geometric transmission and T_λ is the carbon/silver thin-film composite. The efficiency of the LSM at a particular wavelength is the integrated reflection curve of the LSM at that wavelength which is a measure of the energy in to the energy out. It depends mostly on the optical constants (see Appendix A) of the layer materials. The geometric transmission is probably a constant for the LSM in this case, but is not always so as one would normally have to include aberrations which are wavelength dependent.

The total flux measured by the PMT in a bandpass $\Delta\lambda$ is therefore

$$\Phi_{\Delta\lambda}^{LSM} = G^{LSM} F_\lambda^{LSM} \int_{\Delta\lambda} B_\lambda E_\lambda T_\lambda d\lambda \qquad (36)$$

As has been demonstrated in section 2.1.2, the LSM efficiency is not constant across the instrument bandpass and therefore must remain within the integral.

The flux measured by the OMA system at a particular wavelength is

$$\Phi_\lambda^{OMA} = B_\lambda \times G^{OMA} \times E_\lambda^{OMA} \times F_\lambda^{OMA} \qquad (37)$$

where all factors have identical meaning except E_λ^{OMA} is the efficiency of the grating. Literature [12] shows that this efficiency is probably constant over the 6 eV centred at 125.4 eV. In the spectral interval $\Delta\lambda$, one finds that

$$\Phi_{\Delta\lambda}^{OMA} = G^{OMA} F_\lambda^{OMA} E_\lambda \int_{\Delta\lambda} B_\lambda d\lambda \qquad (38)$$

Upon taking the ratio of the fluxes, one gets

$$\Phi_{\Delta\lambda}^{LSM}/\Phi_{\Delta\lambda}^{OMA} = \frac{G^{LSM} F_\lambda^{LSM} \int_{\Delta\lambda} B_\lambda E_\lambda T_\lambda d\lambda}{G^{OMA} F_\lambda^{OMA} E_\lambda^{OMA} \int_{\Delta\lambda} B_\lambda d\lambda} \qquad (39)$$

Due to the presence of the LSM efficiency curve and the system's geometric transmission, the two measured fluxes are not proportional. In order to create proportionality, one must multiply the OMA spectra by E_λ^{LSM} and F_λ^{LSM} before integration. Then the ratio becomes

$$\Phi_{\Delta\lambda}{}^{LSM} = C_1/C_2 \times \Phi'_{\Delta\lambda}{}^{OMA} \tag{40}$$

where the constant factor of the LSM and OMA systems have been substituted with C_1 and C_2 respectively Now,

$$\Phi'_{\Delta\lambda}{}^{OMA} \propto \int_{\Delta\lambda} B_\lambda E_\lambda T_\lambda d\lambda \tag{41}$$

and the two measured fluxes become directly proportional

Concluding Remarks

In this chapter, three different experimental systems have been discussed in varied detail, with the most attention to detail being paid to the XUV flux measurement system upon which the main experiments were conducted This system is capable of isolating a band of XUV radiation of width 6 03 eV, centred at 125 4 eV, by combining a NiCr/C multilayer and C/Ag thin-film composite with a collimating series of apertures The 2 2 m McPherson spectrometer, on which the emission spectra of the metal plasmas were recorded, was briefly described It was shown that the XUV integrated intensities measured on the LSM and OMA systems are proportional if the OMA spectra are modulated by the efficiency of the LSM and the transmission of the composite filter in the 6 03 eV bandpass of the LSM system The 2 m grazing incidence photographic spectrometer, upon which the XUV emission from highly ionised first row transition metals were recorded, was also briefly detailed

Chapter 3

Characterisation of Nd:YAG-Produced Plasmas

The XUV emission spectra of aluminium and the transition metal plasmas of cobalt, nickel, copper and zinc, generated by a Nd YAG laser system were recorded on a 2 m grazing incidence vacuum spectrograph The purpose of this exercise was to identify the predominant ion stages present in these plasmas and to obtain an estimate of the typical electron temperatures produced by such a laser system Arising from this work, a number of previously unidentified spectral lines of Co, Ni, Cu and Zn ions have been classified

3.1 Philosophy

As the Nd YAG laser used during the course of this work was new to our laboratory, and hence no data on the paramaters of the typical plasmas which it could generate was available, we first recorded the XUV spectra of a number of plasmas for which the atomic data was readily available To this end, the XUV emission spectrum of the well-known aluminium was recorded along with the higher-Z, first transition series metals of Co, Ni, Cu and Zn Determination of dominant ion stages and electron temperatures is most easily done for aluminium since a wealth of atomic structure data for all aluminium ion stages already exists By *visual* comparison of recorded line intensities with intensities listed in Kelly's spectral data tables [95], one can infer the ion stages present and, also, the predominant ion stages Using the ionisation model of Colombant and Tonon [20] one can then estimate the dominant ion stages present in these plasmas to check for consistency in the diagnostics

Secondly, it was hoped that by examining the known atomic structure data of the higher atomic-number elements of Co through Zn that complementary data on the typical electron temperatures and dominant ion stages of the Nd YAG-produced laser-plasmas would be obtained In compiling lists of classified transition lines for the Co through Zn ions, it was observed that some gaps in our knowledge of these atomic structures exist This, however, is not the case for the first row transition metals from Ti through Fe In order to partially fill in these gaps, an attempt at classification of previously unidentified lines was undertaken with the aid of the Hartree-Fock Configuration Interaction (HFCI) computer code written by Cowan [96]

The Nd YAG laser used to generate the plasmas was focussed with a f/5, 100 mm focal length lens to focal spot size of about 100 μm in diameter (cf section 2 1 1 of chapter 2) This corresponds to an energy density of ~5 × 10^{11} W cm^{-2} A schematic diagram of the spectrograph is given in figure 2 20 of chapter 2 along with a short description of the experimental conditions

3.2 Aluminium Spectral Lines

In Table III.1 (see further on), a list of the aluminium reference lines measured from the photographic plates, and identified using Kelly's tables, is given, along with the ionisation stage associated with each spectrum line. Although hundreds of emission lines were recorded on each plate for aluminium, it was only required that a number of easily identifiable lines be located. As can be seen from the table below, lines from ionisation stages ranging from Al VII to Al XI were present. The relative intensities of lines are our visual estimates of their brightness on the photographic plates.

3.2.1 Plasma Diagnostics of Aluminium Spectrum

On observation of the aluminium spectrum, it was noticed that the ion stages recorded ranged from Al VII up to a cut-off (as opposed to peak) ion stage of Al XI. It is intuitively difficult to precisely say which ion stages dominate the spectrum owing to the fact that spectral lines from a particular ion stage which appear to be intense may not originate from the dominant ion stage. It may also be the case that line emissions from the dominant ion stages are relatively weak and thus difficult to analyse. From the distribution of the lines though, the spectrum appears to be dominated by ionisation stages Al VIII and IX. Using equation (22) from section 1.3.4 of chapter 1, in the form

$$T_e(eV) = (1.5z)^3Z^{-1} \qquad (42)$$

allows the corresponding electron temperatures to be estimated. T_e ranged from 89 eV up to 133 eV. If one takes the mean of this energy range as being ~111 eV then the incident laser power may be calculated using the equation (21) in the form

$$\phi(Wcm^{-2}) \approx \lambda(\mu m)^{-2} \times [T_e(eV)/5.2\times10^{-6}(Z^{1/5})]^{5/3} \qquad (43)$$

which yields an estimated focussed laser power density of ~6 × 10^{11} W cm^{-2} for radiation of 1.064 μm and with Z = 13. This value is consistent with the power density calculated in section 2.1.1 of chapter 2, that is, ~5 × 10^{11} W cm^{-2}. Using the geometrically calculated intensity of 5 × 10^{11} W cm^{-2}, one can estimate the electron temperature to be approximately 100 eV which corresponds to a dominant ionisation stage of Al VIII. Again, there is some degree of consistency between the predicted and inferred dominant ion stages. Again, it is worth noting that the ionisation model applies better to heavy elements than light ones.

Table III 1 The emission lines of highly ionised aluminium identified on the photographic plates along with the ionisation stages to which these transitions correspond Relative Intensities are our visual estimations of the spectral line brightness on the photographic plates

Ion Stage	Configurations	Terms	J–J	Reference Wavelength (Å)	Relative Intensity
VII	$2s^22p^4 - 2s^22p^33d$	$^4P - ^4D$	5/2 - 7/2	83 883	500
VII	$2s^22p^3 - 2s^22p^23d$	$^2P - ^2D$	1/2 - 3/2	79 96	400
VII	$2s^22p^3 - 2s^22p^23d$	$^2P - ^2D$	5/2 - 7/2	76 557	200
VII	$2s^22p^3 - 2s^22p^23d$	$^4P - ^4P$	1/2 - 3/2	76 44	200
VIII	$2s2p^3 - 2s2p^23d$	$^3P - ^3D$	2 - 3	73 703	150
VIII	$2s2p^3 - 2s2p^23d$	$^3D - ^3F$	3 - 3	72 223	200
VIII	$2s2p^3 - 2s2p^23d$	$^3D - ^3F$	1 - 2	73 401	150
VIII	$2s^22p^2 - 2s^22p3d$	$^1D - ^1F$	2 - 3	68 375	750
VIII	$2s2p^3 - 2s2p^23d$	$^3D - ^3F$	3 - 4	67 946	500
IX	$2s2p^2 - 2s2p3d$	$^2D - ^2D$	5/2 - 5/2	64 885	150
IX	$2s2p^2 - 2s2p3d$	$^2D - ^2F$	5/2 - 7/2	63 509	500
IX	$2s2p^2 - 2s2p3d$	$^2P - ^2D$	3/2 - 5/2	63 025	500
IX	$2s2p^2 - 2s2p3d$	$^2D - ^2F$	5/2 - 7/2	59 761	300
X	$2s2p - 2s3d$	$^1P - ^1D$	1 - 2	59 107	400
X	$2s^22p^2 - 2s^22p3d$	$^1D - ^1F$	2 - 3	57 368	450
X	$2s2p - 2s3d$	$^3P - ^3D$	2 - 3	55 376	600
X	$2s2p - 2s3d$	$^3P - ^3D$	1 - 2	55 272	450
XI	$1s^22p - 1s^23d$	$^2P - ^2D$	3/2 - 5/2	52 446	800
XI	$1s^22p - 1s^23d$	$^2P - ^2D$	1/2 - 3/2	52 299	600
X	$2s^2 - 2s3p$	$^1S - ^1P$	0 - 1	51 979	350
XI	$1s^22s - 1s^23p$	$^2S - ^2P$	1/2 - 1/2	48 338	850
IX	$2s^22p - 2s^24d$	$^2P - ^2D$	3/2 - 5/2	47 856	50
X	$2p^2 - 2p4d$	$^1S - ^1P$	0 - 1	46 223	100
X	$2s2p - 2s4d$	$^1P - ^1D$	1 - 2	44 902	100
X	$2p^2 - 2p4d$	$^3P - ^3D$	2 - 3	43 577	150
XI	$1s^22p - 1s^24d$	$^2P - ^2D$	3/2 - 5/2	39 180	400
XI	$1s^22s - 1s^24p$	$^2S - ^2P$	1/2 - 3/2	36.675	350

3.3 Electron Temperatures and Predominant Ion Stages of Transition Metal Plasmas

The cobalt spectrum originates from line emissions from stages Co XI up to the observed cut-off ion stage of Co XVII. The predominant stages present on the plates appear to be Co XI and XIII. For Ni and Cu, the ion stage distribution appears to be similar. For Zn the dominant ion stages have increased by one up to Zn XII and XIV. Table III.2 shows the electron temperatures, T_e(eV), calculated from equation (21) using $\phi = 6 \times 10^{11}$ W cm^{-2} and the dominant ion stage, Y_{dom}, estimated from expression (22). The range of predominant ion stages observed on the plates, $Y_{predom}{}^{plate}$, are used to calculate the probable electron temperature range $T_e{}^{plate}$(eV).

Table III.2 Compilation of the dominant ion stages estimated from the laser power density and its corresponding electron temperatures along with the observed dominant ion stages from the photographic plates and their corresponding electron temperatures.

Metal	T_e(eV)	Y_{dom}	$Y_{preom}{}^{plate}$	$T_e{}^{plate}$(eV)
Cobalt	126	XI	XI - XIII	125 - 216
Nickel	127	XI	XI - XIII	120 - 208
Copper	128	XI	XI - XIII	116 - 201
Zinc	129	XII	XII - XIV	150 - 247

The dominant ion stages predicted from the laser power density and those inferred from the plates are in reasonable agreement. The electron temperatures differ somewhat from each other especially in the case of zinc. This is due to the fact that in estimating T_e from expression (42), the shift from one dominant ion stage to another causes an abrupt increase in the resulting T_e due to the z^3 dependence. As one increases the atomic-number of the target by one, and creates the same experimental conditions, a similar dominant ion stage may exist, producing a lower predicted T_e. Equation (43) is independent of the ion stage and allows calculation of T_e on the basis of knowing the laser focussing conditions and the atomic-number of the target. Therefore, changing the target through the transition metal series gradually increases the electron temperature by a factor of $Z^{1/5}$.

3.3 Atomic Structure Calculations

The computer code used to calculate line wavelengths and oscillator strengths was the HFCI code developed by Cowan [96] The Hartree-Fock (HF) method is a formulation of the self-consistent field method, taking into account exchange interaction In the HF method, it is assumed, in accordance with the independent particle approximation and the Pauli exclusion principle, that the N-electron wavefunction is a Slater determinant Φ, or, in other words, an antisymmetrised product of individual electron spin orbitals The optimum Slater determinant is then obtained by using the variational method to determine the 'best' individual electron spin orbitals The HF method is therefore a particular case of the variational method, in which the trial function for the N-electron atom is a Slater determinant whose individual spin orbitals are optimised

The total wavefunction Ψ of a many-electron system is the solution of Schrodinger's equation, $H\Psi = E\Psi$, where H is the Hamaltonian and E is the total energy of the system The solutions of this equation describe the states of the system, and since they also are eigenfunctions of the total angular momentum L and the total angular spin S, they are designated by a label such as γLS where γ represents a configuration The radial factors of the spin orbitals (wavefunctions for a single electron in a central potential are called *orbitals* or *spin orbitals*) are functions $R(nl,r) = (1/r)P(nl,r)$ where $P(nl,r)$ is referred to as the radial wavefunction For a given potential the bound-state orbitals form an orthonormal set with $< nl \mid n'l > = 0$ for $n \neq n'$ Let $(nl) = (n_il_i, i = 1, 2, \ , N)$ define a configuration for the atom with N-electrons A *configuration state function* (csf) is an antisymmetrized sum of the products of the orthonormal spin orbitals, one for each electron in the configuration, so as to be an eigenfunction of LS Let (l) represent the set of one electron angular quantum number and α any other information such as the coupling scheme required to uniquely specify the spin-angular coupling Then the configuration state function $\Phi((nl)\alpha LS)$ may be defined in Racah notation as

$$\Phi((nl)\alpha LS) = \mathcal{A}\ \{[\textstyle\prod_i R(n_il_i,r)] \mid (l)\alpha LS>\} \qquad (44)$$

In the Hartree-Fock approximation, $\Psi(\gamma LS) \approx \Phi(\gamma LS)$ with the radial functions selected by the energy functional, $<\Phi \mid H \mid \Phi>/<\Phi \mid \Phi>$ This must be stationary with respect to all allowed variations in the radial wavefunction It leads to a system of coupled integro-differential equations The HF method fails to produce term-splitting that agrees with experiment because it ignores the effects of interaction between configurations Configuration interaction will take place between configurations if (i) they have the same total angular momentum quantum number, J, and (ii) have the same parity P If these conditions are satisfied then CI may strongly perturb energy levels and oscillator strengths of interacting configurations

Cowan's code is a set of FORTRAN 77 programs used for the self-consistent field calculation of atomic radial wavefunctions, and of the various radial integrals involved in the calculation of the atomic energy levels and spectra The code has two input files, RCN and RCN2 The primary input information to the program RCN is the ground and excited state configurations of an ion The program calculates single-configuration radial wavefunctions $P_{n,l}(r)$ for a spherically symmetrised atom (centre-of-gravity energy of the configuration) using true Hartree-Fock calculations In addition to the radial wavefunctions, the various radial integrals, and the total energy of the atom, E_{av}, are also calculated RCN2 accepts radial wavefunctions from RCN and calculates various multiple-configuration radial integrals (such as overlap, configuration interaction, spin-orbit, radial electric dipole and electric-quadrupole integrals) It automatically computes all quantities required for calculating energy levels and spectra of an atom and writes a file containing this information for input to program RCG which performs these calculations The programs RCN35 were then submitted to BATCH on the VAX/VMS network for execution The output file RCG OUT contains, among other things, information on the atomic transitions from the ground state terms to the allowed excited state terms of interest, such as the wavelengths and oscillator strengths, determined by the selection rules for electric dipole (E_1) transitions

The above *ab initio* calculations were complemented by extrapolation of known atomic data along isoelectronic sequences, beginning with titanium where possible Measured wavelengths from Kelly's tables were fitted to a 3rd or 4th order polynomial and extended along the first row transition metal series to predict the wavelengths of unknown lines

3.1.2 The $3s^2 3p^1$ -> $3s^2 4s^1$ Transition Array

It was noted from the spectral data tables of Kelly, and Sugar and Corliss [97] that the $^2P_{1/2,3/2} - {}^2S_{1/2}$ doublet lines have not been previously identified The plot in figure 3 1 shows an extrapolation along the aluminium I isoelectronic sequence for the $^2P_{1/2,3/2} - {}^2S_{1/2}$ transitions from Ti X to Zn XVIII using known lines from Kelly's tables (represented by solid diamonds and circles) These data have been fitted to a 3rd order polynomial equation The isoelectronic extrapolation proved a reliable technique in this case even though the doublet has not been identified for chromium or manganese

Configuration interaction for the unscaled calculations was retained among the excited state configurations of the following expansion of even parity

$$3s^2(3d^1 + 4s^1 + 4d^1 + 5s^1)$$

The spectral line wavelengths measured from the plates, together with calculated and extrapolated wavelengths for the $3p^1(^2P_{1/2,3/2})$ -> $4s^1(^2S_{1/2})$ are given in Table III 3

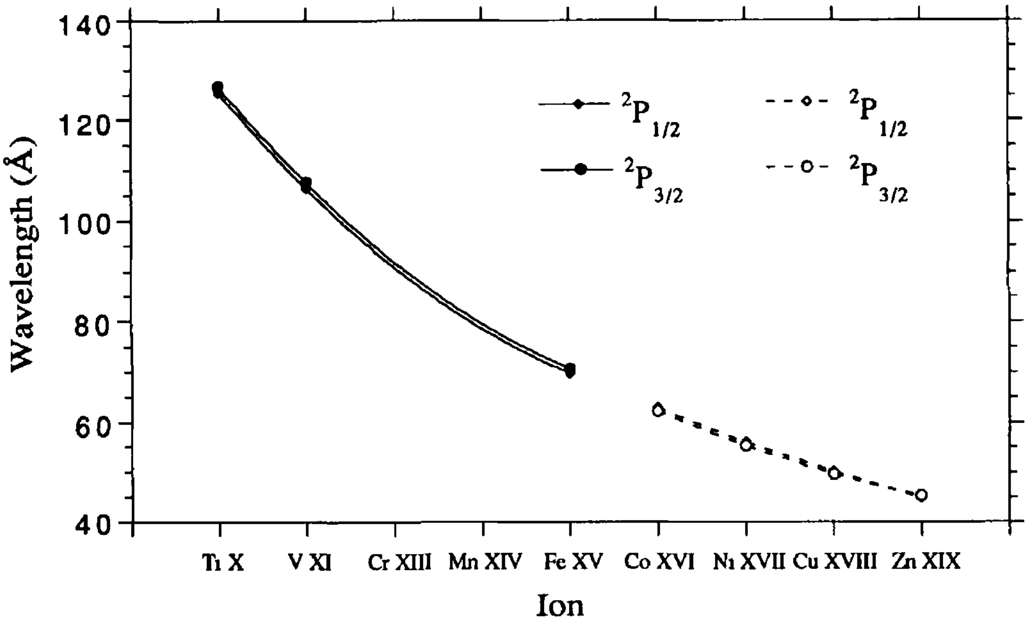

Figure 3 1 Isoelectronic extrapolation of $3s^23p^1$ ($^2P_{1/2,3/2}$) -> $3s^24s^1$ ($^2S_{1/2}$) doublet lines in Ti X, V XI and Fe XIV (extracted from Kelly's tables and represented by solid line and data points) to Co XV through to Zn XVIII (represented by dashed line and hollow data points)

The oscillator strengths for the transitions have been taken from the HFCI calculations These “transition probabilities” are listed in Table III 3 in the form of *gf*-

Table III 3 Observed, extrapolated and calculated wavelengths for the $3s^23p^1$ ($^2P_{1/2,3/2}$) -> $3s^24s^1$ ($^2S_{1/2}$) doublet of cobalt through zinc with (a) $^2P_{1/2}$ - $^2S_{1/2}$ and (b) $^2P_{3/2}$ - $^2S_{1/2}$ All wavelengths are in Angstrom units (Å)

Ion	Transition	Observed	Extrapolated	HFCI	gf_{HFCI}
Co XV	(a)	62 78	62 76	61 95	0 1437
	(b)	62 11	62 27	62 83	0 2834
Ni XVI	(a)	56 00	56 19	55 23	0 1406
	(b)	55 30	55 32	56 07	0 2769
Cu XVII	(a)	50 17	50 11	49 54	0 1378
	(b)	49 69	49 56	50 36	0 2711
Zn XVIII	(a)	44 80	44 90	44 69	0 1354
	(b)	45 19	45 27	45 49	0 2660

values The statistical weight, g, of a state is given by 2J+1 In emission, the statistical weight is derived from the upper level, i, in this case 2(1/2)+1 = 2 The intensity of a line corresponding to a particular transition from level i -> j is directly proportional to its Einstein transition probability A_{ij}

The correlation of observed with calculated wavelengths in this case is quite good This would lead one to the conclusion that the configurations selected for CI are reasonable Extrapolated wavelengths also deviated little from the observed wavelengths

3.1.3 The $3p^3$ -> $3p^2 4s^1$ Transition Array

In studying this transition array from Co XIII to Zn XVI, it became apparent that a number of previously identified lines were conflicting with the results of our calculation Using corrections to the unscaled HFCI calculations, based on the energy separation between the calculated and observed wavelengths, it was possible to evaluate the wavelength of a known line in the sulphur I isoelectronic sequence

The atomic calculations included CI between configurations of odd parity in the expansion

$$2p^6(3s^1 3p^3 3d^1 + 3s^0 3p^5 + 3s^1 3p^4 + 3s^2 3p^2 3d^1 + 3s^2 3p^2 4s^1 + 3s^2 3p^2 4d^1)$$

The calculations for transitions from the $3p^3$ ground state to excited states are slightly more complicated than for the $3p^1$ ground state due to the additional terms generated from the three p-subshell electrons The wavelength of the emission lines of interest, as predicted by the HFCI model, are continuously underestimated when compared to the observed wavelengths The emission lines listed in Table III 4 also include an intercombination or spin-forbidden transition line resulting from the breakdown of the LS-coupling where the spin conservation selection rule is disobeyed, i e , $\Delta S \neq 0$

In the case of sulphur-like Zn , it was not possible to clearly discern the lines of this transition array because they are of relatively low observed intensity This factor contributed to the drop in the number of measured lines as one continued along the isoelectronic sequence from cobalt to zinc

Based on the work undertaken here, we believe that certain lines listed in Table III 4 may have been previously misidentified The line occurring at 68 83 Å in Co XIII has been identified here as $3p^3(^4S_{3/2}) - 3p^2(^3P)4s(^4P_{5/2})$ In Kelly's tables, this line has been classified as 3p -> 4d It is believed that the 72 02 Å line has also been misidentified as $3p^3(^2D_{5/2}) - 3p^2 4d(^2F_{7/2})$ The lines occurring at 70 68 Å has been misclassified as belonging to the 3p -> 4d again The emission lines occurring at 72 56 and 70 27 Å on the plate have been tentatively attributed to the $3p^3(^2P_{3/2})$ – $3p^2(^1D)4s(^2D_{3/2})$ and $3p^3(^4S_{3/2}) - 3p^2(^3P)4s(^4P_{3/2})$ transitions, respectively, and have not been identified by any other authors to date

Table III.4 Measured and calculated wavelengths and oscillator strengths for lines in the $3p^3$ -> $3p^24s^1$ transition array for cobalt through nickel. All wavelengths are in Angstrom units (Å).

Ion	Term	J - J	Observed	HFCI	gf_{HFCI}
Co XIII	$^2P - (^1D)^2D$	3/2 - 3/2	72.56†	71.400	0.2750
	$^2D - (^3P)^2P$	3/2 - 1/2	72.02§	70.885	0.3733
	$^2D - (^3P)^2P$	5/2 - 3/2	71.84§	70.576	0.6013
	$^4S - (^3P)^4P$	3/2 - 3/2	70.27†	69.038	0.2907
	$^4D - (^1D)^2D$	5/2 - 5/2	70.68§	69.317	0.5531
	$^4S - (^3P)^4P$	3/2 - 5/2	69.83§	68.551	0.4316
Ni XIV	$^2P - (^1D)^2D$	3/2 - 3/2	64.09†	63.205	0.3063
	$^4S - (^3P)^4P$	3/2 - 5/2	61.68§	60.787	0.4210
	$^2D - (^3P)^2P$	5/2 - 3/2	63.51§	62.506	0.5802
Cu XV	$^2P - (^1D)^2D$	3/2 - 3/2	58.44†	56.279	0.4106
	$^4S - (^3P)^4P$	3/2 - 5/2	56.31§	56.494	0.0451

§ Tentatively reclassified.

† Previously unclassified.

3.1.4 The $3p^4$ -> $3p^34s^1$ Transition Array

New lines have been identified for the $3s^23p^4 - 3s^23p^34s$ transition array of cobalt through zinc during this work. Lines were selected for investigation based on the strength of their predicted *gf*-value. These lines are listed in Table III.5.

Calculations retained CI between the configurations of the expansion:

$$2p^6(3s^23p^33d^1 + 3s^03p^6 + 3s^1\,3p^5 + 3s^23p^3\,3d^1 + 3s^23p^34s^1).$$

The additional complexity of four p-electrons in the ground state increases the error in the predicted wavelengths for particular lines. Again, the HFCI model consistently overestimated the energy of the excited state levels which introduced a separation of roughly 1 Å between calculated and observed line wavelengths, but the consistency of this wavelength separation is poorer than in the previous calculations, deviating up to ~2 Å for the $^1S - ^1P$ line.

Again, due to the reduction in discernibility of certain lines in nickel through zinc, some of the lines identified in Co XIII could not be extended through the sequence The gf-value for the $^3P_0 - {}^3S_1$ line is predicted to be relatively low, but was found to be a weak feature in the cobalt spectrum, although it did not appear on any of the other plates

Table III 5 Measured and calculated wavelengths and oscillator strengths for selected lines in the $3p^4$ -> $3p^3 4s^1$ transition array for cobalt through zinc All wavelengths are in Angstrom units (Å)

Ion	Term	J - J	Observed	Extrapolated	HFCI	gf_{HFCI}
Co XII	^1S - ^1P	0 - 1	79 20	78 29	77 286	0 2462
	^3P - ^3S	0 - 1	78 85	78 72	77 724	0 0825
	^3P - ^3S	1 - 1	78 53	78 65	77 584	0 2015
	^1D - ^1D	2 - 2	78 17	76 53	76 530	0 8074
	^3P - ^3S	2 - 1	77 65	77 69	76 690	0 4611
Ni XIII	^1S - ^1P	0 - 1	69 15	68 87	67 992	0 2420
	^1D - ^1D	2 - 2	68 50	68 48	67 425	0 7705
	^3P - ^3S	2 - 1	68 30	68 35	67 473	0 4597
Cu XIV	^1S - ^1P	0 - 1	61 13	61 10	60 300	0 2381
	^1D - ^1D	2 - 2	60 50	60 83	59 875	0 7359
	^3P - ^3S	2 - 1	60 33	60 65	59 845	0 4582
Zn XV	^1D - ^1D	2 - 2	54 43	54 61	53 864	0 2346
	^1S - ^1P	0 - 1	53 95	54 45	53 547	0 7042

In figure 3 2, the deviation between the observed and calculated wavelengths for selected lines has been plotted The data points for each transition along the isoelectronic series have been fitted to a 4th order polynomial equation The wavelengths calculated for transitions by Cowan's code improve in accuracy as the charge state increases along the isoelectronic sequence This is due to the increased core charge, and hence, Coulomb potential, experienced by the electrons, which increases their binding energy The increased Coulomb interaction term dominates in the atomic calculations over the perturbing configuration interaction term, and thus, the system becomes more hydrogenic

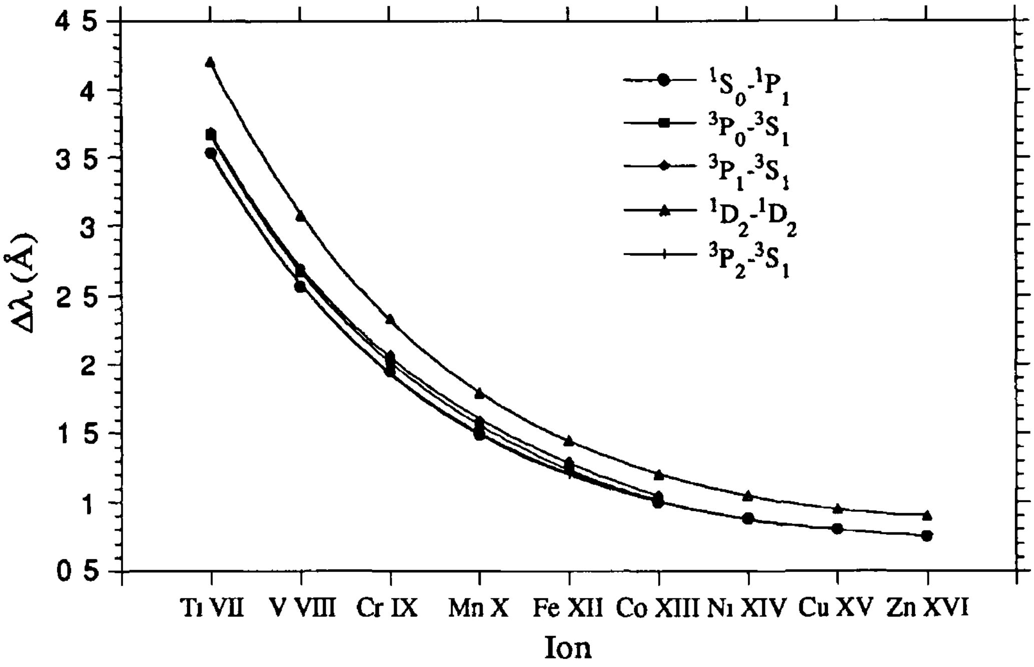

Figure 3 2 The separation between the observed and calculated wavelengths for transitions in the $3p^4$ -> $3p^3 4s^1$ transition array for ions of Ti VII to Zn XV isoelectronic with S I

Concluding Remarks

The photographically recorded spectra of the highly ionised aluminium and the transition metals of cobalt through zinc have been analysed The laser power density for the Nd YAG laser was estimated at 6 × 10^{11} W cm^{-2} based on the ion stages observed in the aluminium spectrum for an estimated electron temperature of 111 eV Plasma electron temperatures of the order of 130 eV were found to exist in the transition metal spectra which correspond to dominant ion stages of Co XI, Ni XI, Cu XI and Zn XII New lines for the Co XII, XIII, XV, and isoelectronic metals in the series up to Zn, have been tentatively classified with the aid of Hartree-Fock Configuration Interaction calculations and isoelectronic extrapolations for the $3p^n$ -> $3p^{n-1}4s^1$ transition arrays where n = 1, 3, 4

Chapter 4

Atomic-Number Dependence

In this chapter, results are presented on a study of the atomic-number dependence of XUV emission from Nd YAG-generated plasmas on metals from carbon through lead In order to aid interpretation of the Z-dependence of the XUV flux emission observed, reference is made to the ionisation balance and gross atomic structure of ions present in our plasmas To this end, spectrally-resolved spectra recorded on the 2 2 m grazing incidence spectrometer are also presented for a selected number of targets These data are used to generate a complementary atomic-number dependence plot which is compared with the plot obtained from XUV flux measurements

4.1 Introduction

For over two decades, LPPs generated by solid state lasers have been employed with considerable success as XUV light sources The outstanding properties of the LPLS are (i) the very high instantaneous brightness in the XUV range, (ii) the possibility of producing picosecond and sub-picosecond XUV emission, and (iii) the small and reproducible source size As we have seen in chapter 1, these sources have found many useful applications in research laboratories Examples are XUV emission and absorption spectroscopy, XUV laser research, diagnostics of inertial-confinement fusion (ICF) and high-resolution x-ray microscopy and lithography Some of these applications have industrial potential The growth in importance of XUV light sources has been further stimulated by the progress in the development of XUV optical elements such as multilayer mirrors The XUV emission from laser-plasmas depends strongly on the atomic-number of the target material and the laser irradiance conditions (such as pulse duration, wavelength of radiation and focussing conditions)

Previous studies of the atomic-number dependence of radiative emission from laser-plasmas have concentrated on the x-ray spectral region (and to a lesser extent on the XUV region) using large scale laser systems McMordie and Simmons [70] studied the x-ray emission from plasmas of 26 targets ranging from Z = 6 – 92 with a CO_2 laser in the ~7 × 10^{10} W cm^{-2} energy region The plasma x-ray emission above a photon energy of $h\omega$ = 800 eV with the bandpass determined by a 20 – 80 μm thick Be foil, was recorded using two silicon p-i-n diodes Srong peaks were observed as a function of target-Z The greatest x-ray yield observed was for Ti Strong x-ray yields were also observed from plasmas of Fe, Zn, Ag, Mo, In and Cd Bleach and Nagel [71] investigated plasma x-ray emission from targets containing elements in the range $6 \leq Z \leq 68$ using a ruby laser with an on target irradiance of ~10^{12} W cm^{-2} Absolute plasma x-ray emission was measured in the 0 1 – 5 keV energy region using a silicon diode located behind a Be filter They also found that strong peaks were observed at atomic-numbers corresponding to ions with valence/sub-valence electrons in the K, L and M atomic shells between and within which electron transitions occur producing the measured radiation Gilbert *et al* [72] measured the x-ray yields of plasmas, in the 0 7 – 20 keV region, created from 36 target elements ranging from Z = 4 – 92 Targets were irradiated with 8 ns Nd glass laser pulses with a focussed power density of ~4 × 10^{13} W cm^{-2} and the emitted plasma radiation measured with crystal spectrograph and a p-i-n diode spectrometer Total x-ray irradiances as a function of target-Z showed strong peaking corresponding to transitions to the K, L and M shells Nakano and Kuroda [98] measured the x-ray intensity from plasmas, produced with a 30 ps YAG laser, above 2 keV on target metals from Z = 6 – 82 X-rays were measured using a 100 µm Be foil in front of a PMT equipped with a plastic scintillating material No distinct peaking was observed as a function of target-Z, although an oscillatory behaviour was present Gupta *et al* [73] measured the x-ray emission intensity from plasmas created with a 5 ns Nd glass laser with a focussed irradiance of ~10^{13} W cm^{2} on targets in the range 6 ≤ Z ≤ 73 The x-ray intensity measurements were carried out using a scintillator-PMT combination coupled with a thin polycarbonate foil with a low energy cut-off of 900 eV Again, it was observed that the x-ray intensity demonstrated strong dependence on target-Z, differing by over an order of magnitude for different elements The greatest flux measured was from a copper plasma followed by that of antimony Recently, Zeng *et al* [99] measured the absolute x-ray intensity from 21 elements ranging from Z = 6 – 50 in the 2 – 13 nm energy region Measurements were carried out on plasmas created by 8 ns, 500 mJ Nd YAG laser pulses (operating at the fundamental (1 06 µm) and first harmonic (0 53 µm) wavelengths) and also using a 4 J, 35 ns slab Nd glass laser for spectra recorded using a grazing incidence spectrometer equipped with a MCP-PDA detector

XUV emission from LPPs has been studied in detail by authors such as Mochizuki *et al* [74] They investigated the atomic-number dependence conversion efficiency to soft x-ray photons in the 0 1 – 1 5 keV region for 10 elements from Z = 6 – 79 Plasmas were generated with 0 53 µm light from a frequency-doubled GEKKO-IV laser system generating a power density of ~10^{14} W cm^{-2} in 1 ns Emitted plasma radiation was measured with an x-ray diode (XRD) detector array Again, an "undulatory" dependence of the x-ray flux on atomic-number was observed It is clearly seen from their study that the atomic shell mainly contributing to the measured soft x-ray radiation moved outwards, i e , from K to L to M etc , as Z increases, and from that shell, a dominant stage of ionisation and corresponding electron temperature can be inferred at the emission region Mead *et al* [75] irradiated a number of disk targets of different Z with 0 53 µm light in 3 – 30 J, 600 ps pulses from an Nd glass laser which could produce a power density in the range 3 × 10^{13} – 4

$\times 10^{14}$ W cm^{-2} Plasma studies were performed on (i) laser energy absorption rates which was observed to increase with decreasing laser intensity and increasing target-Z, (ii) hard x-ray fluence in the energy region of 5 – 70 keV which increased with laser intensity and target-Z, and x-ray conversion efficiencies to photons with $h\omega >$ 0 1 keV for titanium and gold which increase with target-Z and decrease with increasing laser intensity

To date, systematic studies of the Z-dependence of plasma emission, whether in the x-ray or XUV region, have, in the main, utilised high-power frequency-doubled lasers with only a few exceptions Such laser systems would not be considered table-top laser sources, as would be the standard in most laboratories The study presented in this thesis is the first systematic investigation of the Z-dependence of XUV flux emission from a LPP carried out with a conventional table-top laser system (0 5 J, 10 ns) operating at the fundamental wavelength (1 064 µm) Its aim is to optimise the plasma XUV emission obtained from plasma sources under the constraints of the present experimental system

To this end, we have measured the variations of the XUV photon flux emitted by laser-plasmas as a function of the atomic-number of the target material using the experimental set-up described in chapter 2 We recall that this system transmits only a ~6 eV photon energy band centred at $h\omega$ = 125 4 eV The series of measurements was carried out for 27 elements roughly spanning the Periodic Table, i e , from Z = 6 (carbon) to Z = 82 (lead) The elements used as well as their location in the Periodic Table are highlighted in figure 4 1 A constant laser power density of approximately 5 $\times 10^{11}$ W cm^{-2} was used to create the plasma in all these experiments From the measured XUV flux of each plasma, the relative integrated flux intensity (area under the measured curve) can be determined and a target-Z dependence plot generated

To facilitate interpretation of the Z-dependence measured with the LSM system, the XUV spectra of certain elements used in the XUV flux measurements were recorded using a 2 2 m grazing incidence spectrometer in the 116 – 136 eV energy region The OMA-equipped spectrometer has been previously described in section 2 5 of chapter 2 The space-resolved spectra serve to provide information on the nature of the radiation (line and/or continuum and their relative dominance) contributing to the measured XUV flux in the LSM system In the case of a limited number of spectra, it was possible to classify spectral lines from which information could be gleaned on the emitting ion species present in the plasmas

We have also seen in section 2 6 of chapter 2 that the throughput or usable photon flux of the LSM and OMA system are proportional if the spectra recorded on the OMA system are modulated by the efficiency of the LSM and the transmittance of the C/Ag composite filter in that system Thus integrating the modified OMA spectra in the 6 03 eV bandpass of the LSM system yielded a complementary Z-dependence plot with which intercomparison with the LSM data could be made

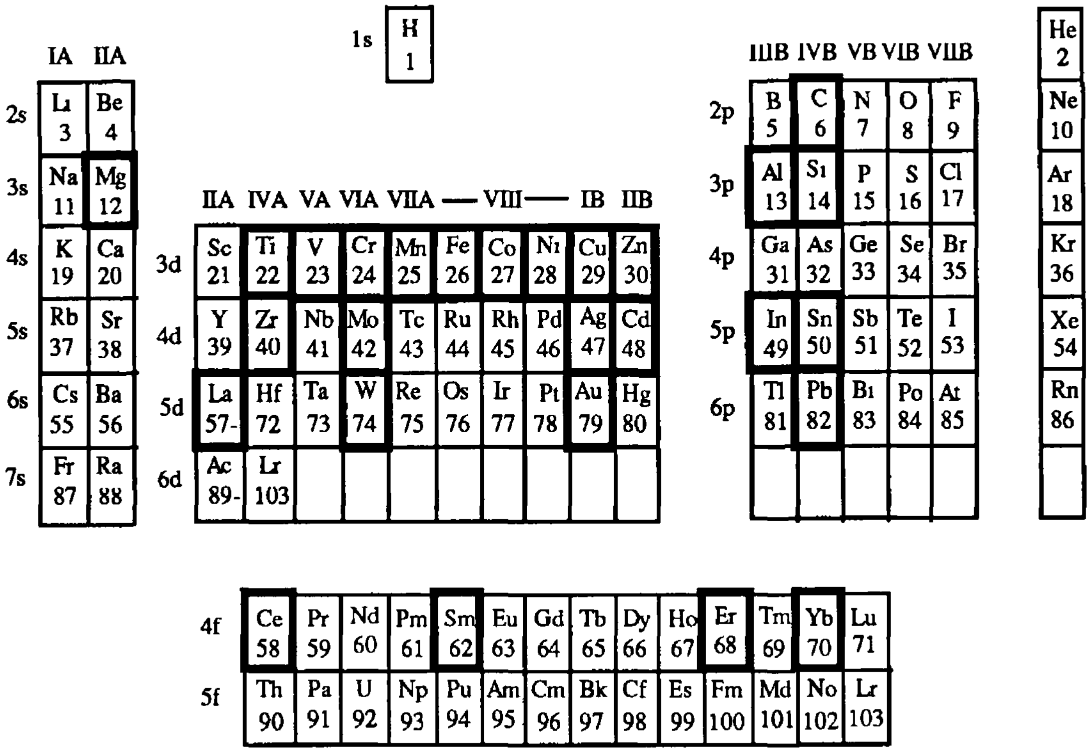

Figure 4 1 The elements of the periodic table selected for the atomic-number dependence study The metals chosen are highlighted with a dark band

4.2 Analysis of XUV Flux Measurements and Their Spectra

The XUV flux measurements for different targets and their spectrally-resolved emission spectra are presented in the following section Where possible, spectral lines are identified and ion stages contributing to the measured radiation are indicated

4.2.1 Light Metals from C – Si

Figure 4 2 shows the measured XUV flux for carbon, magnesium and aluminium As is readily seen, carbon produced only a small XUV flux signal This also proved to be the case when recording its emission spectrum with the OMA system From available spectral data [95,97], it is evident that no spectral lines have been measured for carbon in the 120 – 130 eV spectral region The "hump" appearing in figure 4 2 is produced by recombination/bremstrahlung continuum radiation

Aluminium, on the other hand, has many spectral lines in the energy region of interest as shown in figure 4 3 The emission spectrum comprises numerous discrete lines superimposed on a bremsstrahlung (free-free transition) and/or recombination (free-bound transition) continuum These spectral lines contribute dramatically to the measured flux

From Kelly's tables, it is noted that the transition arrays and the corresponding ionisation stages dominating the spectrum of magnesium in the bandpass energy region (around 122 – 129 eV) are

Mg V	[$2s^22p^4$ -> $2s^22p^3$(4d, 5s, 5d)]
Mg VI	[$2s^22p^3$ -> $2s^22p^23d$]
Mg VII	[$2s^2 2p^2$ -> $2s^2 2p$(3s, 3d)]
Mg VIII	[$2s^0 2p^3$ -> $2s 2p3d$]

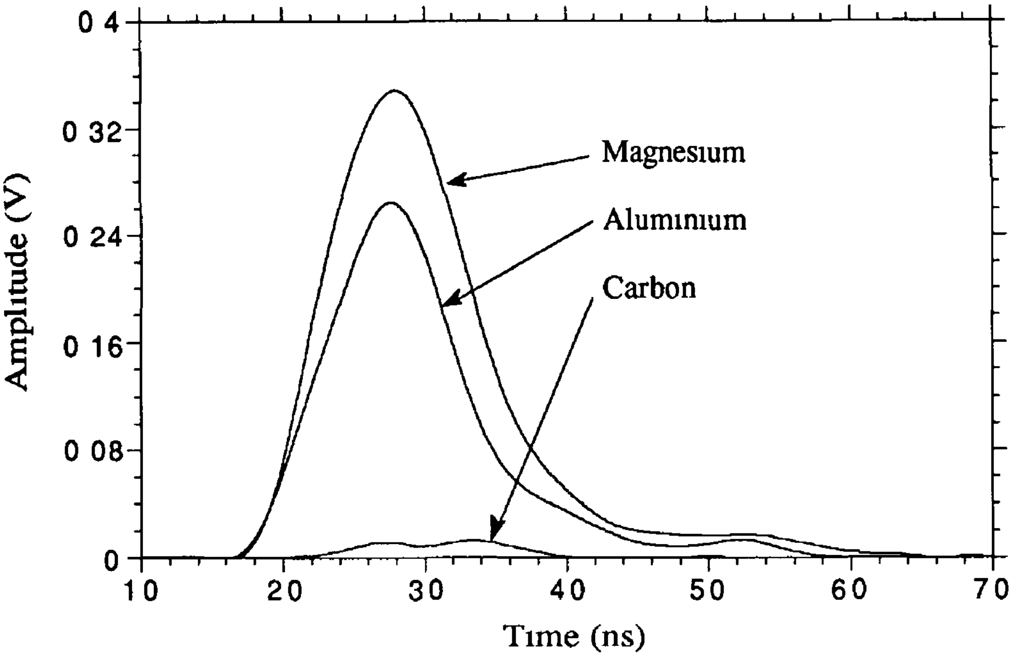

Figure 4 2 The measured XUV flux emissions from carbon, magnesium and aluminium

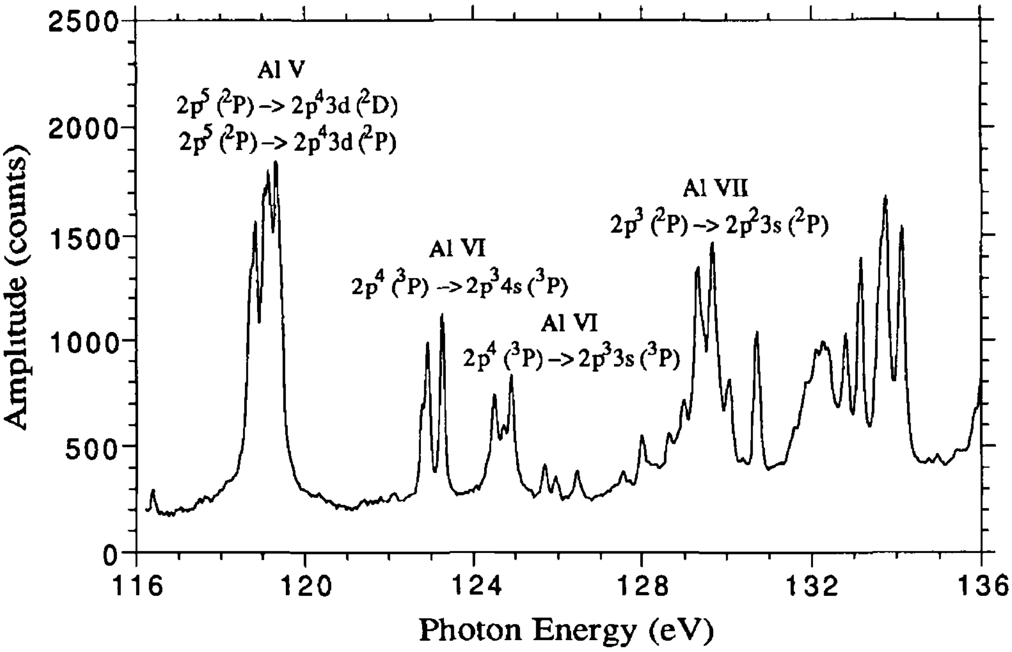

Figure 4 3 The emission spectrum of aluminium in the 116 – 136 eV region

In the case of aluminum these are

Al V	$[2s^22p^5 \to 2s^22p^43d]$
Al VI	$[2s^22p^4 \to 2s^22p^3(3d, 3s)]$
Al VII	$[2s2p^4 \to 2s2p^33s, 2p^5 \to 2s^22p^25d]$

The emission spectrum of silicon in the bandpass of the flux measurement is dominated by

Si V	$[2s^22p^6 \to 2s^22p^53d]$
Si VI	$[2s^22p^5 \to 2s^22p^43s]$

From figure 4 2, we observe that magnesium is the brightest of the low-Z metals examined From Kelly's tables one sees that many bright lines, originating from the ion stages listed above for magnesium are present (although not shown here) with relative intensities up to 500

4.2.1 3d Transition Metal Series from Ti - Zn

Laser-plasmas created from light-to-moderate atomic-number elements ($22 < Z < 30$) show numerous emission lines superimposed on a strong continuum (which originates mainly from electron-ion recombination) as shown in figures 4 4 In going from low-to-high atomic-number targets, line emission in the XUV spectral range gives way to recombination continuum with a relative strength which increases with target-Z This increase is due to (i) the higher average ion stages attained, (ii) the subsequent increase in electron density and (iii) the increase in ion densities resulting from the reduction in the mass flow rate [100] Few spectral lines have been identified for the first row transition metal series within the photon energy region of interest As seen in figure 4 4(a), the relative dominance of lines is significantly reduced as one progresses along the 3d sequence The strength of the underlying continuum of titanium is approximately 600 counts as measured with the MCP/PDA detector array The dominant transition arrays present in the titanium spectrum are assigned to the $3s^23p - 3s^2(4d, 5f, 5d)$ of Ti X and $3s3p - 3p4d$ and $3p^2 - 3p4d$ of Ti XI The corresponding XUV pulse measured with the LSM system is shown in figure 4 5 In the case of the Fe plasma shown in figure 4 4(b), these arrays are seen to move to higher energies, out of spectral energy window of interest The transition arrays expected (on the basis of known spectral lines published in Kelly's tables) to produce the strong lines appearing between 116 and 125 eV are $3s^23p^5 - 3s^23p^44s$ of Fe X and $3s^23p3d - 3s^23p4p$ of Fe XIII Also readily seen in this spectrum is the increased continuum level at about 800 counts Figure 4 5 displays the XUV pulse measured with the LSM system The spectrum of zinc in figure 4 4(c) clearly shows the continuum as the dominant feature especially in a 6 eV band centred at 125 eV The continuum level has a "valley" in this part of the spectrum reducing the counts level to below 800 at around 125 eV The XUV pulse produced by this radiation is shown in

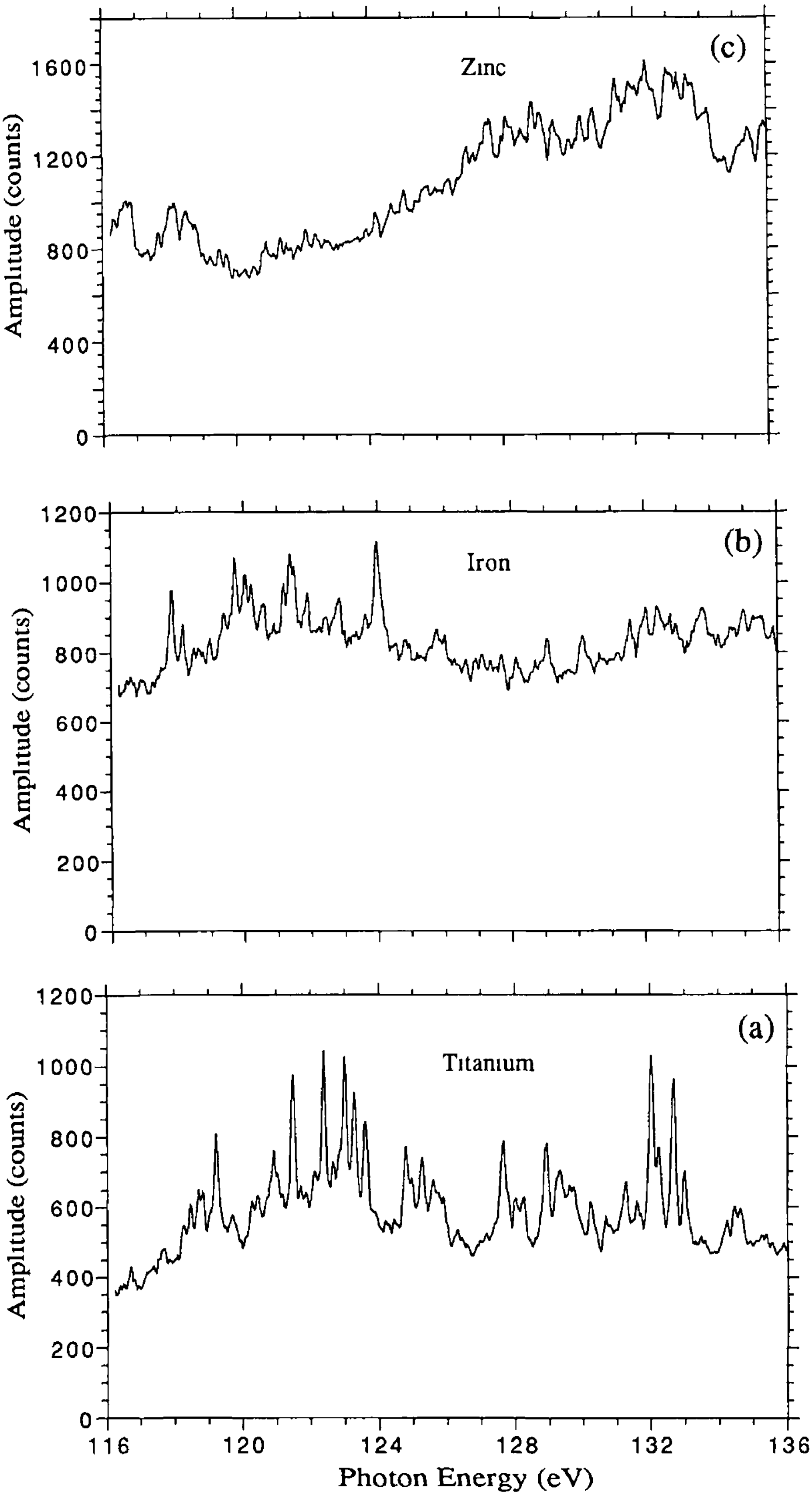

Figure 4 4 The emission spectra of titanium, iron and zinc in the 116 – 136 eV energy region figure 4 5

In summary, it is clear from figure 4 4 that the increase in the measured flux with the LSM system is mainly due to an increase in the XUV continuum emission

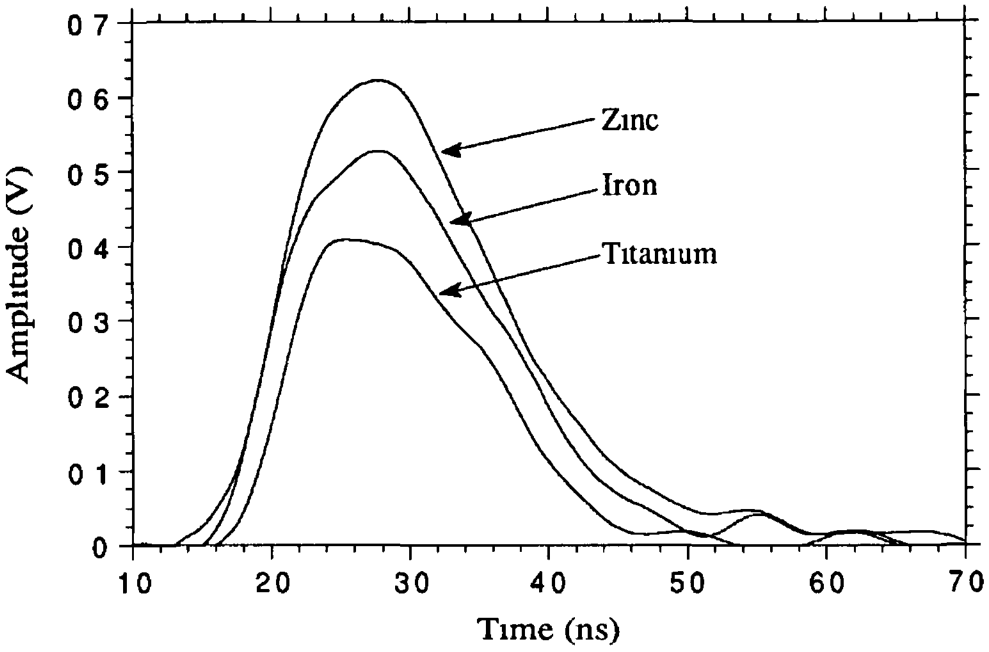

Figure 4 5 The measured XUV flux emission from plasmas of titanium, iron and zinc

4.2.3 Medium-Z Elements from Zr – Sn

As the atomic-number of the target increases, so too does the continuum emission In the case of the 4d transition elements, one finds that the recombination continuum is the dominant spectral feature Many strong lines are still present Figure 4 6 plots the measured XUV flux from plasmas of zirconium, silver and tin Tin produced the greatest flux of this selection of metals Of the 4d transition metals examined, cadmium generated the highest measured flux Examples of emission spectra of plasmas created from the 4d elements of zirconium and cadmium are shown in figures 4 7 and 4 8 respectively Zirconium produces a low-level continuum (just below 200 counts) and no strong lines in the 122 – 126 eV region thus yielding a low XUV flux measurement as shown in figure 4 6 Cadmium, on the other hand, produces a strong continuum (about 1000 counts) with many strong spectral lines in the 6 eV band centred at ~125 eV which is seen by the LSM system as a greater flux measurement The elements indium and tin produced even higher XUV fluxes than the 4d elements, with tin producing the largest

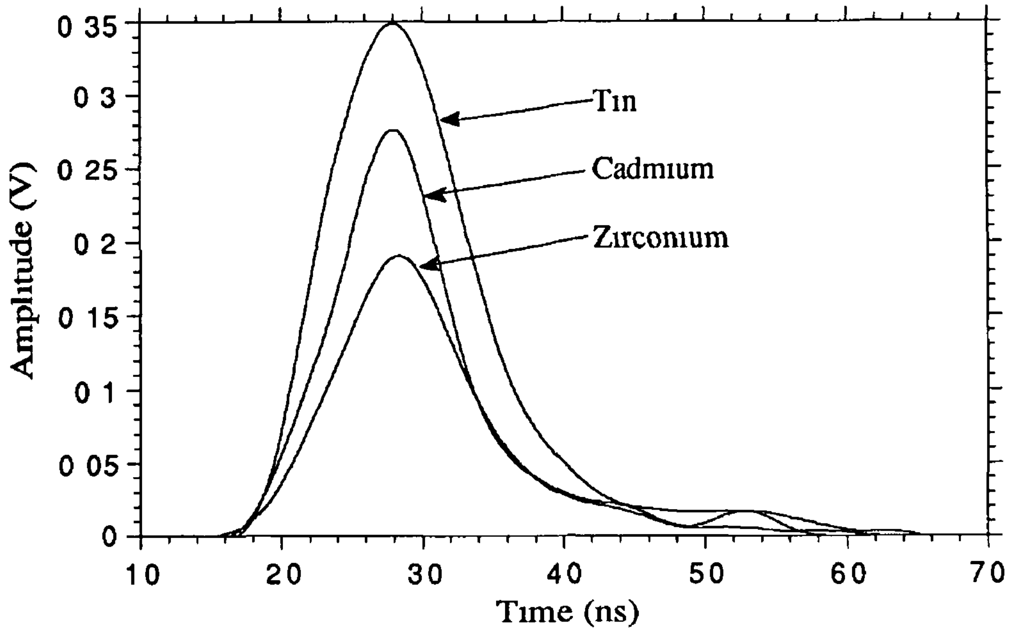

Figure 4 6 The measured XUV flux emission from plasmas of zirconium, cadmium and tin

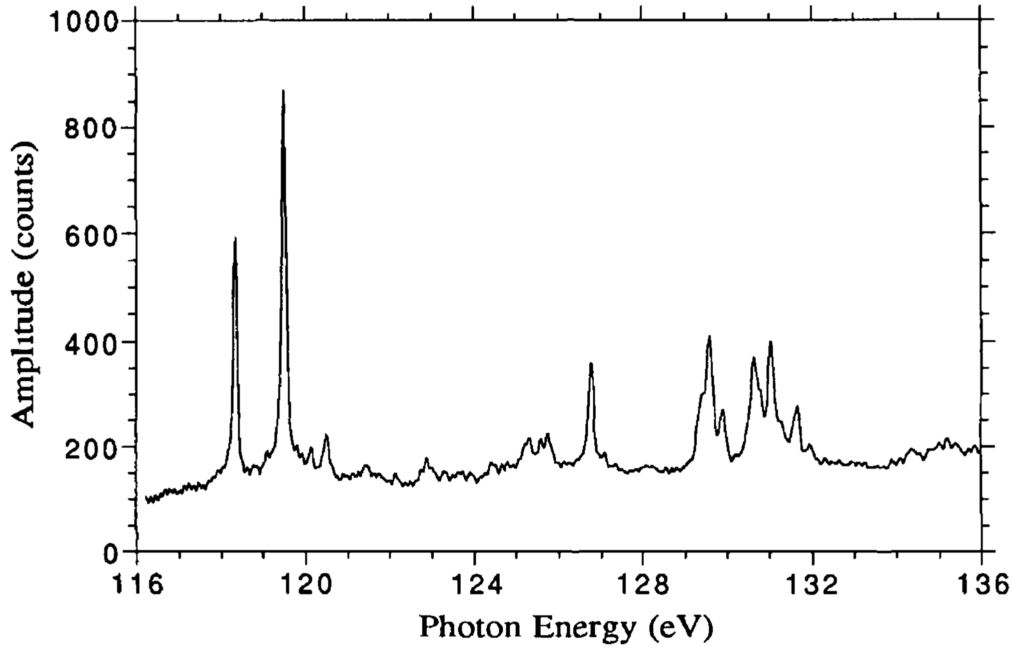

Figure 4 7 The emission spectrum of zirconium in the 116 – 136 eV energy region

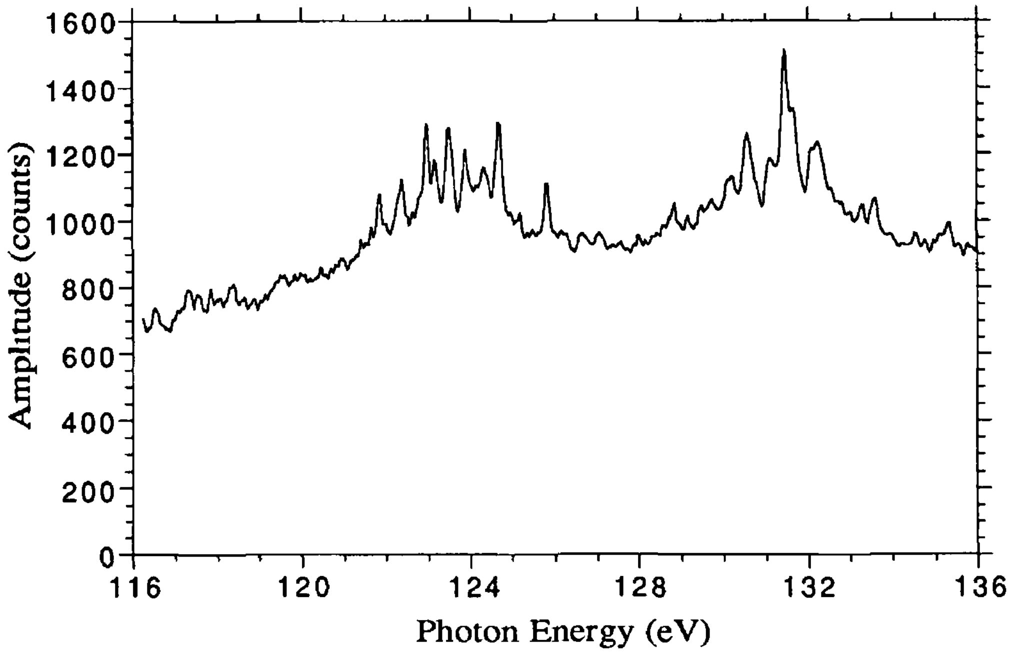

Figure 4 8 The emission spectrum of cadmium in the 116 – 136 eV energy region

4.2.4 Lanthanides and Heavy Metals from La – Pb

The emission spectra of laser-plasmas of the elements from lanthanum to tungsten have the remarkable characteristic of emitting essentially line-free continua extending from about 40 – 2000 Å with a peak intensity in the 125 eV energy region [36,37] Considering the points discussed above with reference to the increase in continuum emission with higher atomic-number, one might expect that the continuum emission should continue to grow in intensity and smoothness as the target atomic-number increases, but in the case of the lanthanides this is not exactly true The continuum-like structure of lanthanum shown in figure 4 9 may be explained in the following manner Application of the ionisation model of Colomant and Tonon [20] to rare-earth plasmas created with a laser pulse of 5×10^{11} W cm^{-2} yields an electron density of $\approx 10^{21}$ cm^{-3} at an electron temperature of about 50 eV with a corresponding predominant charge states of about 11 and a distribution extending up to 16 times ionised species [40] Under such conditions, recombination radiation will be the dominant source of XUV continuum The contribution from line radiation can be significantly absorbed by plasma opacity, i e , any line emission from the plasma's hot core will be attenuated in the cool sheath surrounding the plasma However, plasma opacity does not explain the purity of the continuum as strong line radiation is emitted from plasmas of elements above and below the rare-earth elements The striking absence of discrete features may be explained if one examines the energy level structure of the range of electron configuration existing in these plasmas

For low degrees of ionisation (z < 5), the 5s and 5p subshells are filled and the 4f varies with atomic-number and the ion stage With increasing ionisation, and hence increasing core charge, the 4f electron binding energy becomes larger than the 5s and 5p binding energies 4f/5p and 4f/5s level crossing occurs for six and twelve times ionised species, respectively [99] These elements will contain 4f electrons in the ground state for each ion generated in the laser-plasma The proximity of the 4f, 5s and 5p binding energies gives rise to bands of overlapping complex configurations with variable numbers of 4f, 5s, and 5p electrons Transitions between families of such degenerate ground and excited configurations can give rise to hundreds of thousands of lines [99] As a result, the oscillator strength for these lines are so weakened that no strong individual features appear in the emission spectrum, i e , they form unresolved transition arrays (UTAs)

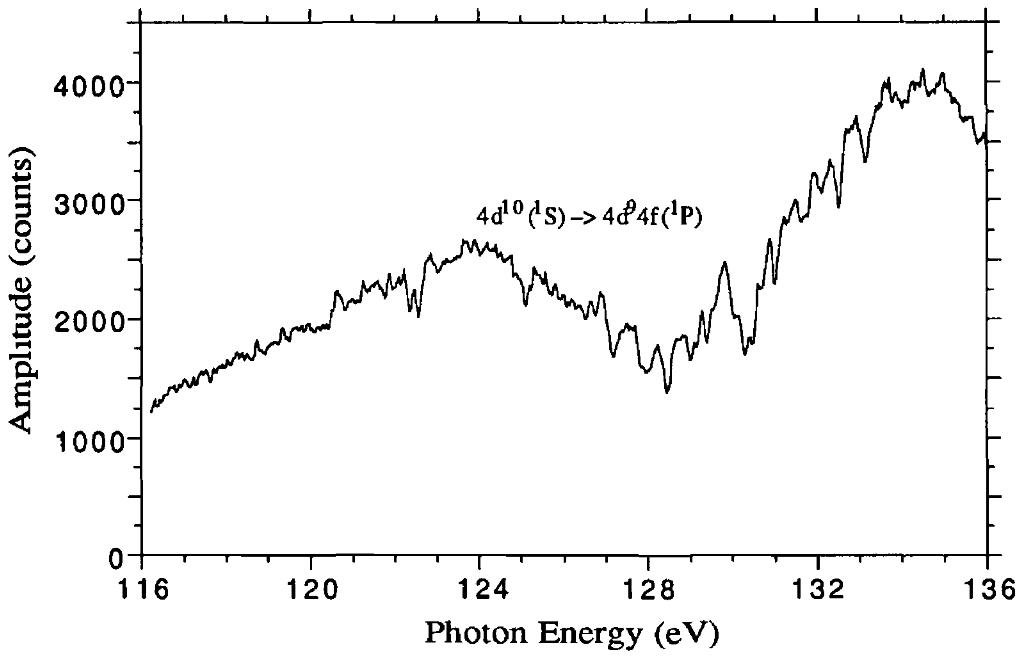

Figure 4 9 The emission spectrum of lanthanum in the 116 –136 eV energy region

In the 125 eV energy region, lanthanide UTAs originate from the $4d^n \rightarrow 4d^{n-1}4f$ transitions from ionisation stages up to XV [100] Lanthanum produced the greatest flux emission of all targets examined in the 122 4 – 128 4 eV energy region as can be seen from figure 4 10 From 103 – 170 eV, the emission spectrum of lanthanum is dominated by a strong broad emission feature, typically 30 eV wide [101] The observed UTA centred at about 125 eV has been assigned to the $4d^n$ – $4d^{n-1}4f$ transition arrays of lanthanum ions Since these features arise from transitions of 4d – 4f and have $\Delta n = 0$, the XUV emission spectra from a group of ion stages should lie approximately in the same energy region Calculations using HFCI code predicted that for the La IV [$4d^{10}$ (^1S) -> $4d^94f$ (^1P)], the average energy is 123 86 eV

Calculations also showed that for the ion stages up to La XII, the value of E_{av} (average energy of the configuration) were fairly close to the 125 eV region and therefore these UTAs will strongly overlap each other Such UTAs move monotonically to higher energies with increasing atomic-number This appears to be the case for lanthanides with Z > 57 for which the UTA in figure 4 9 is shifting out of the 6 eV window at 125 eV and thus recording a lower but still significant XUV flux

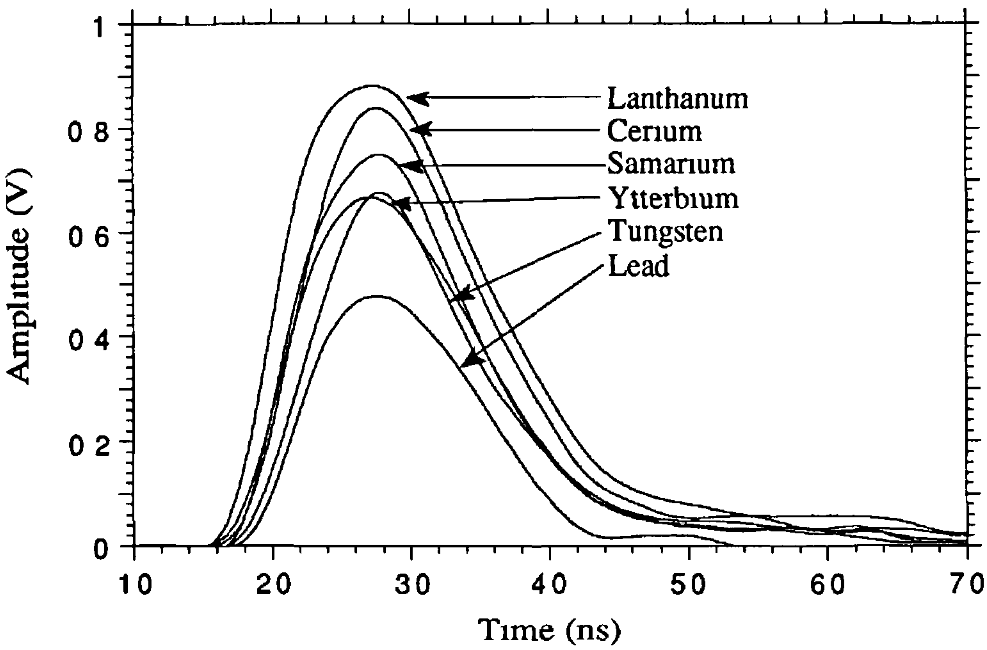

Figure 4 10 The measured XUV flux for plasmas of lanthanum, cerium, samarium, ytterium and high-Z plasmas of tungsten and lead

Plasmas from high-Z metals emit smooth and broad continuum-like structure as seen in the case of gold in figure 4 11 Tungsten and lead (whose measured XUV flux emission are shown in figure 4 10) and gold were the high-Z metals studied in this work Tungsten produced the highest measured XUV flux, and lead the lowest

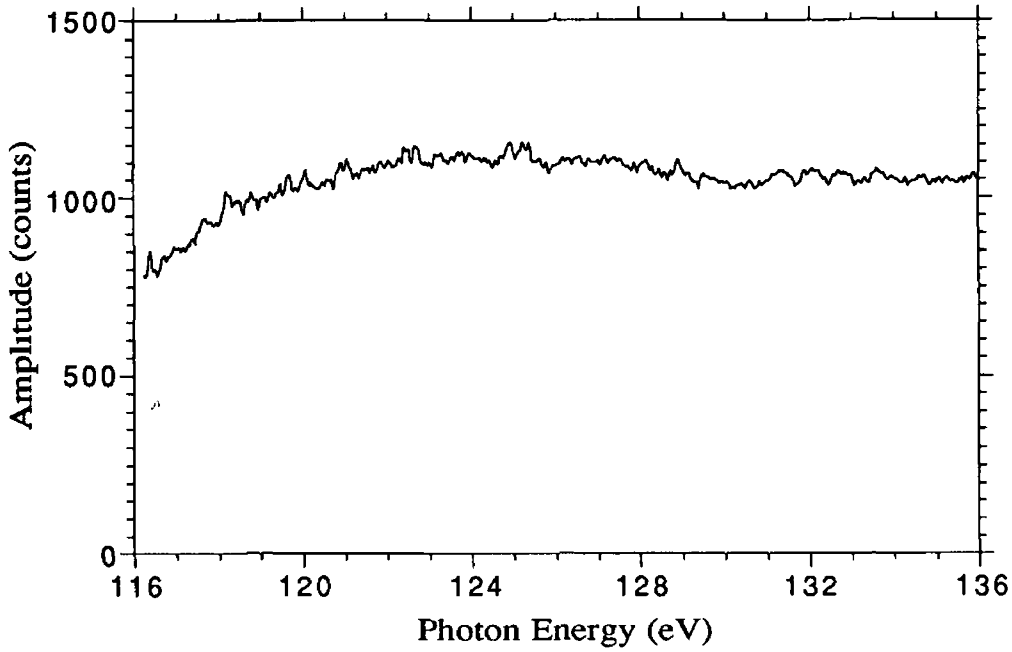

Figure 4.11 The emission spectrum of gold in the 116 – 136 eV energy region

4.3 Comparison of LSM and OMA Atomic-Number Dependence

The significant quantity measured during the present study is the integrated intensity rather than the peak amplitude of the XUV pulse. For each of the 27 elements examined here, the area under the curve gave a measure of the integrated intensity of the flux emission on a relative scale in the 122.3 – 128.5 eV spectral region as defined by the 6.03 eV bandpass of the LSM system.

Recalling section 2.6 of chapter 2, we found that the OMA spectra could be used to generate an atomic-number dependence plot which is proportional to the dependence observed for the LSM system. The ratio of the measured fluxes for the LSM and OMA systems was derived to be (see expression (39))

$$\Phi_{\Delta\lambda}^{LSM}/\Phi_{\Delta\lambda}^{OMA} = \frac{G^{LSM}\, F_{\lambda}^{LSM} \int_{\Delta\lambda} B_{\lambda} E_{\lambda} T_{\lambda}\, d\lambda}{G^{OMA}\, F_{\lambda}^{OMA}\, E_{\lambda}^{OMA} \int_{\Delta\lambda} B_{\lambda}\, d\lambda}$$

The factors outside the integrals are constant over the bandpass, $\Delta\lambda$, of the LSM system. In order to render Φ^{LSM} and Φ^{OMA} proportional, one must multiply each OMA spectrum by the efficiency of the multilayer, E_{λ}, and the transmission of the Ag/C composite thin-film filter, T_{λ}, and then integrate the modified spectra in the 6.03 eV energy bandpass of the LSM system.

Figure 4 12 plots the integrated XUV intensity in relative units as a function of the target atomic-number for both the LSM and OMA systems The LSM data are represented by circles and the OMA data by triangles Both sets of atomic-number dependence data have been normalised to lanthanum A similar chemical trend is observed for both graphs An interpolating curve is only drawn for the LSM data to guide the eye Graphs display peaks and troughs which are strongly dependent on the target-Z The peaks are labelled K, L, M corresponding to the atomic shells into which or within which atomic transitions can occur producing the measured radiation Each peak originates from radiation of the dominating species of multiply-charged ions in the plasma, and mainly correspond to a set of transitions where the change in the principle quantum number is unity, that is to say, $\Delta n = 1$ (but also for $\Delta n = 0$ and $\Delta n \geq 1$) These sets of transitions form L-spectra with $n \geq 3 \rightarrow n = 2$ (for ions stipped down to the L-shell), M-spectra for $n \geq 4 \rightarrow n = 3$, and N-spectra for $n \geq 5 \rightarrow n = 4$ and so on Also, from observation of the overall trend in figure 4 12, it is clear that recombination continuum (which scales with ion charge as z^2 [102]) is providing an increasing ramp with Z onto which line continuum provides some modulation This gross Z-dependence is quite similar to those previously observed for the x-ray energy region by McMordie *et al*, Gupta *et al* and Glibert *et al* The measured peaks for the M- and N-shells occur at Zn and La for the LSM system and at Cu and La for the OMA system The L-shell peaks at magnesium for the LSM system but no corresponding measurement exists for the OMA system In both cases, the minimum integrated intensity recorded was for carbon, and the maximum for lanthanum

Differences in the Z-dependencies measured by the LSM and OMA systems are due, in my opinion, to experimental errors For example, slight variations in the plasma production conditions due to (i) the laser irradiance conditions not be identical for each system (since different lenses were used for each), (ii) the fact that the internal plasma conditions such as dominant ionisation stages and electron temperatures are not completely controllable, and from plasma to plasma these may vary Another reason is that different parts of the plasma may have been viewed by the detector in each system due to alignment requirements of each With the LSM system, the plasma source size was small compared to the dimensions of the apertures used to collimate the XUV radiation On the other hand, the slit widths in the OMA system were comparable to the plasma dimensions and not all of the plasma was viewed (i e , a degree of spatial resolution was present)

The location of a plasma with respect to the optical axis of the OMA or LSM system may also have varied to a small extent from plasma to plasma, though every effort was made to ensure identical conditions existed in each case Also, variations in target geometry, surface quality (e g polished or dull, cylindrical or planar) and degree of oxidation will affect the plasma-production characteristics

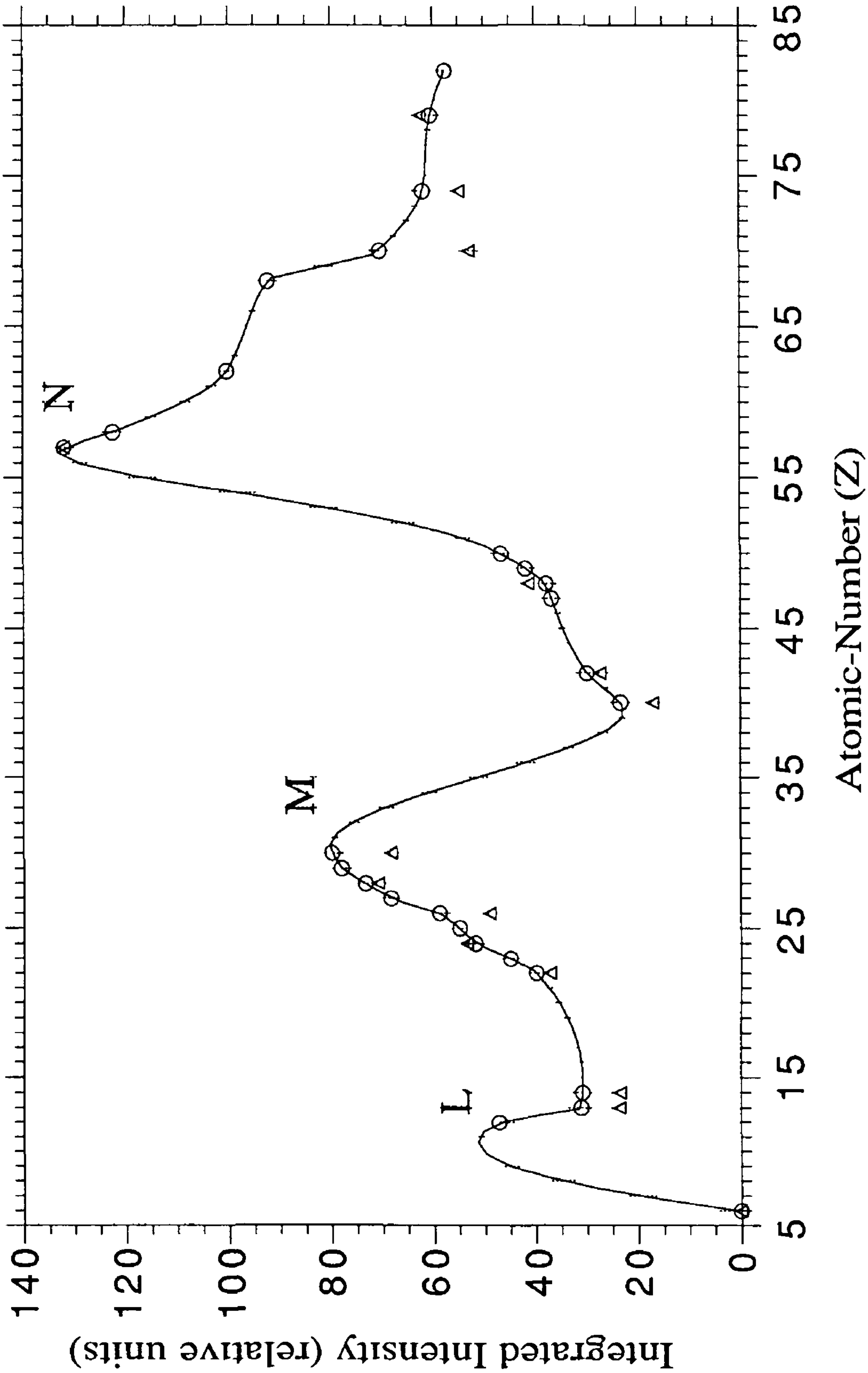

Figure 4.9 The relative integrated XUV intensity as a function of atomic-number for a laser power density of ~5 × 10^{11} W cm^{-2}. The solid line is drawn for the LSM results only as a visual guide

An assumption has been made that the grating efficiency E^{OMA} is constant across the 6 03 eV bandwidth and although the variation is expected to be quite small, for even better interpretation of the OMA Z-dependence, it is necessary to determine the efficiency and modify the OMA spectra accordingly

The fluorescent quantum efficiency of the NE102A plastic scintillator is not constant with wavelength in the 6 – 62 eV region [12] Efficiency data for NE102A above 62 eV are not available It has therefore been assumed that the fluorescent efficiency of NE102A is constant within the 122 3 – 128 5 eV energy band, but this may not be the case If non-negligible variations are present then the ratio of the XUV fluxes for each system will not be in proportion and hence the integrated intensities measured with the LSM system may deviate from those measured with the OMA system

Concluding Remarks

The XUV flux emission from plasmas of 27 elements roughly spanning the Periodic Table, generated using Nd YAG pulses of power density ~5 × 10^{11} W cm^{-2}, were measured with the XUV flux measurement system (described in chapter 2) in the energy band of 122 3 – 128 5 eV The emission spectra of a number of these elements in the 116 – 136 eV region were recorded using a 2 2 m grazing incidence instrument and used to interpret the flux measurements in terms of the nature of the radiation, and the contributing transition arrays and ion stages The integrated intensities for each of these plasmas as measured with the LSM system are used to generate an atomic-number dependence plot By modifying the OMA spectra with the efficiency of the multilayer mirror and the transmittance of the thin-film composite filter of the multilayer system, and then integrating the modulated spectra between 122 3 and 128 5 eV, a comparable atomic-number dependence plot was created Both plots display a strong dependence on the target-Z which is in reasonable agreement with studies carried out for the x-ray region Three peaks are observed and assigned to the K-, L- and M-shells corresponding to the atomic shells into or between which atomic transitions occured producing the measured radiation

Chapter 5

Double-Pulse Experiment

In this chapter, the details of an experiment based on the generation of a laser-produced aluminium plasma with a pair of time-separated laser pulses obtained by splitting the output of a single Nd:YAG laser into two parts are given. Results on studies of variation of the time-delay between pulses, prepulse to main pulse energy ratio, the effects of overlap between the two laser pulses and of defocussing the prepulse beam are reported. At a constant total pulse energy, an increase in XUV flux of up to 40% was observed under certain conditions for the double-pulse configuration over that produced by single pulse-produced plasmas.

5.1 Philosophy

In recent years, work has been undertaken in various laboratories on the study of methods designed to increase the conversion efficiency of x-ray emission from laser-plasmas. Increasing the plasma scale length or emitting volume has been shown to increase the conversion efficiency in the plasma [79 and references therein]. This has been achieved by (i) using a variable laser pulse duration and/or (ii) by introducing a prepulse ahead of a higher energy main pulse. In option (ii), the first pulse or prepulse heats the solid and creates a plasma which is subsequently heated by the main pulse. Work on this effect was carried out by Kodama *et al* [79] who measured plasma emission in the 1.5 – 5 keV spectral range. In their experiment on the double-pulse approach, a 0.53 μm main pulse of 200 ps (FWHM) was preceded by a 1.05 μm prepulse of the same pulse duration. The laser beams were focussed onto a planar copper target through aspherical lenses with angles of incidence of 35° and 22.5° to the target normal. The power density at the focus of the main laser pulse was 1×10^{14} W cm^{-2} and the prepulse laser intensity and time interval between the two pulses was varied between 2×10^{12} and 9×10^{12} W cm^{-2} and from 1.3 to 3.1 ns, respectively. This experiment produced an enhancement of the optical to x-ray conversion efficiency by a factor of up to 3. It was observed that the x-ray conversion efficiency increased with prepulse intensity and/or inter-pulse time delay.

A similar experiment was carried out on plasma emission by Tom and Woods [80] who concentrated on the 17 – 35 nm spectral range. A gaseous plasma was created with a 100 fs prepulse and subsequently heated with a second time-delayed 100 fs pulse. Both laser pulses possessed fluences of 2.6 J cm^{-2} and with a time-delay of up to 200 ps with respect to each other. It was observed that the x-ray yield increased dramatically with increasing time-delay up to a maximum factor of 19 over that produced by irradiating the unprepared solid with a single pulse of 5.2 J cm^{-2} fluence.

Encouraged by these experiments on sub-nanosecond laser plasma light sources, it was decided to perform a parallel study with our simple table-top Nd:YAG laser plasma source. The laser beam was split into two parts and brought to a common focus on a solid aluminium target. The variations in XUV flux in the ~6 eV bandpass of the multilayer system with (i) time-delay between the prepulse and main laser pulse, Δt, and (ii) prepulse (E_{pp}) to main pulse (E_{mp}) laser energy ratio, ΔE (= E_{pp}/E_{mp}) were investigated. We shall demonstrate in the following that for an aluminium plasma an increase in XUV yield of up to 40% can be obtained, under certain conditions, over that produced by a single laser pulse of the same total energy.

5.2 Experimental Set-up

The arrangement used in the experiment differed very little from that shown in figure 2.1 of chapter 2. The Nd:YAG laser beam was split into two parts using a right-angle prism which intersected the beam and directed the prepulse, by means of internal reflection, towards the aluminium target. The remainder of the pulse, unaffected by the first prism, formed the main pulse. The main pulse then propagated through a series of right-angle prisms which introduced a time-delay of 3 ns m^{-1}. Figure 5.1 shows the beam-splitting arrangement used. The prepulse and main pulse entered the target chamber at approximately 15° and 30° to the target normal, respectively. An upper limit on the time-delay between the pre- and main laser pulses of ~9 ns was set by restrictions on the available optical path length. The laser beams were focussed via two f/5 plano-convex lenses of 100mm focal length. The energy in each pulse was measured with an energy monitor at each lens position. Burn patterns of both pulses were recorded on blackened photographic paper following each change in Δt and/or ΔE to monitor the division of the Nd:YAG pulse. Superposition of pre- and main focussed laser spots on the target surface was accomplished by monitoring the XUV output which reached its maximum value at optimum overlap. The laser spot positions were optimised by adjusting the lenses which were mounted on X-Y-Z micrometer stages. All measured XUV fluxes used in the following result sections were averaged over 10 laser shots.

It was not feasible to examine all possble combinations of time-delay and pulse energy ratio due to time restrictions. It was therefore decided to conduct the pulse energy ratio dependence experiment using a fixed 4 ns delay as it lay in the middle of the time-delay range available to us. Once ΔE_{op} was found, the time-delay dependence was then investigated. In these conditions, the laser pulse energy ratio was subsequently varied until the value ΔE_{op}, which optimises the sought effect, was found. The effect of varying the time-delay between the two pulses at the fixed value near ΔE_{op} was also investigated (see below for details).

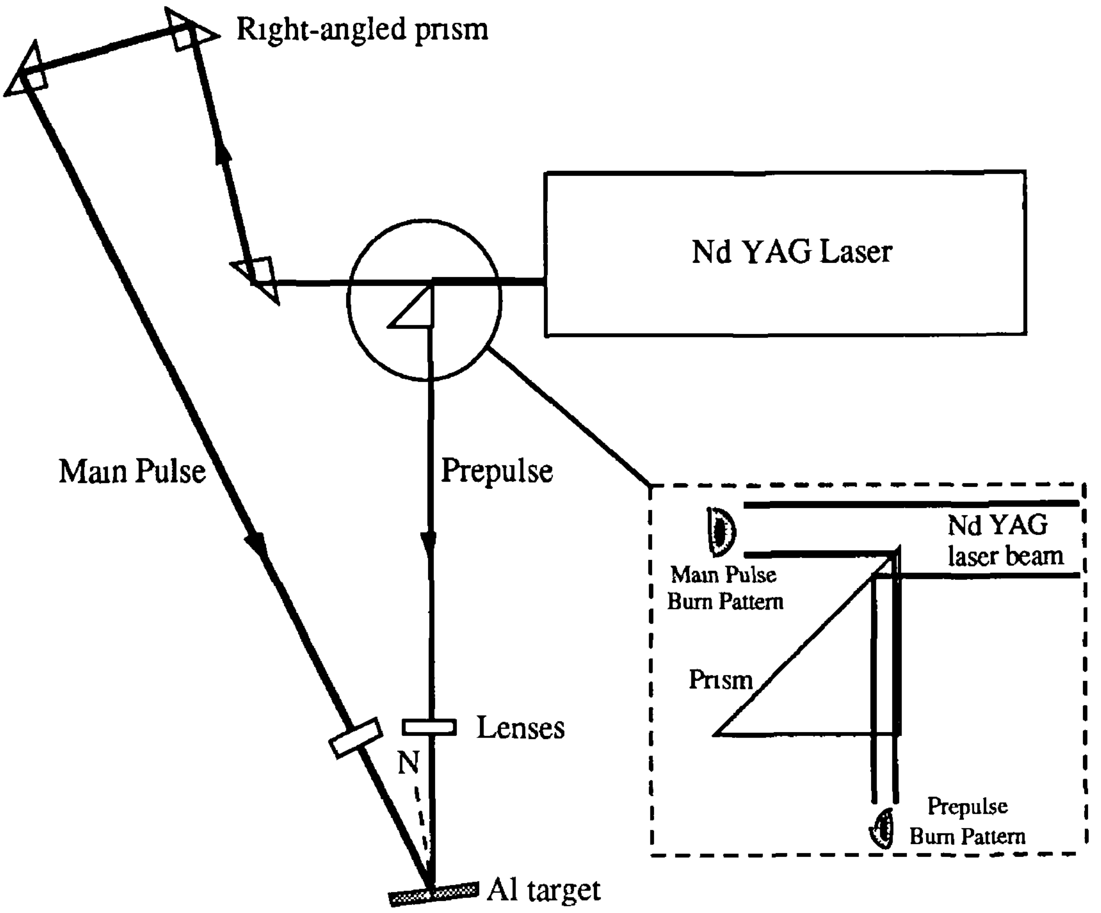

Figure 5 1 Generation of the prepulse and main pulse using right-angle prisms

5.3 Pulse Energy Ratio Dependence

The results presented here are valid in the context of a time-delay of $\Delta t = 4$ ns Figure 5 2 shows the percentage XUV intensity gain obtained from the double-pulse technique over that generated by a single laser pulse of the same total energy The pulse energy ratio, $\Delta E = E_{pp}/E_{mp}$, ranged from 0 16 to 1 As can be readily seen, an enhancement of 18% was achieved for an optimal pulse energy ratio of ΔE_{op} = 0 5 The total energy in both laser pulses, E_t, amounted to 350 mJ in 10 ns of unfocussed energy Thus, for ΔE = 0 5, the prepulse energy was ~115 mJ and the main pulse energy was ~235 mJ For ΔE = 0 16 and 0 34, one finds that $E_{pp} \approx$ 50 and 90 mJ, respectively Thus, $E_{mp} \approx$ 300 and 260 mJ, respectively At these ratios, there was no real enhancement effect measured For ratios greater than 0 5, it appears that the gain effect is reduced, but still appreciable, falling to around 13% for ΔE = 0 62 with $E_{pp} \approx$ 132 mJ and $E_{mp} \approx$ 218 mJ In the case of $\Delta E = 1$, the gain is about 11 5% with $E_{pp} = E_{mp} \approx$ 175 mJ Displayed in figure 5 3 is the XUV emission from an aluminium plasma created with a double and single laser pulse In the case of the double-pulse, the pulse energy ratio is 0 5, i e , at the point of maximum enhancement using a 4 ns time-delay

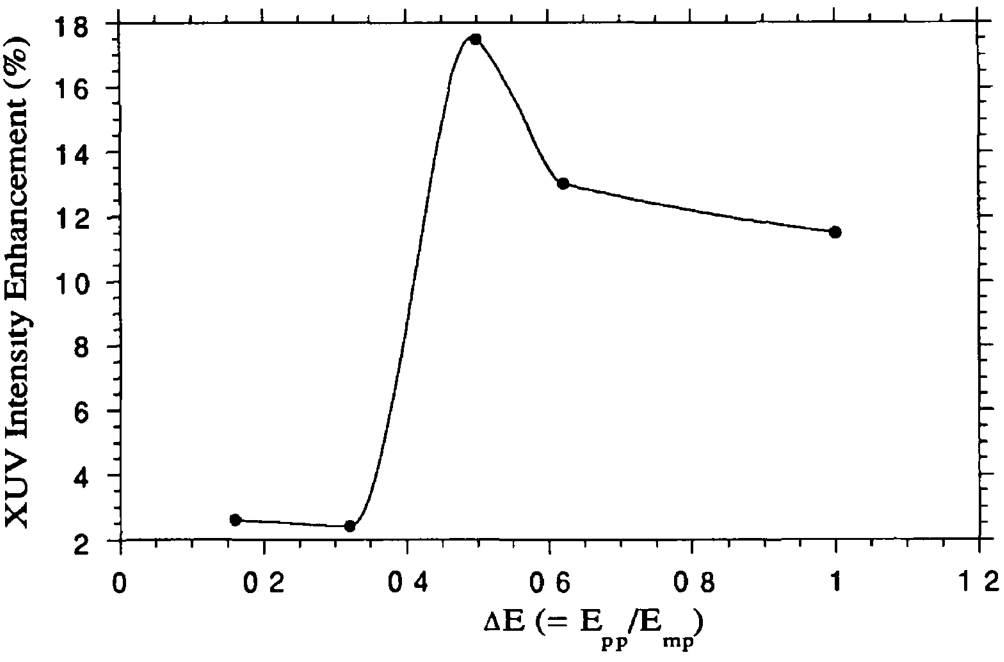

Figure 5 2 Measured XUV enhancement as a function of pulse energy ratio for an aluminium plasma in the 6 eV bandpass of the detector

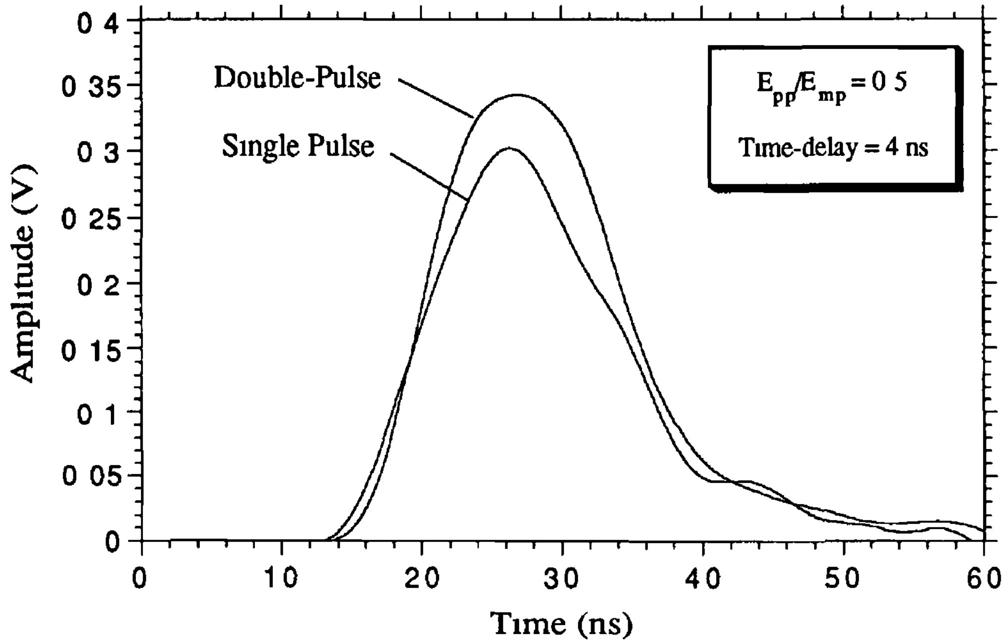

Figure 5 3 Measured XUV emission from aluminium plasmas created from double and single laser pulses using a time delay of 4 ns and a pulse energy ratio of 0 5

5.4 Time-Delay Dependence

The results of the time-delay dependence experiment presented here were carried out for a pulse energy ratio of 0.4. Figure 5.4 shows the variation of the measured integrated XUV flux for the double-pulse approach with a variable time-delay up to 9 ns introduced between the prepulse and main pulse.

For Δt = 0 ns, one can expect that the situation is exactly that of a single laser pulse of energy 350 mJ. For Δt = 1 ns, the XUV flux intensity generated by the single and double-pulse is the same. This is expected since the pulse duration is of the order of 10 ns. It is not until Δt = 3 ns that a difference in the emitted flux appears. At Δt = 5 ns the effect is still on the increase. The highest enhancement observed is for Δt = 7 ns reaching up to 40%. The corresponding XUV pulses measured for the double and single laser pulses are shown in figure 5.5. Figure 5.6 plots the percentage XUV intensity gain from using the double-pulse technique over that produced by a single pulse of the same total laser energy ($E_t = E_{pp} + E_{mp} \approx 350$ mJ) at these time-delays. Of note is the percentage loss of 30% at a time-delay of 9 ns. This may be accounted for by the fact that after 9 ns, the preformed plasma has expanded and cooled significantly through recombination of electrons with ions. Therefore the main pulse energy is now, to some extent, expended in the creation of new electrons in the gas rather than heating existing free electrons. Also, absorption of the XUV emission by an expanding cooling plasma may be significant.

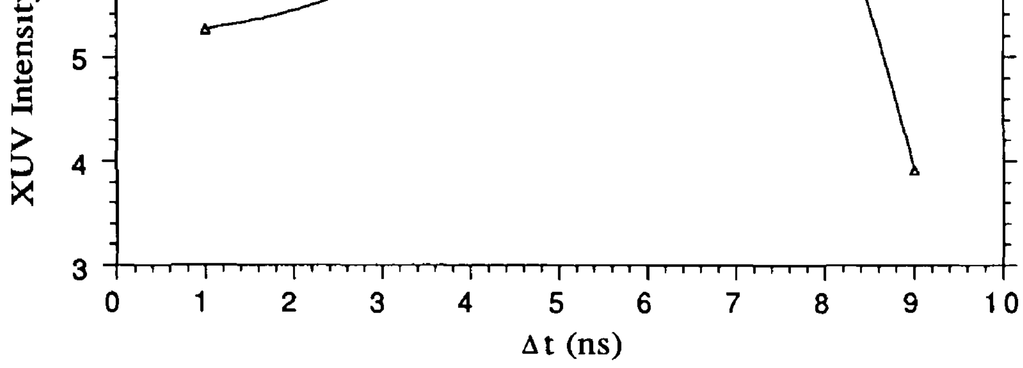

Figure 5.4 The integrated XUV flux intensity as a function of time-delay between the prepulse and main pulse

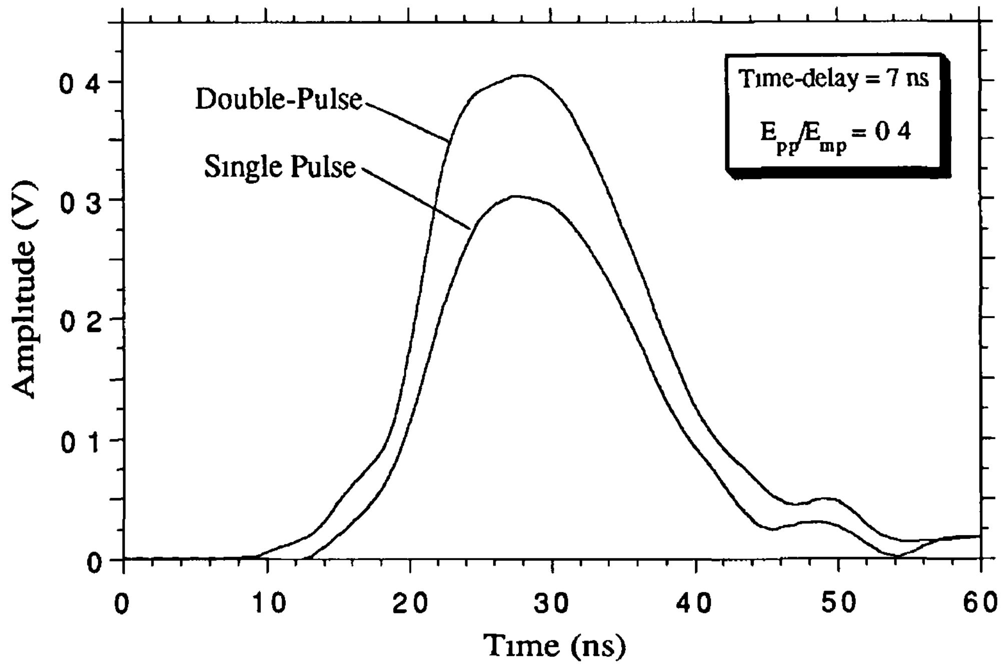

Figure 5 5 Measured XUV emission from double-pulse and single pulse (of same total energy) for a time-delay of 7 ns

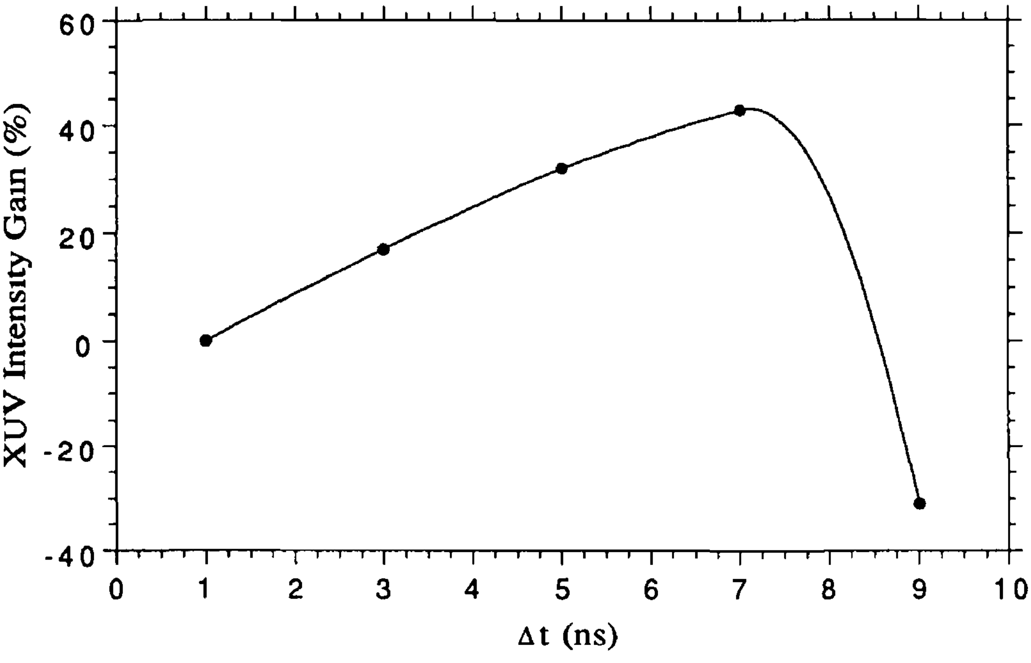

Figure 5 6 The percentage XUV flux enhancement measured as a function of time-delay between the prepulse and main pulse for the double pulse over that produced by a single laser pulse of the same total energy.

5.5 Prepulse Spatial Dependence

Variations of the overlap of the prepulse with the main pulse on the target surface and its affect on the measured XUV flux intensities was investigated Also studied was the effect of defocussing the prepulse on the target surface to attempt to improve overlap between the prepulse and main pulse For both of these experiments, ΔE = 0 5 and Δt = 7 ns

Figure 5 7 shows the variation in the XUV flux intensity as the prepulse is scanned from "behind" the main pulse position to a location "in front" of the main plasma, i e , as viewed in the direction of the optical axis of the system by the detector Negative values of the prepulse position indicate that the prepulse is behind the main pulse, the situation is reversed for positive values As the prepulse travels across the main pulse, three distinct stages must be considered

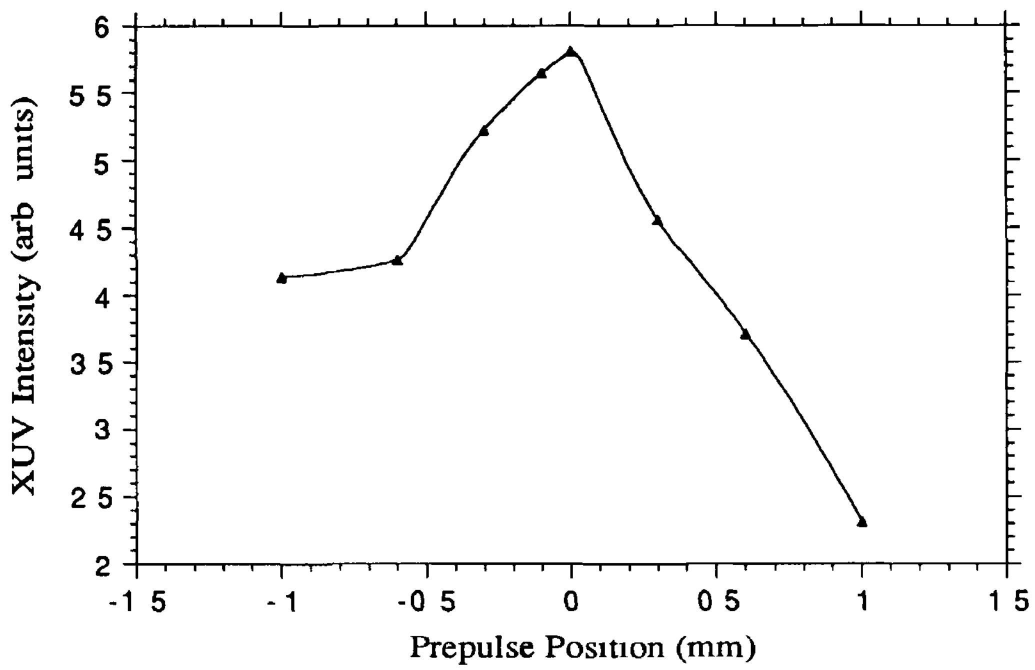

Figure 5 7 Measured XUV flux intensity as a function of position of the prepulse with respect to the main pulse A prepulse position of 0 mm corresponds to complete overlap between the laser pulses

(i) When the preformed plasma is behind the main plasma the measured XUV radiation is mostly due to emission from the main plasma Both plasmas are spatially separated and radiation emitted from the preformed plasma must propagate through the main plasma In doing so it can, to a greater or lesser extent, be absorbed by the main plasma Such absorption is not likely to be strong as the main plasma is hot and a significant depopulation of the ion ground state is expected This situation is seen for prepulse positions from -1 to -0 6 mm This configuration is analogous to a dual laser plasma set-up where the fore plasma forms an absorbing column for the backlighting plasma.

(ii) As the prepulse moves closer to the main laser pulse position, the measured intensity begins to increase as can be seen for a prepulse position of 0.3 mm. For prepulse positions of 0.1 mm and 0 mm, overlap between the laser pulses is good and the measured XUV intensity is maximum. The main laser pulse is heating the preformed plasma under optimal conditions and the enhancement factor is anticipated to be at a peak.

(iii) When the prepulse is in front of the main laser pulse position, measured XUV radiation is due mainly to emission from the preformed plasma. Radiation emitted from the main plasma must propagate through an expanding and cooling pre-plasma and in doing so is strongly attenuated. Therefore, the overall measured intensity begins to drop.

Figure 5.8 demonstrates the effects of defocussing the prepulse laser beam.

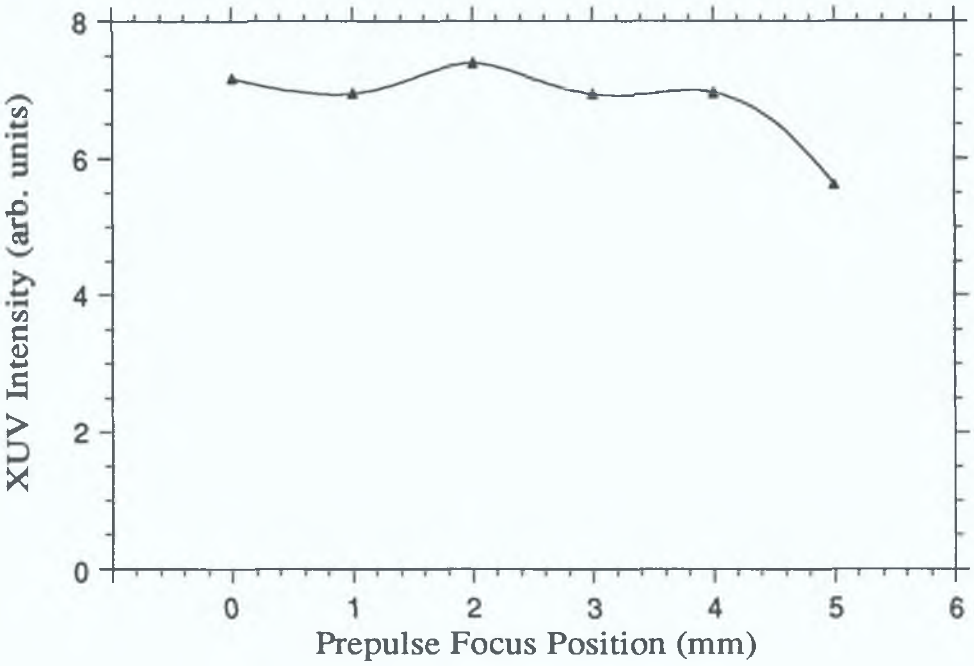

Figure 5.8 Measured XUV flux intensity as a function of prepulse focussing conditions. A focus position of 0 mm corresponds to a focussed prepulse beam.

When the prepulse is focussed on the target surface, the reading on the x-axis of figure 5.8 is 0 mm. The lens was then moved closer to the target in 1 mm steps such that the focus of the prepulse was "beneath" the target surface, thereby increasing the size of the laser spot. As can be seen in figure 5.8, defocussing of the prepulse laser spot did not seem to improve matters, but rather as the beam was defocussed by 5 mm, the overall XUV intensity reduced by roughly 30%. It would seem that as the laser spot is increased in area that the overlap is improving but at the cost of the lower temperature of the preformed plasma. Thus, the plasma is cooler and a greater fraction of the XUV radiation from the main pulse is attenuated.

Concluding Remarks

By producing a small priming plasma with a prepulse momentarily before the main laser pulse is incident on a target surface, the main pulse energy can be more efficiently absorbed in that thin plasma layer to generate a higher XUV flux intensity or conversion efficiency than that produced by a single laser pulse heating a cold solid target For our conventional Nd YAG source, an enhancement of up to 40% was observed for a time-delay of 7 ns between the pulses, and an enhancement of approximately 18% was found when the prepulse-to-main pulse energy ratio is 0 5 using a time-delay of 4 ns The importance of accurate overlap was noted by scanning the prepulse across the stationary main pulse When poor overlap is present, the plasmas formed are separated in space and the resultant measured radiation reduced due to absorption of emitted radiation from the rear plasma by the fore plasma Defocussing of the prepulse may improve overlap, but produces a cooler plasma with fewer free electrons and thus reduces absorption of the secondary laser radiation in the preformed plasma.

Finally, a comment on possible errors While experiments were carried out with great care, factors beyond our control may have affected the quality of the results Firstly, the optical path length over the main laser beam travelled was a few metres more than that covered by the prepulse laser beam The beam divergence (~2 mrad) increased the radius of the main laser spot at the lens with distance For long time-delays (> 5 ns) the spot diameter was quite large Although the lense was larger than the beam diameter, slight variations in focussing may have occured with increasing time-delay Secondly, since the main laser pulse was propagating over quite long distances, the air through which the beam travelled may have suffered refractive index variations due to the energy variations across the beam profile The resultant refractive index variations may cause lensing effects to the laser beam and thus alter its beam profile and therefore effect the focussed energy distribution on the target surface It is beyond the scope of this work to quantify these non-linear effects, but it is important that their affects be recognised

Conclusions

A novel XUV light source has been developed which combines a laser-plasma and multilayer mirror Plasmas were created using a conventional Nd YAG laser system (0 5 J in 10 ns) with focussed power densities of approximately 5×10^{11} W cm^{-2} These plasmas emitted in 4π sr over a broad spectral range from (predominantly in) the XUV to the infrared spectra region A small solid angle of radiation emitted from a plasma was captured by a series of apertures to form the beam incident on the NiCr/C multilayer mirror at an angle of 45° Multilayer optics are low-resolution dispersive elements with high XUV reflectivities at near-normal (or normal) angles of incidence Thus, they offer a number of advantages over grazing incidence optics such as (i) wider range of acceptance angles and (ii) higher flux throughput The NiCr/C multilayer has a measured peak reflectivity of 8 5% at 125 4 eV for an angle of incidence of 45° with a bandwidth of 6 eV full-width at half-maximum Further, diffracted radiation lies in a narrow band from 122 3 to 128 5 eV with a spatial dispersion of 0 22 eV mm^{-1}

The range of ion stages and electron temperatures associated with plasmas generated by the Nd YAG laser used in the work reported here were unknown before commencement of this work The XUV emission spectrum of an aluminium plasma was therefore recorded using a 2 m grazing incidence spectrometer As the XUV spectra of most ions of aluminium are well known, it represented a good choice of target material Higher-Z metals of cobalt through zinc were simultaneously recorded for comparison The ionisation model of Colombant and Tonon was employed to check for consistency in the diagnostics It was observed from the photographic plates that the predominant ion stage was Al IX which corresponds to an electron temperature of ~111 eV The laser power density was then estimated to be approximately 6×10^{11} W cm^{-2} In chapter 2, the laser power density was estimated to be about 5×10^{11} W cm^{-2} which, according to the ionisation model, produces an electron temperature of ~100 eV and a predominant ion stage of Al VIII In the case of the transition metal series from Co – Zn, better agreement was observed because the ionisation model is more applicable to heavier elements than lighter ones During this study, a number of previously unobserved spectral lines for the Co – Zn were classified for the transition arrays $3s^23p^n - 3s^23p^{n-1}4s$ for n = 1, 3, 4 with the help of *ab initio* Configuration Interaction Hartree-Fock calculations

The flux measurement system described in chapter 2 was used to investigate the atomic-number dependence of the emitted XUV radiation from laser-plasmas It was noted from the measured pulses that the XUV emission around 125 eV ocurred in a 25 ns duration or less The integrated intensity for each XUV pulse was plotted as a function of target atomic-number (Z) It was observed that this XUV flux was strongly dependent on atomic-number, displaying distinct peaks at magnesium, zinc and lanthanum In conjunction with these measurements, the emission spectra within the same energy region were recorded using a 2 2 m grazing incidence spectrometer equipped with an Optical Multichannel Analyser (OMA) The purpose here was two-fold, firstly, to gain an understanding of the nature of the XUV radiation contributing to the measured radiation and, secondly, to generate a complementary Z-dependence plot which could be compared to that produced by the multilayer system As expected, we observed that for low-Z targets, line emission dominates over continuum emission As Z increases, the continuum (mainly due to recombination) grows monotonically in relative strength to line emission In the case of the lanthanides, the emission spectra consisted of hundreds of thousands of dense lines which appeared continuum-like High-Z targets produced smooth continuum with no measurable lines in the spectrum From section 2 6 of chapter 2, we recall that the integrated flux measured by the OMA system could be made proportional to that measured with the multilayer system by modulating the recorded emission spectra with the multilayer efficiency and the transmittance of the thin-film composite filter, and then integrated within the 6 03 eV bandpass of the multilayer system These data were plotted on the same graph as the multilayer results A similar chemical trend was observed for both graphs Peaks and troughs were observed which were strongly dependent on the target-Z Peaks measured with the OMA system occurred at copper and lanthanum For both plots, the brightest plasma in the 122 3 – 128 5 eV range was lanthanum and the weakest was carbon A number of reasons were invoked to explain deviations from overlap of the Z-dependence plots, such as (i) not viewing the same region of the plasma, (ii) slight variations in production conditions from plasma to plasma, (iii) not accounting for the quantum efficiency of scintillator, and (iv) not accounting for variations of the grating efficiency within the ~6 eV energy region of interest The observed Z-dependences were quite similar in structure to those measured for the x-ray spectral region

An important property of laser-plasma light sources is their brightness One way of increasing the x-ray photon yield from a plasma employs a weak prepulse to produce a plasma which is subsequently heated with a time-delayed and more intense laser pulse This technique has been successfully applied to the femtosecond and picosecond laser pulse regime Inspired by such experiments, we have performed a similar investigation with our table-top nanosecond laser source on an aluminium plasma using the multilayer system The single Nd YAG laser beam was split into two separate beams The main goal was to see if an XUV enhancement effect could be observed using double pulse over that produced with a single laser pulse of the same total energy With a fixed time-delay of 4 ns between the prepulse and main laser pulse, a gain of 18% was measured for a prepulse to main pulse energy ratio of 0 5 Results of varying the time-delay from 1 – 9 ns between the pulses for a fixed energy ratio of 0 4 yielded an XUV enhancement of up to 40% Also examined was the dependence of prepulse focussing and overlap with respect to the main pulse We measured no gain enhancement from defocussing the prepulse On the other hand, we observed how critically the XUV enhancement depends on the spatial overlap between the prepulse and main pulse When poor overlap is present, plasmas are separated in space and the fore plasma forms an absorbing column for the rear plasma, thereby reducing the overall measured flux

Finally, arising from the initial study reported here, a number of avenues for future study should be pursued

(a) The encouraging data on double-pulse plasma production warrants further experimental study using both (i) the LSM flux measurement system and (ii) the 2 2 m grazing incidence spectrometer Studies of the dependence of the XUV flux on target-Z, pre- and main pulse irradiance, laser wavelength, etc could be made using system (i) An intercomparison of the spectra of single and double pulse produced plasmas could be preformed using system (ii)

(b) The source described in this work also has the useful property of emitting reasonably intense polarised radiation Hence it could be applied to the study of photoionisation of laser-excited aligned atoms (e g [104]) or magneto-optical properties of magnetic materials in the XUV (e g [105]), two areas of intense research but currently confined to synchrotron facilities containing wiggler-undulator sections capable of producing polarised radiation (purity ~ 80 – 95%)

(c) Finally, combined with suitable optics and scintillator for XUV-to-visible down conversion, a gated image-intensified CCD imaging system, currently used with optical filters for time/space/spectrally resolved imaging of laser-plasmas, could have its operation extended into the XUV Such a system could provide useful information on the evolution of plasma parameters in both space and time in a concise image format

References

[1] R J Collins, D F Nelson, A L Schawlow, W Bond, C G S Garret and W Kaisers, Phys Rev Lett , **5**, p303 (1960)

[2] L Tonks and I Langmuir, "Oscillations in ionised gases" Phys Rev , **33**, p195 (1929)

[3] W Cookes, Phil Trans , **1**, p135, (1879)

[4] F I Boley, "Plasmas-Laboratory and Cosmic", Published for the Commission on College Physics (1966)

[5] N A Krall and A W Trivelpiece, "Principles of plasma physics", International series in Pure and Applied Physics, McGraw-Hill (1973)

[6] F H Coensgen, W F Cummins and A E Sherman, Phys Fluids, 2, p350 (1950) Cited in [5]

[7] J Marshall, Phys Fluids, 3, p135 (1960) Cited in [5]

[8] A W Trivelpiece, "Slow wave propagation in plasma wave guides", Wiley, New York (1968) Cited in [5]

[9] W I Linlor, Appl Phys Lett , 3, p210 (1963)

[10] J C Boyce, Rev Mod Phys , **13**, No 1 (1941)

[11] R Tousey, J Opt Soc Am , **52**, p1186 (1962)

[12] J A R Samson, "Techniques of vacuum ultraviolet spectrocopy", Wiley, New York (1967)

[13] R W P McWhirter in "Plasma Diagnostic Techniques", P H Huddlestone and S L Leonard, eds, Chapt 4, Academic Press, New York (1965)

[14] E Hecht, "Optics", Addison-Wesley, Canada (1987)

[15] T W Johnston and J M Dawson, Phys Fluids **16**, p722 (1973)

[16] P.K. Carroll and E.T. Kennedy, "Laser-produced plasmas", Contemp. Phys., **22**, No.1, p61 (1981).

[17] F. Bijkerk and A.P. Bevelko, "Laser-plasma XUV sources, A role for excimer lasers?", Invited Paper, SPIE Vol. **1503**, Excimer lasers and applications III (1991).

[18] H. Motz, "The physics of laser fusion", Academic Press (1979).

[19] T.P. Hughes, "Plasmas and laser light", Adam Hilger (1975).

[20] D. Colombant and G.F. Tonon, "X-ray emission in laser-produced plasmas", J. Appl. Phys., 44, No.8 , p61(1973).

[21] D.R. Bates, A.E. Kingston and R.W.P. McWhirter, Proc. Roy. Soc., **A257**, p297 (1962).

[22] D. Nagel, C.M. Brown, M.C. Peckerar, M.L. Ginter, J.A. Robinson, T.J. McIlrath and P.K. Carroll, "Repetitively pulsed-plasma soft x-ray source", Appl. Opt., **23**, No.9 (1984).

[23] P. Gohil, H. Kapoor, D. Ma, M.C. Peckerar, T.J. McIlrath and M.L. Ginter, "Soft x-ray lithography using radiation from laser-produced plasmas", Appl. Opt., **24**, No.13, p2024 (1985).

[24] D.S. DiCicco, D. Kim, R. Rosser and S. Suckewer, "First stage in the development of a soft x-ray reflection imaging microscope in the Schwarzchild configuration using a soft x-ray laser at 18.2nm", Opt. Lett., **17**, No.2, p157 (1992).

[25] D.A. Tichenor, G.D. Kubiak, M.E. Malinowski, R.H. Stulen, S.J. Haney, K.W. Berger, L.A. Brown, R.R. Freeman, W.M. Mansfield, O.R. Wood II, D.M. Tennant, J.E. Bjorkholm, A.A. MacDowell, J. Bokor, T.E.Jewell, D.L. White, D.L Windt and W.K. Waskiewicz, "Diffraction-limited soft x-ray projection imaging using a laser plasma source", Opt. Lett., **16**, No.20, p1557 (1991).

[26] I.C.E. Turcu, M.C. Gowar, C.J. Reason, P. Huntington, M. Schulz, A.G. Michette, F. Bijkerk, C. Louis, G.J. Tallents, Y. Al-Hadithi and D. Batani, "100Hz KrF laser-plasma x-ray source", SPIE Vol. **1503**, Excimer lasers and applications III (1991).

[27] Hampshire Instruments Inc., Marlborough M.A. 01752 USA.

[28] R A Gutcheck and J J Muray, "Intense plasma source for x-ray microscopy", SPIE Vol **316**, High Resolution Soft X-ray Optics (1981)

[29] R J Rosser, K G Baldwin, R Feder, D Bassett, A Coles and R W Eason, J Microscop , **138**, p311 (1985)

[30] R Feder *et al*, "X-ray microscopy", Springer-Verlag, Berlin (1984)

[31] G R Morrison *et al*, "X-ray microscopy II", Springer-Verlag, Berlm (1988)

[32] J A Trail and R L Byer, "Compact scanning soft x-ray microscope using a laser-produced plasma source and normal incidence multilayer mirrors", Opt Lett , **14**, No 11, p539 (1989)

[33] H Daido, I C E Turcu, I N Ross, J G Watson, M Steyer, R Kaur, M S Schulz and M Amit, "Spatial coherence of a repetitive laser-plasma point x-ray source in the water window spectral region", Appl Phys Lett , **60**, No 10 (1992)

[34] P J Mallozzi, R E Schwerzel, H M Epstein and B E Campbell, "Fast-extended-x-ray-absorption-fine-structure spectroscopy with a laser-produced x-ray pulse", Phys Rev A, **23**, No 2, p824 (1981)

[35] R W Eason, D K Bradley, J D Kilkenny and G N Greaves, "Improved laser-EXAFS studies of aluminium foil", J Phys C Solid State Physics, **17**, p5067 (1984)

[36] P K Carroll, E T Kennedy and G O'Sullivan, "New continua for absorption spectroscopy from 40 to 2000 Å", Opt Lett , **2**, p72 (1978)

[37] P K Carroll, E T Kennedy and G O'Sullivan, "Laser-produced continua for absorption spectroscopy in the vacuum ultraviolet and XUV", Appl Opt , **19**, p1454 (1980)

[38] P K Carroll and E T Kennedy, "Doubly excited autoionisation resonances in the absorption spectrum of Li^+ formed in a laser-produced plasma", Phys Rev Lett , **38**, p1068 (1977)

[39] P K Carroll and J T Costello, "Giant-dipole-resonance absorption in atomic thorium by a novel two-laser technique", Phys Rev Letts , **57**, No 13, p1581 (1986)

[40] J T Costello, J P Mosnier, E T Kennedy, P K Carroll, and G O'Sullivan, "XUV absorption spectroscopy with laser-produced plasmas, A review", Phys Scri , **T34**, p77 (1990)

[41] B C Fawcett, A H Gabriel, F E Irons, N J Peacock and P A H Saunders, Proc Phys Soc , **88**, p1051 (1966)

[42] B C Fawcett, "Classification in the early 1980's of the spectra of highly ionised atoms", J Opt Soc Am B, **1**, No 2 (1984)

[43] I Martinson, "The spectroscopy of higly ionised atoms", Rep Prog Phys , **52**, p157 (1989)

[44] G O'Sullivan, "Atomic structure of highly ionised atoms", Comments At Mol Phys , **28**, No 3, p143 (1992)

[45] G Befeki, C Deutsch and B Yaakobi, "Spectroscopic diagnostics of laser plasmas", in "Principles of laser plasmas", ed by G Befeki, Chapt 13, Wiley (1976)

[46] G M Zeng, H Daido, K Murai, Y Kato, M Nakatsuka and S Nakai, "Line x-ray emissions from highly ionised plasmas of various species irradiated by compact solid state lasers", J Appl Phys , **72**, No 8, p3355 (1992)

[47] C DeMichelis and M Mattioli, Rep Prog Phys , **47**, p1233 (1984)

[48] C L S Lewis in "Laser-plasma interactions 4", ed by H B Hooper, Chapt 12, Proc 35th Scottish Universities Summer School in Physics, p317 (1988)

[49] D M O'Neill, C L S Lewis, D Neely, Y Kato, H Daido, H Shiraga, H Azuma, K Murai, Y Yang, E Miura, M Ohmi, H Takaben, T Kanabe, M Takagi and S Nakai, "Collaborative work at the institute of laser engineering on the Ne-like Ge XUV laser scheme", Central Laser Facility (SERC) Ann Rep (1992)

[50] F E Irons and N J Peacock, J Phys B At Mol Phys , **7**, p1109 (1974)

[51] S Suckewer, C H Skinner, H Milchberg, C Keane and D Voorhees, "Amplification of stimulated soft-x-ray emission in a confined plasma column", Phys Rev Letts , **55**, No 17 (1985)

[52] P Jaegle, G Jamelot, A Carillon and C Wehenkel, J Appl Phys , **17**, p4483

(1978)

[53] A N Zherkin, K N Koshelev and V S Letokhov, Sov J Quant Elect , **6**, p82 (1976)

[54] D L Matthews, P L Hagalstein, M D Rosen, M J Eckart, N M Ceglio, A U Hasi, H Medeci, B J MacGowan, J E Trebes, B L Whitten, E M Campbell, C W Hatcher, A M Hawryluk, R L Kauffman, L D Pleasance, G Rambach, J H Scofield, G Stone and T A Weaver, Phys Rev Letts , **54**, p110 (1985)

[55] D L Matthews *et al*, in "X-ray laser 1990", ed by G Tallents, Conf Series No 116 (IOP, Bristol, UK), p205 (1991)

[56] A Carillon, H Z Chen, P Dhez, L Dwivedi, J Jacoby, P Jaegle, G Jamelot, J Zhang, M H Hey, A Kidd, A Klisnick, R Kodama, J Krishnan, C L S Lewis, D Neely, P Norreys, D O'Neill, G J Pert, S A Ramsden, J P Raucourt, G J Tallents and J Uhomoibhi, "Saturated and near-diffraction limited operation of a Ge XXIII laser at 23 6 nm", Central Laser Facility (SERC) Ann Rep (1992)

[57] R C Elton, "X-ray lasers", Academic Press (1990)

[58] G J Linford, E R Peressini, W R Sooy and M L Spaeth, Appl Opt , **13**, p379 (1974)

[59] D L Matthews, E M Campbell, N M Ceglio, G Hermes, R Kauffman, L Koppel, R Lee, K Manes, V Rupert, V W Slivinsky, R Turner and F Ze, "Characterisation of laser-produced plasma x-ray sources for use in x-ray radiography", J Appl Phys , **54**, No 8 (1983)

[60] O Willi, "Diagnostics and experimental methods of laser-produced plasmas" in "Laser-plasma interactions 4", Ed H B Hooper, Proc 35th Scottish Universities Summer School in Physics, p285 (1988)

[61] R Benattar and J Godart, "On the use of x-ray radiation to probe laser created plasmas by refractometry", Opt Comm , **49**, No 1, p43 (1984)

[62] J A Trail, R L Byer and T W Barbee Jnr, Appl Phys Lett , **52**, p279 (1988)

[63] S Nakayama, M Yanagihara, M Yamamoto, H Kimura and T Namioka, "Soft x-ray reflectometer with a laser-produced plasma source", Phys Scripta, **41**,

p754 (1990).

[64] H. Azuma, Y. Watanabe, Y. Kato, T. Motohiro, S. Noda and K. Murai, "Single-shot measurement of spectral reflectance of a soft x-ray multilayer mirror using a laser-plasma x-ray source", Jpn. J. Appl. Phys., **31**, Pt.2, No.2B, pL203 (1992).

[65] G. Ballofet, J. Romand and B. Vodar, Comp. Rend. Acad. Sci. (Paris), **252**, p4139 (1961).

[66] M. Kühne, "Radiometric comparison of a laser-produced plasma and a BRV-source plasma at normal incidence", Appl. Opt., **21**, No.12 (1982).

[67] M. Kühne and B. Wende, "Vacuum UV and soft x-ray radiometry", J. Phys. E: Sci. Instrum., review article (1983).

[68] J. Fisher, M. Kühne and B. Wende, "Spectral radiant power measurements of VUV and soft x-ray sources using the electron storage ring BESSY as a radiometric standard", Appl. Opt., **23**, No.23, p4252 (1984).

[69] P.K. Carroll E.T. Kennedy and G. O'Sullivan, "Table-top EUV continuum light source", IEEE J. Quantum Elec., **QE-19**, No.12, p1807 (1983).

[70] J.A. McMordie and A.C. Simmons, "X-ray emission from CO_2-laser-produced plasmas at powers up to 10^{11}W/cm^2 for 26 elements", J. Phys.D: Appl. Phys., **8** (1975).

[71] R.D. Bleach and D.J. Nagel, "Plasma x-ray emission produced by ruby lasers at 10^{12} W/cm^2", J. Appl. Phys., **49**, No.7, p3832 (1978).

[72] K.M. Glibert, J.P. Anthes, M.A. Gusinov and M.A. Palmer, "X-ray yields of plasmas heated by 8-nsec neodymium laser pulses", J. Appl. Phys., **51**, No.3, p1449 (1980).

[73] P.D. Gupta, P.A. Naik and H.C. Plant, "Dependence of x-ray intensity scaling on target atomic number in laser-produced plasmas", J. Appl. Phys., **56**, No.5. p1371 (1984).

[74] T. Mochizuki, T. Yabe, K. Okada, M. Hamada, N. Ikeda, S. Kiyokawa and C. Yamanaka, "Atomic-number dependence of soft-x-ray emission from various targets irradiated by a 0.53-μm-wavelength laser", Phys. Rev. A, **33**, No.1, p525 (1986).

[75] W C Mead, E M Campbell, K G Estabrook, R E Turner, W L Kruer, P H Y Lee, B Pruet, V C Rupert, K G Tirsell, G L Stradling and F Ze, "Laser-plasma interaction at 0 53 μm for disk targets of varying Z", Phys Rev Lett , **47**, No 18 (1981)

[76] T W Barbee Jnr, "Advances in multilayer x-ray/EUV optics synthesis, performance and instrumentation", Opt Eng , **29**, No 7, p711 (1990)

[77] C L Cromer, J M Bridges, J R Roberts and T B Lucatorto, "High resolution VUV spectrometer with multichannel detector for absorption studies of transcient species", Appl Opt , **24**, No 18 (1985)

[78] J T Costello and J P Mosnier, private communication, unpublished (1989)

[79] R Kodama, T Mochizuki, K A Tanaka and C Yamanaka, "Enhancement of KeV x-ray conversion in laser-produced plasmas by a weak prepulse laser", Appl Phys Letts , **50**, No 12, p720(1987)

[80] H W K Tom and O R Wood II, "Study of soft x-ray generation by laser-heating solid and gaseous tantalum plasmas with sub-picosecond pulses", Appl Phys Letts , **54**, No 6, p517 (1989)

[81] J H Underwood and T W Barbee Jnr, "Layered synthetic microstructures as Bragg reflectors for x-rays and extreme ultraviolet theory and predicted performance", Appl Opt , **20**, No 17, p3027 (1981)

[82] W Deubner, Ann Phys , Leipzig, **5**, p261 (1930)

[83] J Dumond and J P Youtz, "An x-ray method of determining rates of diffusion in the solid state", J Appl Phys , **11**, p357 (1940)

[84] T W Barbee Jnr , in Proceedings, Topical Conference on Low Energy X-ray Diagnostics, American Institute of Physics, New York (1980)

[85] A G Michette, "Optical systems for soft x-rays", Plenum Press, New York (1986)

[86] R W James, "The principles of the diffraction of x-rays", Oxbow Press, (1982)

[87] T Cafolla, private communication, unpublished (1993)

[88] F R Powell, P W Vedder, J F Lindblom, "Thin film filter performance for extreme ultraviolet and x-ray applications", Opt Eng , **29**, No 6, p614 (1990)

[89] P Choi and M B Favre, "Silver as a soft x-ray filter for plasma diagnostics", J Phys D Appl Phys , **20** , p169 (1987)

[90] H J Hagemann, W Gudat and C Kunz, "Optical constants from the far infrared to the x-ray region Mg, Al, Cu, Ag, Au, Bi, C, and Al_2O_3" J Opt Soc Am , **65**, No 6 (1975)

[91] J Senior, "Optical fibre communications", Prentice-Hall, London (1985)

[92] A Chambers, R K Fitch and B S Halliday, "Basic vacuum technology", Adam Hilger (1989)

[93] J L Wiza, "Microchannel plate detectors", Reprint from Nuc Instr and Methods, **162**, p587 (1979)

[94] M G Shaw, "Spectral Image Processing", M Sc Thesis, Dublin City University, Dublin 9, in progress

[95] R L Kelly, "Atomic and ionic spectrum lines below 2000 Angstroms Hydrogen through Krypton", J Phys Chem Ref Data, **16**, Supp No 1 (1987)

[96] R D Cowan, "Theory of atomic structure and spectra", University of California Press, Berkeley CA (1981)

[97] J Sugar and C Corliss, "Atomic energy levels of the iron-period elements Potassium through Nickel", J Phys Chem Ref Data, **14**, Supp No 1 (1985)

[98] N Nakano and H Kuroda, "X-ray generation from laser-produced plasmas and its atomic-number dependence", Phys Rev A, **27**, No 4, p2168 (1983)

[99] P K Carroll and G O'Sullivan, "Ground state configurations of ionic species I through XVI for Z = 57 - 74 and the interpretation of 4d - 4f emission resonances in laser-produced plasmas", Phys Rev A, **25**, No 1 (1982)

[100] G O'Sullivan, " The origin of line-free XUV continuum emission from laser-produced plasmas of the elements $62 \leq Z \leq 74$", J Phys B At Mol Phys , **16**, p3291 (1983)

[101] G O'Sullivan and P K Carroll, "4d – 4f emission resonances in laser-produced plasmas", J Opt Soc Am , **71**, No 3, p227 (1981)

[102] P K Carroll and G O'Sullivan, "Laser-produced continua for studies in the XUV", SPIE, **1503**, Excimer Lasers and Applications III (1991)

[103] B L Henke, P Lee, T J Tanaka, R L Shimabukuro, B K Fujikawa, "Low-energy x-ray interaction coefficients Photoabsorption, scattering and reflection", At Dat Nuc Dat Tables, **27**, p1 (1982)

[104] S Baier, M Schultz, H Staiger, P Zimmerman, C Lorenz, J Ruder, M Pahler, B Sonntag, J T Costello and L Kiernan, J Phys B At Mol Phys , In Press (1994)

[105] L Baumgarten, C M Schneider, A Peterson, F Schafers and J Kirschner, Phys Rev Lett , **65**, No 482 (1990)

Appendix A

Multilayer Theory

Reflectivities at nongrazing incidence angles may be enhanced by causing multiple reflections to add in phase in a similar manner to Bragg reflecion of x-rays by crystals The Bragg diffraction equation which describes the condition for constructive interference of the mth order reflection is given by

$$m\lambda = 2d \sin\theta_m \qquad \text{(A 1)}$$

At the Bragg angle of reflection, θ_m, all scattered waves will add in phase and the total scattered amplitude will reach a maximum Total reflection from a multilyer mirror in the XUV spectral region is not possible due to the fact that all elements absorb at these wavelengths In order to theoretically determine the performance of a multilayer mirror, it is necessary to solve Maxwell's equations for a system with a periodically varying dielectric constant Two equivalent approaches can be used, (i) treat x-ray reflections from a multilayer mirror in a manner similar to that used to compute Bragg reflection intensities from a naturally or artificially grown crystal or (ii) use an adaption of the optical multilayer theory (based on the Fresnel equations) used for the design of interference coatings for visible radiation The description here follows that of Underwood and Barbee [79] A simplified crystal diffraction theory that neglects absorption is described in section (I) to obtain formulae for estimating the performance of multilayers Optical multilayer theory is used in section (II) to make exact calculations of multilayer performance

Sections (III), (IV) and (V) calculate the optical constants, corrected Bragg angles and corresponding integrated reflectivities or efficiency, respectively, of the NiCr/C multilayer with 25 bilayers and a periodicity of 74 7 Å within the energy bandpass of the XUV flux measurement system

(I) Absorption-Free Dynamical Theory

In treating the reflection of soft x-rays from a natural or pseudo-crystalline structure such as a multilayer, either of two approaches may be adopted

(i) Kinematical theory neglects the details of wave interactions within the structure, in particular, the progressive reduction of the forward wave as it travels into the multilayer The wave is partially reflected by successive planes, a process known as primary extinction The scattering from each volume element is treated as being independent of the scattering from all other volume elements This theory is used to study thin or mosaic crystals

(ii) Dynamical theory takes into account all wave interactions and is customarily used in the study of x-ray diffraction from large perfect crystals

Multilayer mirrors are essentially perfect crystals and it is therefore more suitable to use the dynamical theory to describe their properties Although, if a multilayer can be thought of as being sufficiently thin, then a kinematical approximation may be employed A quantitative description of "thick" and "thin" multilayers is given below

Although absorption in multilayers is non-negligible and may have a significant effect on the shape and intensity of reflections, omission of its effect leads to a simpler theory that gives useful expressions for estimating peak and integrated reflectivities and widths of the Bragg peaks

The complex refractive index of an elemental layer is given by

$$\eta = 1 - \delta - i\beta \qquad \text{(A 2)}$$

where δ is the refractive index decrement and β is the absorption index Each index is related to the atomic scattering factors f_1 and f_2 by

$$\delta = (r_e\lambda^2/2\pi)Nf_1 \qquad \text{(A 3)}$$

and

$$\beta = (r_e\lambda^2/2\pi)Nf_2 \qquad \text{(A 4)}$$

respectively, where N is the number density of atoms (cm^{-3}) and r_e is the classical electron radius e^2/m_ec^2 with c as the speed of light The complex scattering factor is given by

$$f = f_0 + \Delta f_1 + i\Delta f_2 = f_1 + if_2 \qquad \text{(A 5)}$$

where Δf_1 and Δf_2 are the resonance and absorption corrections to the atomic scattering factor arising from anomalous dispersion (the Honls corrections) Now for multilayers with $2d > 10$ Å, $\sin\theta/\lambda < 0\ 1$ Å^{-1} and so thus $f_0 \approx A$, that is, all electrons in an atom can be considered to scatter in phase Thus $f_1 \approx A + \Delta f_1$ and $f_2 = \Delta f_2$

Define the scattering amplitude density for soft x-rays by

$$\Phi = N|f|r_e = N[(A + \Delta f_1)^2 + \Delta f_2{}^2]^{1/2}r_e \qquad \text{(A 6)}$$

Now in the absorption-free case $\Delta f_2 = 0$ and the term in the brackets reduces to $A + \Delta f_1$

In principle, the crystalline structure of the individual layers will contribute to the reflected intensity In practice, however, this structure can be neglected since the lattice spacing is such that Bragg's law cannot be satisfied Therefore, the crystalline structure may be neglected and one need only consider multilayer superlattice diffraction Thus, in the crystal a unit cell may be defined in terms of a bilayer of metals within the multilayer From crystallographic theory, one finds the angle-dependent structures factor F(θ) of a unit cell may then be defined as

$$F(\theta) = \int_0^d \Phi(v)\exp[iQv]dv \qquad \text{(A 7)}$$

where $Q = 4\pi(\sin\theta)/\lambda$ and v is the direction normal to the multilayer surface Let a plane parallel wave of wavelength λ be incident on a multilayer at a glancing angle θ The intensity of the wave is I_0 and the reflected intensity is $I(\theta)$, then using dynamical theory one obtains the reflectivity [81] from a multilayer as

$$I(\theta)/I_0 = \{u^2 + (u^2 - 1)\cot^2[\hat{A}(u^2 - 1)^{1/2}]\}^{-1} \qquad \text{(A 8)}$$

where

$$\hat{A} = 2LdK\,|F(\theta_m)|\,/m \qquad \text{(A 9)}$$

and

$$u = \pi mL[(\theta - \theta_m)\sin 2\theta_m - 2\delta_0)]/2\hat{A}\sin^2\theta_m \qquad \text{(A 10)}$$

The factor K is 1 for the σ-component of the wave polarisation, $|\cos 2\theta_m|$ for the π-component and $(1 + |\cos 2\theta_m|)/2$ for unpolarised radiation δ_0 is the average refractive index decrement for the multilayer, that is,

$$\delta_0 = (r_e\lambda^2/2\pi)\,\Sigma\, N_j^{av}(A + \Delta f_1)_j \qquad \text{(A 11)}$$

where N_j^{av} is the number density of the atoms of type j averaged over the multilayer Equations (A 8), (A 9) and (A 10) imply that a correction for refraction must be applied to the Bragg equation (A 1) Peak reflectivity, R_m^p, for the mth order Bragg reflection is defined as the maximum value of $I(\theta)/I_0$, so differentiating equation (A 8) with respect to u and setting u = 0 yields

$$R_m^p = (I(\theta)/I_0)_{max} = (-\cot^2 i\hat{A})^{-1} = \tanh^2\hat{A} \qquad \text{(A 12)}$$

The integrated reflectivity for the mth order Bragg reflection, R_m^I, is given by

$$R_m^I = {}_0\!\int^{\pi} (I(\theta)/I_0)\, d(\theta - \theta_m) \qquad \text{(A 13)}$$

$$= [\hat{A}(\tan\theta_m)/\pi mL]\ {}_{-\infty}\!\int^{+\infty} (I(\theta)/I_0)\, du \qquad \text{(A 14)}$$

$$= [(\tan\theta_m)/mL]\ \hat{A}\tanh\hat{A} \qquad \text{(A 15)}$$

Equation (A 8) is derived from Ewald's solution which assumes no absorption in the dynamical problem

Equation (A 10) shows that, since the peak reflectivity is at u = 0, the peak does not occur at the Bragg angle but at a slightly larger angle

$$\theta_m^p = \theta_m + 2\delta_0/\sin 2\theta_m \qquad \text{(A 16)}$$

This correction is due to refraction of the x-rays ($\delta_0 \neq 0$) and the Bragg equation needs modification to account for this In the medium, the wavelength of the radiation is λ' where

$$1 - \delta' = \lambda/\lambda' \qquad \text{(A 17)}$$

The glancing angle is θ_m' where

$$m\lambda' = 2d\sin\theta_m' \qquad \text{(A 18)}$$

and therefore by Snell's law,

$$1 - \delta_0 = \cos\theta_m{}^p/\cos\theta_m{}' \qquad (A.19)$$

Using equations (A.17), (A.18) and (A.19), the modified Bragg equation becomes

$$m\lambda = 2d[1 - (2\delta_0 - \delta_0{}^2)/\sin^2\theta_m{}^p]^{1/2} \sin\theta_m{}^p \qquad (A.20)$$

Thick and Thin Multilayers

Two limiting cases of the dynamical theory are defined by $\hat{A} << 1$ and $\hat{A} >> 1$. In the case of $\hat{A} << 1$, we have a thick multilayer (since L is large). This implies that $\tanh \hat{A} \approx 1$ for $\hat{A} > 1.8$ and therefore

$$R_m{}^p = 1 \qquad (A.21)$$

and

$$R_m{}^I = \hat{A} \tan\theta_m/mL \qquad (A.22)$$

In the case of a thin multilayer, $\tanh \hat{A} \approx \hat{A}$ for $\hat{A} < 0.4$, and thus

$$R_m{}^p = \hat{A}^2 \qquad (A.23)$$

and

$$R_m{}^I = \hat{A}^2 \tan\theta_m/mL \qquad (A.24)$$

The dynamical theory at the thin limit approximation corresponds to the kinematical theory.

Evaluation of $|F(\theta)|$

For simple cases, $|F(\theta)|$ may be evaluated in an analytical manner. If the layers A and B (with low and high refractive indices, respectively) are homogeneous with constant scattering amplitude densities Φ_A and Φ_B, with perfectly sharp interfaces between them so that transitions from Φ_B to Φ_A take place over infinitesimally small intervals, then

$$F(\theta) = \int_0^{dA} \Phi_A \exp(iQv)dv + \int_0^{dB} \Phi_B \exp(iQv)dv \qquad (A.25)$$

Evaluating the integrals gives

$$F(\theta) = (1/iQ)[\Phi_A - \Phi_B) \exp(iQd_A) - \Phi_A + \Phi_B \exp(iQd) \qquad (A.26)$$

which gives

$$\begin{aligned} |F(\theta)| &= [F(\theta)F^*(\theta)]^{1/2} \\ &= (\sqrt{2}/Q)[\Phi_A{}^2(1 - \cos Qd_A) + \Phi_B{}^2(1 - \cos Qd_B) \\ &\quad - \Phi_A\Phi_B(1 + \cos Qd - \cos Qd_A - \cos Qd_B)] \qquad (A.27) \end{aligned}$$

If the layer thicknesses are the same, i.e., $d_A = d_B = d/2$, then equation (A.27) becomes

$$|F(\theta)| = (\sqrt{2}/Q) \sin(Qd/4)[\Phi_A{}^2 + \Phi_B{}^2 + 2\Phi_A\Phi_B \cos(Qd/2)] \qquad (A.28)$$

At the Bragg angle, $Q = 2m\pi/d$ and $\cos Qd = 1$ Therefore, equation (A 27) becomes

$$|F(\theta)| = (d/m\pi)(\Phi_B - \Phi_A)\sin(m\pi d_B/d) \qquad \text{(A 29)}$$

which is equal to zero for even order reflections Thus only odd reflections (m = 1, 2, 3,) are permitted by the multilayer If the layer thicknesses are equal but the scattering amplitude density makes a smooth sinusoidal transition from Φ_B to Φ_A then the structure factor may be written

$$F(\theta) = (\Phi_A/2)\int_0^d [1 + \sin(2\pi v/d)]\exp(iQv)dv$$
$$+ (\Phi_B/2)\int_0^d [1 - \sin(2\pi v/d)]\exp(iQv)dv \qquad \text{(A 30)}$$

which gives

$$|F(\theta)| = \sin(Qd/2)[(\Phi_A + \Phi_B)^2/Q^2$$
$$+ (4\pi^2/d^2)(\Phi_A - \Phi_B)^2/(Q^2 - 4\pi^2/d^2)^2]^{1/2} \qquad \text{(A 31)}$$

Now, for m = 1, $Q = 2\pi/d$ and so the $\sin(Qd/2)(\Phi_A + \Phi_B)^2/Q^2$ term in equation (A 31) is zero, but the second term remains since

$$\lim_{Q\to 2\pi/d} \{[\sin(Qd/2)]/(Q^2 - 4\pi^2/d^2)\} = -\, d^2/8\pi \qquad \text{(A 32)}$$

which gives

$$|F(\theta_1)| = (d/4)(\Phi_B - \Phi_A) \qquad \text{(A 33)}$$

For $m > 1$, $|F(\theta_m)|$ is zero

(II) Dynamical Theory with Absorption

All materials absorb in the soft x-ray and so $f_2 \neq 0$, so that $F(\theta)$ is complex This situation may be treated using an approach analogous to that invoked by Parratt for the interference of x-rays caused by contaminant layers on the surface of a glancing incidence mirror

Continuity of the tangential components of the electric fields must be boundary condition at layer interfaces If E_{ij} is the electric field vector amplitude

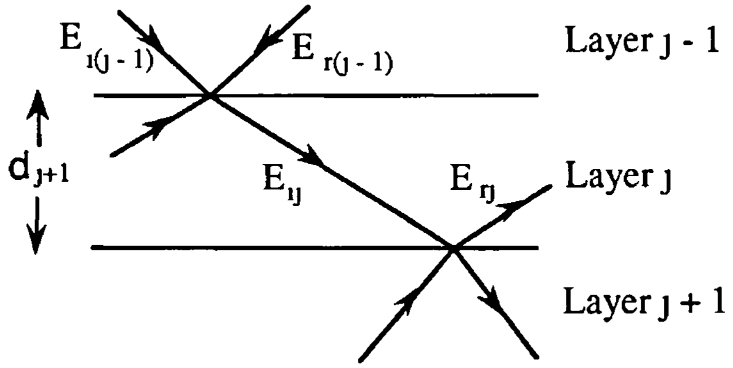

Figure A 1 Electric field continuity at interfaces between layers incident between the jth and (j + 1)th layers and E_{rj} is the reflected vector amplitude from the interface, then the Fresnel coefficients $F_{j,j+1}(\sigma)$, $F_{j,j+1}(\pi)$ for the reflection of the σ and π components of polarisation from the interface may be written

$$F_{j,j+1}(\sigma) = (E_{rj}/E_{ij})^{\sigma} = g_j - g_{j+1}/g_j + g_{j+1} \tag{A.34}$$

and

$$F_{j,j+1}(\pi) = (E_{rj}/E_{ij})^{\pi} = (g_j/\eta_j^2 - g_{j+1}/\eta_{j+1}^2)/(g_j/\eta_j^2 + g_{j+1}/\eta_{j+1}^2) \tag{A.35}$$

where

$$g_j = (\eta_j^2 - \cos^2\theta)^{1/2}. \tag{A.36}$$

Here θ is the glancing angle to the jth layer.

Define the reflectivity from the interface as

$$R_{j,j+1} = a_j(E_{rj}/E_{ij}) \tag{A.37}$$

where

$$a_j = \exp(-i\pi g_j d_j/\lambda) \tag{A.38}$$

is the amplitude factor midway through the jth layer. A recursive formula may now be written as

$$R_{j,j+1} = a_j^4(R_{j+1,j+2} + F_{j,j+1}/R_{j+1,j+2}\,F_{j,j+1} + 1) \tag{A.39}$$

Computation of the multilayer reflectivity starts at the substrate interface where the reflectivity is known to zero, i.e., $R_{2L+2,2L+1} = 0$. Successive application of equation (A.39) eventually leads to the interface between the vacuum and multilayer where $a_1 = 1$ and

$$I(\theta)/I_0 = R_{1,2}^2. \tag{A.40}$$

(III) Calculation of Optical Constants

The high refractive index metal layer is an alloy of 80% nickel and 20% chromium by weight. The specific density of NiCr = 8.496 gcm^{-3}, so that 8.496 g of NiCr contains $8.496 \times 0.8 = 6.832$ g of nickel and $8.496 \times 0.2 = 1.699$ g of chromium. Avogadro's number, N_A, of atoms (6.023×10^{23}) weighs 58.71 g for Ni, and 52.01 g for Cr. Thus, in 1 cm^{-3} of NiCr, there are

$$N_A \times (6.832/58.71 + 1.699/52.01)$$

atoms. Therefore, one finds that the optical constants are given by equations (A.3) and (A.4):

$$\delta_{NiCr} = (r_e\lambda^2/2\pi)\, N_A\, [(6.832/58.71) f_1^{Ni} + (1.699/52.01) f_1^{Cr}]$$

$$\beta_{NiCr} = (r_e\lambda^2/2\pi)\, N_A\, [(6.832/58.71) f_2^{Ni} + (1.699/52.01) f_2^{Cr}]$$

Listed in Table A.I are the scattering factors f_1 and f_2 for Ni, Cr and C. These values have been extracted from Henke's tables [103]. The corresponding calculated values for δ and ß are also shown

Table A I The f_1 and f_2 scattering factors, and scattering and refractive decrements for the elements used in the high refractive index layer of the NiCr/C multilayer for incident energies in the XUV

E (eV)	λ (Å)	f_1^{Ni}	f_1^{Cr}	f_2^{Ni}	f_2^{Cr}	δ_{NiCr}	β_{NiCr}
108 5	114	9 74	9 74	10 93	5 39	0 0522	0 0459
114	108 7	10 19	9 83	11 17	5 37	0 0494	0 0420
132 8	93 4	11 84	10 02	11 90	5 21	0 0415	0 0314
148 7	83 4	12 97	9 79	12 40	5 10	0 0359	0 0245

These data for δ and ß were then fitted to 2nd order polynomial equations and the following expressions in λ obtained

$$\delta_{NiCr}\,(\lambda)= 0\ 018517 + 7\ 423\times10^{-4}\lambda - 1\ 074\times10^{-6}\lambda^2$$

$$\beta_{NiCr}\,(\lambda)= -0\ 027666 + 5\ 65\times10^{-4}\lambda - 6\ 7\times10^{-7}\lambda^2$$

with λ in Angstrom (Å) units

The same procedure was carried through for the low refractive index carbon layer using a specific density of 2 g cm^{-3}, and knowing that Avogadro's number of carbon atoms weighs 12 g Results are presented in Table A II

Table A II The atomic scattering factors, f_1 and f_2, and corresponding scattering and refractive increments of carbon

E (eV)	λ (Å)	f_1^C	f_2^C	δ_C	β_C (× 10^{-3})
108 5	114	4 05	0 596	0 0244	1 423
114	108 7	4 05	0 568	0 0222	2 350
132 8	93 4	4 05	0 497	0 0164	3 157
148 7	83 4	4 05	0 433	0 0131	1 925

Again, these data for δ and ß were fitted and the following expressions obtained·

$$\delta_c\,(\lambda) = 1\ 88\times10^{-6}\lambda^2$$

$$\beta_c\,(\lambda) = 0\ 4241 - 1\ 355\times10^{-2}\lambda + 1\ 435\times10^{-4}\lambda^2 - 5\times10^{-7}\lambda^3$$

with λ in Å

The scattering factors for nickel, chromium and carbon vary in an almost linear fashion such that the f values needed for energies in the system bandpass may be interpolated from the best fit straight line graph as plotted in figure A 2 These scattering factor are listed in Table A III

Table A III The f_1 and f_2 scattering factors for the elements used in the high refractive index layer of the NiCr/C multilayer for incident energies in the system bandpass

E (eV)	f_1^{Ni}	f_1^{Cr}	f_1^{C}	f_2^{Ni}	f_2^{Cr}	f_2^{C}	f_2^{NiCr}	f_2^{C}
121	10 81	9 88	1 47	5 27	4 05	0 548	10 98	8 68
123	10 98	9 91	11 55	5 25	4 05	0 540	11 13	8 70
125 4	11 18	9 93	11 65	5 24	4 05	0 524	11 30	8 71
127	11 33	9 95	11 74	5 22	4 05	0 528	11 43	8 72
129	11 49	9 97	11 81	5 21	4 05	0 517	11 57	8 73

The average f for the alloy was obtained by a number of atoms weighting factor The number of atoms are in the ratio of (6 832/58 71) / (1 699/52 01) ≈ 3 87 Thus the atomic proportion is 1/3 87 = 0 26 for Cr and 0 74 for Ni, that is to say

$$f_{1,2}^{NiCr} = 0\ 74 f_{1,2}^{Ni} + 0\ 26 f_{1,2}^{Cr}$$

(IV) Calculation of Corrected Bragg Angles

Using the fitting curves for δ and β derived for the NiCr and C layers allowed the optical constants to be generated for different incident energies within the energy bandpass of the XUV flux measurement system, i e , from 121 to 129 4 eV Results are compiled in Table A IV The average scattering decrement, δ_0, is given by 0 5(δ_{NiCr} + δ_C) Knowing this, one may proceed to calculate the Bragg angle, θ_m, as from equation A 1, and subsequently the corrected Bragg angle as defined by expression A 16

Table A IV The scattering decrements for the NiCr and C layers and corresponding Bragg and corrected Bragg angles for energies in the bandpass of the XUV measurement system

E (eV)	δ_{NiCr}	δ_C	δ_0	θ_m (deg)	θ_m^P (deg)
121	0 0463	0 0197	0 0330	43 30	47 09
123	0 0454	0 0191	0 0322	42 43	46 13
125 4	0 0476	0 0182	0 0314	41 436	45 06
127	0 0437	0 0179	0 0308	40 80	44 37
129	0 0429	0 0174	0 0301	40 04	43 54

(V) Calculation of the Integrated Reflectivities

Before calculating R_m^I for the NiCr/C multilayer, the scattering amplitude densities for each layer type must be determined This may be achieved using equation A 6 in the form

$$\Phi = N(f_1^2 + f_2^2)^{1/2} r_e \qquad (\mathrm{cm}^{-2})$$

where $r_e = 2\ 818 \times 10^{-13}$ cm This may be broken down into equations for each layer type

$$\Phi^{NiCr} = N^{NiCr}[(f_1^{NiCr})^2 + (f_2^{NiCr})^2]^{1/2} r_e$$

$$\Phi^{C} = N^{C}[(f_1^{C})^2 + (f_2^{C})^2]^{1/2} r_e$$

The number density for each material may be calculated as

$$N^{NiCr} = N_A(6\ 832/58\ 71 + 1\ 699/52\ 01) = 8\ 98 \times 10^{22}\ \mathrm{cm}^{-3}$$

$$N^{C} = N_A(2/12) \approx 1 \times 10^{23}\ \mathrm{cm}^{-3}$$

The parameter, Â, given by expression A 9 for unpolarised radiation, and with $d_A = d_B = 33\ 9$ Å, reads as

$$\hat{A} = (Ld^2/\pi)(1 + |\cos 2\theta_m|)(\Phi_{NiCr} - \Phi_C)$$

assuming that the layers form perfectly sharp interfaces Table A V lists the amplitude scattering densities, Â parameters and integrated reflectivities at different energies in the bandpass

Thus, from Table A V, it can be seen that the efficiency of the NiCr/C multilayer is not constant across the energy bandpass of the XUV measurement system This may be understood if one examines the π- and σ-polarisation components of the incident radiation At 45° or Brewster's angle, the π-polarisation vanishes to leave only σ-polarised radiation reflected This is evident from the above data in Table A V where the lowest efficiency is calculated to be at 45° At non-

Table A IV The amplitude scattering factors for the NiCr and C layers, and the Â parameters and corresponding integrated reflectivities (or efficiency) of the NiCr/C multilayer for energies in the bandpass of the XUV measurement system at an angle of incidence of 45°

E (eV)	Φ^{NiCr} (× 10^{11})	Φ^{C} (× 10^{11})	Â	R_m^I
121	3 542	1 15	1 13	0 04
123	3 57	1 15	1 116	0 0375
125 4	3 61	1 15	1 094	0 035
127	3 64	1 15	1 13	0 036
129	3 67	1 15	1 17	0 037

oblique angles, the overall reflected radiation increases due to the increase in contribution from the π-polarisation

Appendix B

Photographs of XUV Flux Measurement System

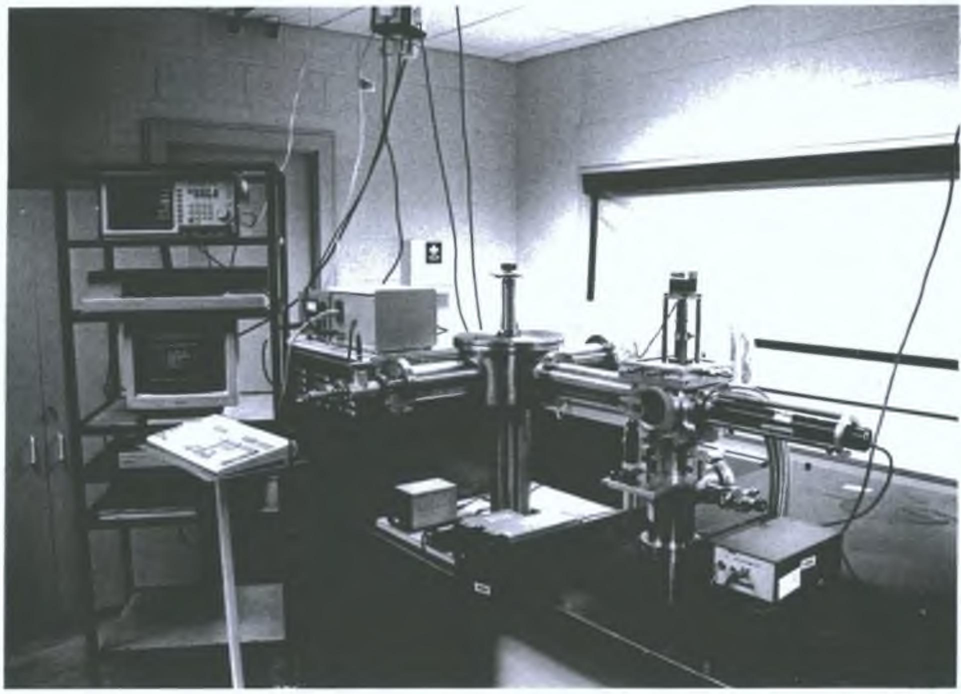

Photograph B.1 The assembled XUV flux measurement system.

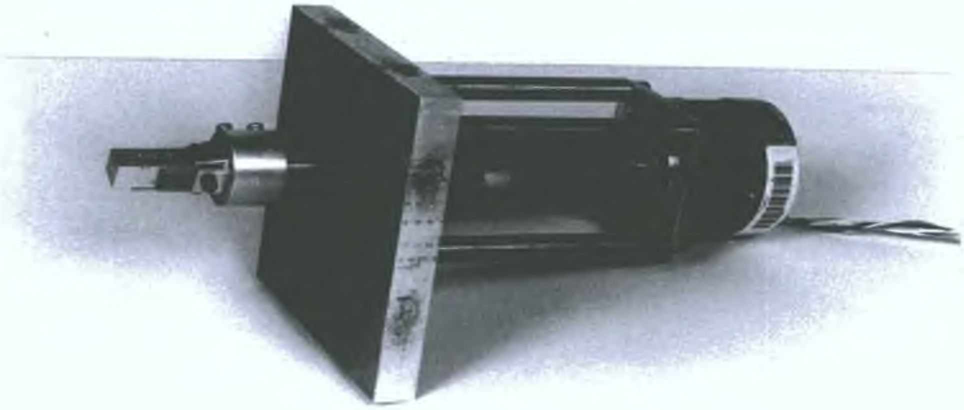

Photograph B.2 The planar target mount attached to the shaft of the stepper motor.

Photograph B.3 The multilayer and mount attached to a rotatable shaft with angular calibration.

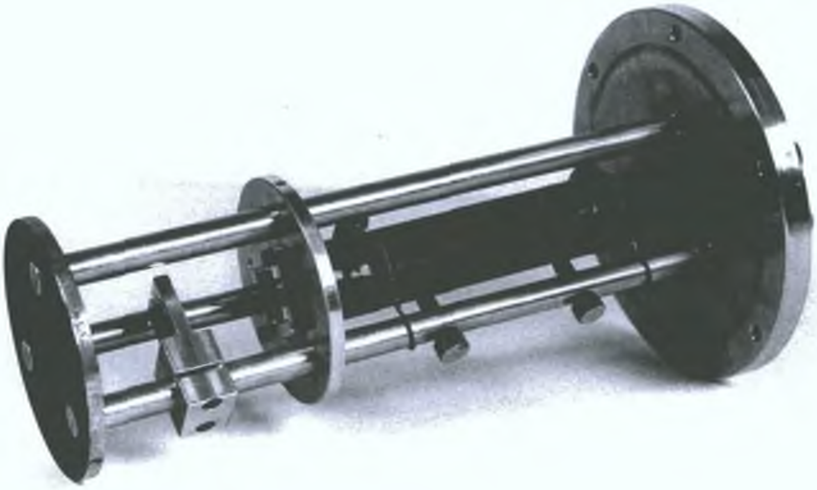

Photograph B.4 XUV detector consisting of from left-to-right: stop with collimating aperture and vent holes, carbon thin-film mount, silver-coated NE102A scintillator and mount, interference filter attached to housed photomultiplier tube on spring loaded mounting system.

Appendix C

The Nd:YAG Laser

A substantial amount of the work on LPPs has been carried out using solid state lasers, especially Q-switched Nd YAG lasers systems A YAG ($Y_2Al_5O_{12}$-yttrium aluminium garnet) crystal doped with Nd^{3+} ions is optically pumped by radiation emitted from powerful discharge flashlamps In this 4-level pumping scheme (figure C 1), the energy is absorbed in allowed transitions over a fairly broad spectral range and then transferred by fast and efficient non-radiative processes into the discrete upper level of the laser transition When a population inversion occurs between the upper and lower laser transition levels, stimulated emission becomes the important process

By inhibiting the normal lasing action of the system, via an optical shutter, for a certain time after the pumping pulse has started, an optimal population inversion may be achieved On opening the shutter, this stored energy may be suddenly released, resulting in the laser radiation being emitted in a giant pulse of energy, the process is known as Q-switching Optical shuttering may be achieved using a Pockels cell (electro-optical device) which controls the transmission of light through the laser cavity

An optical amplifier may be used to further increase the laser output Such a device is simply a crystal of the same material used in the lasing medium (also known as the oscillator) synchronously pumped with the laser A high degree of population inversion is obtained in the amplifier so that when the driving laser radiation from the oscillator passes through the amplifier medium, stimulated emission occurs and the energy stored in the crystal is transferred to the giant pulse

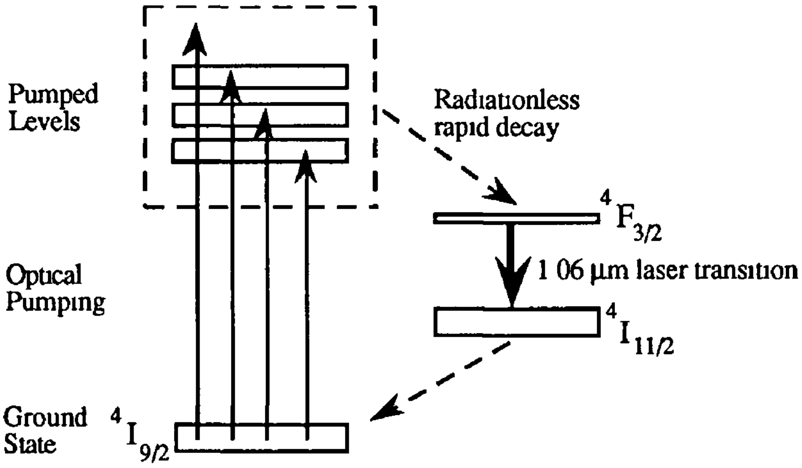

Figure C 1 Simplified energy level diagram for the Nd^{3+} ions in a YAG crystal